

# 博士論文

Thermodynamic and Kinetic Properties of  
Alkali Metal Amide-Hydrogen System

〔アルカリ金属アミド-水素系における  
熱力学及び動力学特性〕

五 舛 目 清 剛

広島大学大学院先端物質科学研究科

2015年3月

# 目次

## 1. 主論文

Thermodynamic and Kinetic Properties of Alkali Metal Amide-Hydrogen System

(アルカリ金属アミド-水素系における熱力学及び動力学特性)

五舛目 清剛

## 2. 公表論文

(1) Ammonia Synthesis via Non-Equilibrium Reaction of Lithium Nitride in Hydrogen Flow Condition

Kiyotaka Goshome, Hiroki Miyaoka, Hikaru Yamamoto, Tomoyuki Ichikawa, Takayuki Ichikawa, and Yoshitsugu Kojima

Materials Transaction, **56** (3), 410-414 (2015).

## 3. 参考論文

(1) Lithium Hydrazinidoborane: A Polymorphic Material with Potential for Chemical Hydrogen Storage

Romain Moury, Umit B. Demirci, Voraksmy Ban, Yaroslav Filinchuk, Takayuki Ichikawa, Liang Zeng, Kiyotaka Goshome, and Philippe Miele

Chemistry of Materials, **26** (10), 3249-3255 (2014).

# 主論文

## Abstract

Metal amide and hydrogen ( $MNH_2-H_2$ ) system is recognized as a promising reversible hydrogen storage system due to its high hydrogen capacity and lower operating temperature. However, slow reaction rate for the Li system with the highest hydrogen capacity is an important issue to be solved for practical use. In this thesis, modification of the reaction properties for the  $LiNH_2-H_2$  system is carried out from thermodynamic and kinetic points of view. Particularly, the novel ammonia synthesis technique is proposed by applying the  $LiNH_2-H_2$  system and Amide-imide system.

Lithium hydride-Potassium hydride ( $LiH-KH$ ) complex synthesized by ball-milling has been focused in order to modify the kinetic properties of the reaction between  $LiH$  and ammonia. The  $LiH-NH_3$  system is recognized as one of the most promising hydrogen storage system because it generates hydrogen at room temperature by ammonolysis reaction. Moreover, the starting system can be regenerated below  $300\text{ }^\circ\text{C}$  and possesses more than 8.0 wt.% hydrogen capacity. From the experimental results, it is confirmed that the hydrogen generation from the reaction between ammonia and the  $LiH-KH$  complex shows much higher reaction rate than that of the simple summation of each component as a synergetic effect. Then, a double-cation amide  $MNH_2$  ( $LiK(NH_2)_2$ ) phase, which could not be assigned to any reported amides so far, is formed as the reaction product. Moreover, in the hydrogenation of  $LiK(NH_2)_2$ , two processes were confirmed at the different temperatures. After the low temperature hydrogenation,  $KH$ -lithium amide ( $LiNH_2$ ) composite is generated as the hydrogenated product. It is noteworthy that the hydrogenation temperature of the composite is dramatically lower than that of  $LiNH_2$  itself, which should be due to the interaction between  $LiNH_2$  and  $KH$  such as a eutectic melting phenomenon.

An ammonia synthesis technique from lithium nitride ( $\text{Li}_3\text{N}$ ) based on the reactions of “Amide-imide system” and “Amide-hydrogen system” is proposed. Namely,  $\text{Li}_3\text{N}$  is hydrogenated below  $300\text{ }^\circ\text{C}$  under  $0.5\text{ MPa}$  hydrogen atmosphere, and then  $\text{LiNH}_2$  and  $\text{LiH}$  are formed as products. Furthermore, the reaction between  $\text{LiNH}_2$  and hydrogen proceeds below  $250\text{ }^\circ\text{C}$  under  $0.5\text{ MPa}$  of hydrogen flow condition, which results in the formation of ammonia and  $\text{LiH}$ . In this study, a new method of ammonia synthesis is proposed at laboratory scale using above two reactions. This method is capable of being operated under more moderate conditions than those of Haber–Bosch process. The proposed method is investigated for various reaction system such as open system, closed gas circuit system, and closed gas exchange system using couple of hydrogen storage alloys. As a result, it is experimentally clarified that the ammonia can be synthesized below  $300\text{ }^\circ\text{C}$  and  $0.5\text{ MPa}$  with realistic reactions rate by non-equilibrium reaction field under certain hydrogen flow rate even in the closed system.

## Contents

1 Introduction .....	1
1-1 Hydrogen storage for energy system.....	1
1-1-1 Hydrogen energy.....	1
1-1-2 Hydrogen storage .....	2
1-2 Hydrogen storage material .....	5
1-2-1 Metal hydride .....	5
1-2-2 Material composed of light elements .....	6
1-2-3 Thermodynamics.....	8
1-2-4 Kinetics .....	16
1-3 Ammonia .....	19
1-3-1 Ammonia.....	19
1-3-2 Synthesis .....	22
1-3-3 Decomposition .....	23
1-4 Metal amide- hydrogen system .....	26
1-4-1 Hydrogen generation reaction (Ammonolysis of MH).....	27
1-4-2 Regeneration reaction of MH and NH <sub>3</sub> (Hydrogenation of MNH <sub>2</sub> ) .....	28
References .....	30
2 Purpose .....	33
3 Experimental procedures .....	35
3-1 Sample preparation.....	35
3-1-1 Materials .....	35
3-1-2 Mechanical ball- milling method .....	35
3-1-3 Synthesis of samples .....	37
3-2 Experimental technique.....	39

3-2-1 Powder X-ray diffraction (XRD) measurement.....	39
3-2-2 Fourier transform infrared (FT-IR) spectroscopy .....	42
3-2-3 Differential scanning calorimetry (DSC).....	47
3-2-4 Thermal desorption mass spectroscopy (TDMS) .....	50
3-2-5 Ammonolysis reaction of MH.....	53
References .....	55
4 Results and discussion.....	56
4-1 Hydrogen generation reaction of metal hydride complex with ammonia.....	56
4-1-1 Synthesis of LiH-KH complex .....	56
4-1-2 Hydrogen generation reaction of LiH-KH complex with ammonia.....	59
4-1-3 Summary .....	65
4-2 Hydrogenation reaction of LiK(NH <sub>2</sub> ) <sub>2</sub> .....	66
4-2-1 Thermal properties of LiK(NH <sub>2</sub> ) <sub>2</sub> .....	66
4-2-2 Hydrogenation reaction of LiK(NH <sub>2</sub> ) <sub>2</sub> .....	69
4-2-3 Thermal property of LiNH <sub>2</sub> -KH complex.....	75
4-2-4 Hydrogenation reaction of LiNH <sub>2</sub> and LiK(NH <sub>2</sub> ) <sub>2</sub> in closed system .....	79
4-2-5 Summary .....	82
4-3 Ammonia synthesis from Lithium nitride .....	87
4-3-1 Hydrogenation reaction of Li <sub>3</sub> N .....	87
4-3-2 ND <sub>3</sub> synthesis.....	90
4-3-3 Summary .....	91
References .....	93
5 Conclusion.....	94

## **1 Introduction**

### **1-1 Hydrogen storage for energy system**

Since the “Industrial Revolution” began in the 18<sup>th</sup> century, the global consumption of primary energy has been increased rapidly until now. There are various forms of primary energy, e.g. a fossil energy, a nuclear energy, and natural energies such as wind power, solar light, geothermal power, and so on, where the fossil energy accounts for as high as 90 % of the primary energy consumption[1-1]. Thus, the global society based on large-scale fossil energy production and consumption is facing serious problems such as air pollution, global warming, and exhaustion of fossil fuels. Therefore, development of a clean and sustainable system is required. According to this requirement, utilization of nuclear energy as a sustainable energy was promoted, and then more than four hundred plants for nuclear power generation have been operated throughout the world[1-2]. In Japan as well, the nuclear power generation had accounted more than 10 % of the domestic energy consumption until a few years ago[1-1]. Under such circumstances, serious nuclear accidents such as the nuclear meltdown at Chernobyl and so on occurred across the globe. Furthermore, the nuclear power plant disaster due to “The Great Eastern-Japan Earthquake” in 2011 occurred and inflicted substantial damage on the environment by the leak of radioactive materials. Thus, the question about the safety of nuclear power has been raised and discussed significantly in recent years.

#### ***1-1-1 Hydrogen energy***

In the circumstances described above, utilization of renewable energy converted to electrical energy is proposed as a sustainable energy system. However, renewable energy by solar power and wind power and others depend strongly on the weather, which is a big

problem for a stable power supply. Besides, it is difficult to store and transport a great deal of electrical energy in the long term. To resolve the problems, hydrogen which can be produced from the renewable energy and stored in the long term has attracted attention as a clean secondary energy. Hydrogen can be produced from biomass, water, and others, and then expected to be used as an energy source for a fuel-cell vehicle (FCV) and other applications. When hydrogen is reacted with oxygen to obtain heat energy or electrical energy, no pollution gas such as  $\text{CO}_2$  and  $\text{NO}_x$  is produced but only  $\text{H}_2\text{O}$  is essentially generated; this make it to be considered as an ultimate clean energy. Additionally, hydrogen has the highest gravimetric energy density among all combustion fuels such as hydrocarbon fuel.

If utilization of hydrogen energy such as a FCV proceeds widely, it would bring a considerable effect on inhibiting the air pollution and the global warming. However, there are still various technical problems for utilization of hydrogen energy, namely, it is essential to develop a total system including “production”, “storage and transportation”, and “utilization” for hydrogen energy.

### ***1-1-2 Hydrogen storage***

To realize the sustainable society by hydrogen energy, it is essential to develop a high density storage and transportation method for hydrogen. Although hydrogen has a high gravimetric energy density, the volumetric energy density is much smaller than that of gasoline even though hydrogen is compressed to high pressure as shown in Fig. 1-1-1. Thus, it is considered to be difficult to store hydrogen compactly. Recently, “Compressed gaseous hydrogen system”, “Liquid hydrogen system”, and “Hydrogen storage materials” have been studied to develop a safety and mass hydrogen storage and transportation

system.

Regarding the compressed gaseous hydrogen system, gaseous hydrogen is introduced into a tank and mechanically compressed to 35-80MPa. It is considered that this hydrogen storage system can be applied technically easily, and has already put into practical use as an on-board hydrogen tank. For the practical use of this system, it is essential to develop a suitable tank which is required to have a compact and light weight body, high resistance to hydrogen embrittlement, and high strength for hydrogen pressure. Recently, the tank, which consists of an polyamide (nylon) 6 covered with a carbon-fiber composite and is able to withstand 70 MPa pressure, has been utilized on board[1-3].

Regarding the liquid hydrogen system, the volumetric hydrogen density is as high as  $70.8 \text{ kgH}_2 / \text{m}^3$  at  $-253 \text{ }^\circ\text{C}$ , which is more than 800 times larger than that of gaseous state ( $0.081 \text{ kgH}_2/\text{m}^3$  at  $25 \text{ }^\circ\text{C}$  under  $0.1 \text{ MPa}$ ) and more than 1.5 times larger than that of compressed gaseous hydrogen ( $42.6 \text{ kgH}_2/\text{m}^3$  at  $25 \text{ }^\circ\text{C}$  under  $80 \text{ MPa}$ )[1-4]. Besides, the gravimetric hydrogen density including the weight of the tank is more than 5 % at  $-253 \text{ }^\circ\text{C}$ . However, a large amount of energy corresponding to 30 % of its total energy contents is required for the liquefaction of the gaseous hydrogen because its boiling point is about 20 K under atmospheric pressure. Furthermore, it is inevitable that some energy loss continuously progresses due to its boil-off, where 0.7 % amount of hydrogen is lost per day even though a special adiathermanous columnar container (Inner volume:  $15 \text{ m}^3$ ) is adopted[1-5].

Thus, it is considered that solid-state hydrogen storage is one of the most promising ways to store hydrogen efficiently due to higher gravimetric and volumetric hydrogen density than that of liquid hydrogen system and compressed gaseous hydrogen system. There are various substances from gaseous phase to solid phase, which have a potential

to be a valuable hydrogen storage system, therefore, a lot of studies have been accomplished so far. However, there are still many problems to be solved for developing an effective hydrogen storage system, e.g. low gravimetric hydrogen density for hydrogen storage alloys, slow kinetics and high hydrogen ad/desorption temperature for light element hydrogen storage system.

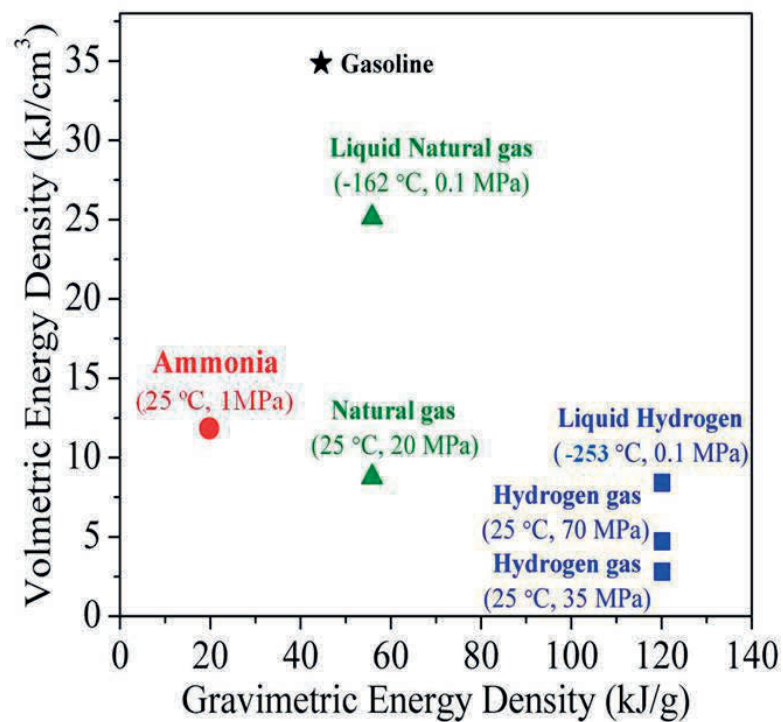


Figure 1-1-1 Gravimetric energy density and volumetric energy density of ammonia, gasoline, natural gas, and hydrogen.

## 1-2 Hydrogen storage material

### 1-2-1 Metal hydride

It is considered that more than a hundred of alloys have been developed so far. Basically, hydrogen storage alloys are made from element (A) which have a high hydrogen affinity and other element (B) which have a low hydrogen affinity. The compositions of the alloys are categorized to following four groups: AB type, AB<sub>2</sub> type, AB<sub>5</sub> type, and A<sub>2</sub>B type, where TiFe, TiCr<sub>2</sub>, LaNi<sub>5</sub>, and Mg<sub>2</sub>Ni are well known as a typical alloy for each type, respectively[1-6-8]. The basic properties for the typical hydrogen storage alloys are listed in Table 1-2-1. It is noted that alloys with various different properties can be designed by combination of A and B metals to obtain a suitable alloy for use of any applications and reversible hydrogen absorption and desorption properties.

Although the above hydrogen storage alloys can absorb and desorb hydrogen reversibly under moderate condition, the gravimetric hydrogen density is too small to be applied for a mass hydrogen transportation method because the alloys are composed of relatively heavier elements.

Table 1-2-1 Basic properties as hydrogen storage system for typical hydrogen storage alloys

Alloy	Type	Capacity (mass%)	Desorption temperature (°C)	Desorption pressure (MPa)
TiFe	AB	1.8	RT	0.3
TiCr <sub>2</sub>	AB <sub>2</sub>	2.4	-91	0.1
LaNi <sub>5</sub>	AB <sub>5</sub>	1.4	RT	0.2~0.3
Mg <sub>2</sub> Ni	A <sub>2</sub> B	3.6	250	0.1

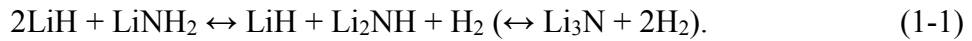
### ***1-2-2 Material composed of light elements***

Generally, hydrides of light elements (e.g. NaH, LiH, CaH<sub>2</sub>, MgH<sub>2</sub>, NaAlH<sub>4</sub>, LiBH<sub>4</sub>, NaBH<sub>4</sub>, NH<sub>3</sub>, NH<sub>3</sub>BH<sub>3</sub>, AlH<sub>3</sub>) have higher gravimetric densities (4-20 mass %) than that of hydrogen storage alloys (1-3 mass %) and a higher volumetric hydrogen density than that of compressed gaseous hydrogen system. However, hydrogen storage system with light element hydrides has some problems such as slow reaction rate and considerable reaction heat. Therefore, various studies to control the kinetics and thermodynamics have been reported so far.

Complex hydrides have been regarded as promising hydrogen storage material because they possess a comparatively high gravimetric hydrogen density. Complex hydrides expressed as  $M(XH_m)_n$  are composed of alkaline or alkaline-earth metal cation (e.g.  $M^{n+} = Li^+, Na^+, K^+, Mg^{2+}, Ca^{2+}$ ) and complex anion (e.g.  $XH_m = [NH_2]^-, [BH_4]^-, [AlH_4]^-$ ). Moreover, many composite systems consist of metal hydride ( $MH$ ) and complex hydrides  $M(XH_m)_n$  have been reported recently. Some examples of complex hydrides as hydrogen storage material and composite system, which are associated with this thesis, are introduced below.

### **Amide-imide hydrogen storage (M-N-H) system**

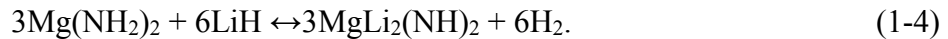
M-N-H system is a comparatively-new hydrogen storage system, which was reported by P. Chen *et al.* in 2002[1-9]. M-N-H system is known as a hydrogen storage system for its solid-solid reaction. Namely, the hydrogen storage state is composed of solid metal amide  $M_I(NH_2)_m$  and solid metal hydride  $M_{II}H$ , where hydrogen is generated by the interaction between these two solid phases, for example, described as following reaction ( $M_I, M_{II} = Li$ ),



It was reported that 1 mol %  $\text{TiCl}_3$  doped -  $\text{LiNH}_2/\text{LiH}$  composite prepared by ball-milling can reversibly desorb and absorb a large amount of hydrogen (~5.5 mass %) below 200 °C[1-10-12]. Moreover, it was proposed that the hydrogen desorption reaction would proceed by following two elementary processes, where ammonia would act as an important intermediate [1-13-15],



Furthermore, many reports for  $M\text{-N-H}$  system with various combinations of  $M_1(\text{NH}_2)_m$  and  $M_2\text{H}$  have been published, including the combination of  $\text{Mg}(\text{NH}_2)_2$  and  $\text{LiH}$ , which is known as  $\text{Li-Mg-N-H}$  system and has attracted attention as one of the most practical system. It can generate 5.5 mass % of hydrogen and is capable of being re-hydrogenated under 150 °C as follows[1-16-18],



It is noteworthy that the  $\text{Li-Mg-N-H}$  system has suitable thermodynamic properties for on-board hydrogen storage material. Therefore, various studies for understanding the reaction mechanism have been conducted so far.

### **Hydrolysis of $\text{NaBH}_4$**

Sodium borohydride ( $\text{NaBH}_4$ ) is one of the promising hydrogen storage materials not only as a reversible hydrogen storage material but also as a non-reversible hydrogen storage material, namely, the one-time hydrolysis reaction of  $\text{NaBH}_4$  proceed at room temperature to generate hydrogen by exothermic reaction as follows[1-19-23],



Actually, Kojima *et al.* reported that the hydrolysis reaction catalyzed by Pt-LiCoO<sub>2</sub> shows more than 90% reaction yield within 15 min even at room temperature[1-20]. However, high temperature over 1500 °C is required to regenerate NaBH<sub>4</sub> from NaBO<sub>2</sub> as reaction product. Furthermore, it was clarified that NaBH<sub>4</sub> can be regenerated by reacting with MgH<sub>2</sub> under 0.1~7.0 MPa hydrogen atmosphere at 350~750 °C as follows[1-24],



However, this process still required high temperature, and regeneration of MgH<sub>2</sub> from MgO under moderate condition is required to achieve the totally recyclable system.

### **1-2-3 Thermodynamics**

Hydrogen atom associates with metals in various forms. Alkali and alkali-earth metals form hydrides with covalent bond stoichiometrically, while, aluminium, silicon, and others form hydrides with ionic bond stoichiometrically. On the other hand, many of transition metals form hydride phase with keeping its metallic behavior over non-stoichiometric composition, which is called “metal-hydrogen alloys”. This section concerns the thermodynamics of metal-hydrogen (*M-H*) system.

Fig. 1-2-1 shows a phase diagram of Nb-H system as an example. Hydrogen dissolves in the crystal lattice of niobium metal without changing the crystalline structure of the metal to form  $\alpha$ -phase, and then spinodal decomposition occurs to form  $\alpha'$ -phase which has the same crystalline structure with  $\alpha$ -phase but different chemical composition from  $\alpha$ -phase under certain temperature. Besides,  $\beta$ ,  $\gamma$ ,  $\varepsilon$ ,  $\lambda$ , and  $\xi$ -phases having slightly-distorted crystalline structure with regularly-arrayed hydrogen, and  $\delta$ -phase having totally different crystalline structure, are formed under certain temperature with increasing

hydrogen concentration in the metal.

The thermodynamic aspects of metal-hydrogen system can be explained by pressure-composition isotherms (PCT-curves) as shown in Fig.1-2-2 (a). A metal dissolves some hydrogen to form a solid solution phase as  $\alpha$ -phase at low hydrogen pressure  $P_{H_2}$  and concentration  $C_H$  in the metal as shown in the figure. It is known that the solubility of hydrogen in a metal increases with increasing pressure of hydrogen gas according to “Sieverts law” at low hydrogen concentration as follows,

$$\sqrt{\frac{P_{H_2}}{P^0}} = K_S C_H. \quad (1-7)$$

Besides, the temperature dependence of Sieverts’ constant  $K_S$  is expressed approximately as follows,

$$\ln K_S = -\frac{\Delta S_S}{R} + \frac{\Delta H_S}{RT}, \quad (1-8)$$

where  $\Delta S_S$  is entropy of solution,  $\Delta H_S$  is enthalpy (heat) of solution which can be negative and positive value according to metal,  $T$  is temperature, and  $R$  is gas constant. The values of  $\Delta S_S$  and  $\Delta H_S$  of some metals are listed in Table 1-2-2.

When the hydrogen concentration in the metal increases with the pressure increase, nucleation and growth of the hydride  $\beta$ -phase start due to the influence of the certain interaction between H-H in the metal. During the formation of  $\beta$ -phase in coexistent state with  $\alpha$ -phase, the isotherm shows a plateau, where the length of the plateau determines the quantity of hydrogen which can be stored reversibly in the metal. After  $\alpha$ -phase changes to  $\beta$ -phase totally, hydrogen pressure starts to increase again with the increase of the gaseous hydrogen concentration. It is known that the plateau pressure  $P_{eq}(T)$  considerably depends on temperature, and the two-phase region ends at a critical point  $T_c$ ,

above which the transition from  $\alpha$ -phase to  $\beta$ -phase proceeds continuously without plateau region.

The thermodynamics of hydride formation is described as follows. Assuming that 1 mol of hydrogen reacts with a metal by following chemical equation,



the heat of formation of  $\beta$ -phase  $\Delta H_\beta$  is defined as follows,

$$\Delta H_\beta = \frac{2}{b}H_{MH_b} - \left( \frac{2}{b}H_M + H_{H_2} \right). \quad (1-10)$$

Similarly, considering the reaction of hydrogen with the metal to form  $\alpha$ -phase by following chemical equation,



the heat of formation of  $\alpha$  phase  $\Delta H_\alpha$  is defined as follows,

$$\Delta H_\alpha = \frac{2}{a}H_{MH_\alpha} - \left( \frac{2}{a}H_M + H_{H_2} \right). \quad (1-12)$$

Furthermore, considering the reaction of hydrogen with  $\alpha$ -phase to form  $\beta$ -phase by following chemical equation,



the heat of formation of  $\beta$ -phase  $\Delta H_{\alpha \rightarrow \beta}$  is defined by using  $\Delta H_\beta$  and  $\Delta H_\alpha$  as follows,

$$(b-a)\Delta H_{\alpha \rightarrow \beta} = b\Delta H_\beta - a\Delta H_\alpha. \quad (1-14)$$

When  $a$  is smaller enough compared with  $b$  ( $a \ll b$ ), equation (1-14) can be modified as follows,

$$\Delta H_{\alpha \rightarrow \beta} \approx \Delta H_\beta. \quad (1-15)$$

The reaction entropy change  $\Delta S_{\alpha \rightarrow \beta}$  is expressed as follows,

$$\Delta S_{\alpha \rightarrow \beta} = \frac{2}{b-a} (S_{\beta} - S_{\alpha}) - S_{H_2}^0 + R \ln \frac{P_{eq}}{P^0}, \quad (1-16)$$

where the entropy of gaseous hydrogen at  $P_{eq}$  is expressed by the standard entropy  $S_{H_2}^0$ , which is the entropy of hydrogen at 0.1MPa, and the entropy change term due to the hydrogen pressure difference between  $P_{eq}$  and  $P^0$ . At the equilibrium condition for the reaction (1-13), the Gibbs's free energy  $\Delta G_{\alpha \rightarrow \beta}$  can be expressed by the entropy change  $\Delta S_{\alpha \rightarrow \beta}$  and the enthalpy change  $\Delta H_{\alpha \rightarrow \beta}$  as follows,

$$\Delta G_{\alpha \rightarrow \beta} = \Delta H_{\alpha \rightarrow \beta} - T \Delta S_{\alpha \rightarrow \beta} = 0, \quad (1-17)$$

$$\Delta H_{\alpha \rightarrow \beta} = T \Delta S_{\alpha \rightarrow \beta}. \quad (1-18)$$

Thus, from equation (1-15), (1-16) and (1-18), the heat of formation of hydride  $\Delta H_{\beta}$  can be evaluated from the slope of a so-called van't Hoff plot of the plateau pressure on a logarithmic scale versus  $T^{-1}$  as shown in Fig. 1-2-2 (b). The reaction enthalpy change  $\Delta H$  by formation of metal hydride from metal or solid solution are shown in Table 1-2-3.

Generally, hydrogen desorption reaction of reversible hydrogen storage system such as metal-hydrogen system is endothermic reaction. Herein, the Gibbs's free energy  $\Delta G_d$  for hydrogen desorption reaction is expressed as follows,

$$\Delta G_d = \Delta H_d - T \Delta S^0 - TR \ln \left( \frac{P^0}{P_{H_2}} \right), \quad \Delta H_d > 0, \Delta S^0 > 0, \quad (1-19)$$

where  $\Delta H_d$  is enthalpy change,  $\Delta S^0$  is standard entropy change, and  $P_{H_2}$  is hydrogen pressure. Even though the hydrogen desorption reaction is endothermic reaction, it can proceed by controlling third entropy term, namely, increasing  $T$  and decreasing  $P_{H_2}$ .

Contrary to the above thermodynamics, if hydrogen absorption is endothermic reaction, the Gibbs's free energy  $\Delta G_a$  for hydrogen adsorption reaction is expressed as follows,

$$\Delta G_a = \Delta H_a - T\Delta S^0 - TR \ln\left(\frac{P_{H_2}}{P^0}\right), \quad \Delta H_a > 0, \Delta S^0 < 0. \quad (1-20)$$

In this case, the first term ( $\Delta H_a$ ) and the second term ( $-T\Delta S^0$ ) on the right side of equation (1-20) are positive value, therefore, it is impossible to make the reaction proceed under realistic temperature and pressure.

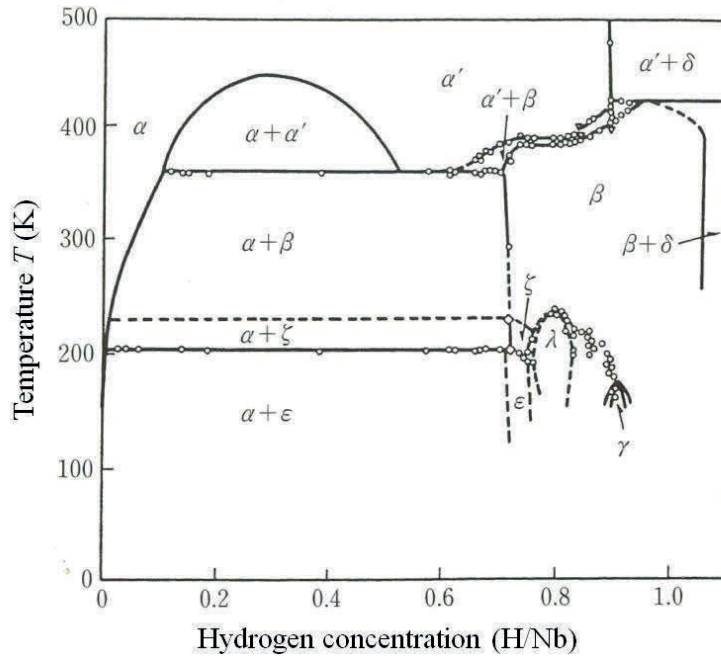


Figure 1-2-1 Phase diagram of Nb-H system[1-25]

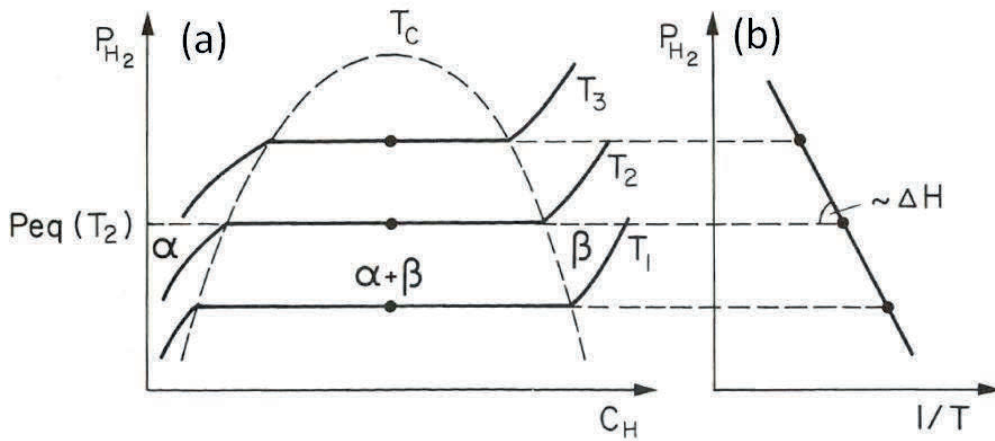


Figure 1-2-2 (a) Pressure-composition isotherms for the solid solution of hydrogen ( $\alpha$ -phase) and hydride formation ( $\beta$ -phase) and (b) its van't Hoff plot[1-26]

Table 1-2-2 The standard enthalpy and entropy changes to form a hydrogen solid solution at the low hydrogen concentration in the metal, and the temperature condition for the experiments.

Metal	$\Delta H_s$ kJ/mol H <sub>2</sub>	$\Delta S_s/R$ (mol H <sub>2</sub> ) <sup>-1</sup>	Temperature range °C
Li (liq.)	-52	-7	200-700
Na (liq.)	2	-	100-400
K (liq.)	~0	-	-
Mg	21	-4	100-670
Mg (liq.)	27	-	700-900
Al	67	-6	500
Al (liq.)	59	-	730-1730
Sc	-90	-7	-
Y	-82	-6	-
La (fcc)	-80	-8	-
Ce (fcc)	-74	-7	-
Ti (hcp)	-53	-7	500-800
Ti (bcc)	-60	-6	900-1100
Zr (hcp)	-63	-6	500-800
Zr (bcc)	-64	-6	860-950
Hf (hcp)	-36	-5	300-800
V	-27	-8	150-500
Nb	-34	-8	>0
Ta	-37	-8	>0
Cr	58	-5	730-1130
Mo	50	-5	900-1500
W	106	-5	900-1750
Fe (bcc)	29	-6	7-911
Fe (fcc)	28	-	911-1394
Fe (bcc)	29	-	1394-1538
Fe (liq.)	33	-	1538-1820
Ru	54	-5	1000-1500
Co (fcc)	32	-6	1000-1492
Rh	27	-6	800-1600
Ir	73	-5	1400-1600
Ni	16	-6	350-1600
Ni (liq.)	24	-	1490-1700
Pd	-10	-7	-78-75
Pt	46	-7	-
Cu	42	-6	<1080
Ag	68	-5	550-961
Au	36	-9	700-900
U ( $\alpha$ )	10	-6	<668
Mg <sub>2</sub> Ni	-13	-	-
TiFe	10	-	-
TaV <sub>2</sub>	-58	-	-

Table 1-2-3 The heat of formation and standard entropy of metal hydrides and the temperature conditions for the experiments.

<i>M</i> - <i>MH</i> system	$\Delta H$ kJ/mol H <sub>2</sub>	$\Delta S^0/R$ (mol H <sub>2</sub> ) <sup>-1</sup>	Temperature range °C
Li - LiH	-158	-16.2	600-900
Na - NaH	-114	-19.6	500-600
K - KH	-118	-20.2	288-415
Rb - RbH	-108	-20.4	246-350
Cs - CsH	-114	-20.4	245-378
Mg - MgH <sub>2</sub>	-74	-16	440-560
Ca - CaH <sub>2</sub>	-182	-16.8	600-800
Sr - SrH <sub>2</sub>	-198	-18.8	<1000
Ba - BaH <sub>2</sub>	-174	-17.2	470-550
Sc - ScH <sub>2</sub>	-200	-17.4	>600
Y - YH <sub>2</sub>	-226	-17.4	600-950
YH <sub>2</sub> - YH <sub>3</sub>	-178	-16.6	250-350
La - LaH <sub>2</sub>	-208	-18.2	600-800
LaH <sub>2</sub> - LaH <sub>3</sub>	-168	-	-
Ce - CeH <sub>2</sub>	-206	-17.8	600-800
CeH <sub>2</sub> - CeH <sub>3</sub>	-238	-	-
Pr - PrH <sub>2</sub>	-208	-17.6	600-800
Nd - NdH <sub>2</sub>	-212	-17.6	650-840
Sm - SmH <sub>2</sub>	-222	-19.6	-
Gd - GdH <sub>2</sub>	-196	-15.8	600-800
Er - ErH <sub>2</sub>	-226	-18.8	-
Ti (hcp) - TiH <sub>2</sub>	-130	12	<300
Zr (hcp) - ZrH <sub>2</sub>	-188	-18	400-550
Hf (hcp) - HfH <sub>2</sub>	-130	-12	600-900
V-VH <sub>0.5</sub>	-72	-13	0-100
V-VH <sub>2</sub>	-40	-18	50-120
Nb - NbH <sub>0.65</sub>	-92	-16	0-80
Nb - NbH <sub>2</sub>	-40	-16	25
Ta - TaH <sub>0.5</sub>	-78	-12	<50
Mn ( $\alpha$ ) - MnH	-22	14*	450-730
Ni - NiH	-58	14*	20
Pd - PdH <sub>0.5</sub>	-40	-10	-78-175
Mg <sub>2</sub> Ni - Mg <sub>2</sub> NiH <sub>4</sub>	-64	-18	-
TiFe - TiFeH	-28	-12.4	-
CaNi <sub>5</sub> - CaNi <sub>5</sub> H <sub>4</sub>	-34	-12.2	-
LaNi <sub>5</sub> - LaNi <sub>5</sub> H <sub>4</sub>	-32	-13	-

\* Assumed value

### ***1-2-4 Kinetics***

In this section, reaction kinetics for hydrogen absorption of *M-H* system is being discussed. The hydrogen absorption and desorption reactions in a metal proceed through several steps. It is important to understand the reaction mechanism, namely, to find out the rate-determining step to improve the kinetics of hydrogen storage materials.

It is considered that hydrogen dissolves in metal by following steps.

- (i) Adsorption step: Hydrogen molecule approaches the metal and is physisorbed on metal surface.
- (ii) Chemisorption step: The physisorbed hydrogen is dissociated to hydrogen atoms at the interface. Then, the hydrogen atoms are adsorbed at appropriate surface.
- (iii) Diffusion step: The adsorbed hydrogen atoms on the surface dissolve into the bulk through interstitial sites of the metal.
- (iv) Hydride forming step: If the local hydrogen concentration exceeds a certain limit, a hydride phase is formed, resulting in a crystalline change.

A simplified and frequently used model known as “one-dimensional model” to describe the dissociation of molecular hydrogen at an interface and the solution of hydrogen atoms in the bulk is shown in Fig. 1-2-3. The potential energy indicates, from left to right, a shallow local minimum for physisorbed hydrogen by van der Waals force (The heat of physisorption:  $\approx 5 \text{ kJ mol}^{-1} \text{ H}_2$ ), a deep local minimum for chemisorbed hydrogen atoms (The heat of chemisorption:  $\approx 50 \text{ kJ mol}^{-1} \text{ H}_2$ ), a rather deep minimum for hydrogen atom dissolved on interstitial site of the metal, and periodic minima separated from each other by diffusion barriers.

The mobility of atomic hydrogen in the bulk depends strongly on the diffusion barriers.

If each hydrogen atom can repeatedly jump to neighbor interstitial site in metal by receiving heat energy in microscopic scale, resulting the hydrogen diffusion phenomenon in macroscopic scale, the dependence of diffusion rate ( $D$ ) is expressed as follows,

$$D \approx d^2 \nu_D \exp\left(-\frac{E_{diff}}{kT}\right), \quad (1-21)$$

where,  $\nu_D$  is lattice frequency known as “Debye frequency”,  $d$  is a distance between neighboring interstitial sites,  $k$  is Boltzmann constant,  $T$  is temperature, and  $E_{diff}$  is the activation energy of diffusion in bulk. For example, the Arrhenius plots of bcc metals are shown in Fig.1-2-4. These Arrhenius plots show a straight line, indicating that the diffusion of hydrogen in metal can be described as thermally activated process according to equation (1-21).

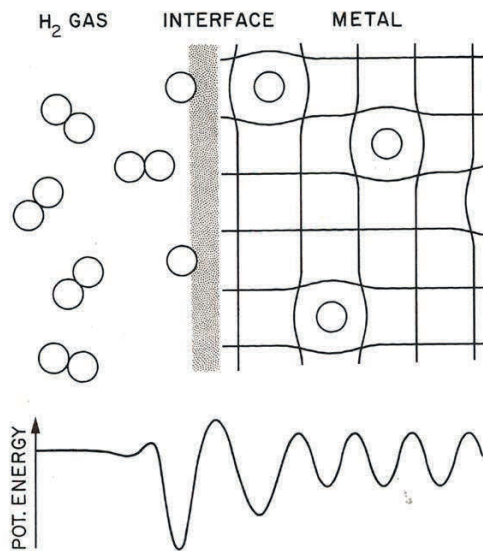


Figure 1-2-3 Simplified model of the dissociation of molecular hydrogen at an interface and solution of hydrogen atoms in the bulk with the potential energy curves[1-26]

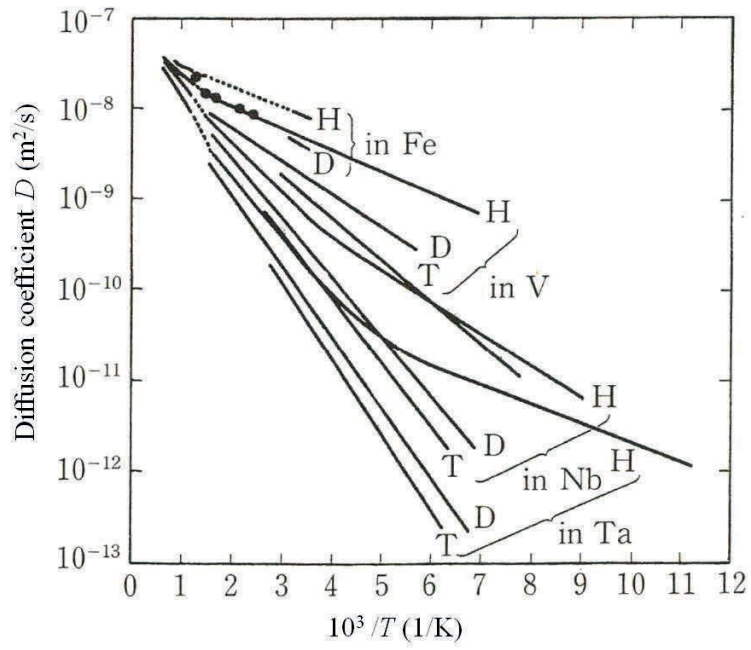


Figure 1-2-4 Arrhenius plots of diffusion rate for bcc metals[1-27]

### **1-3 Ammonia**

Among the various hydrogen storage systems or materials, liquid organic hydrides such as cyclo-hexane and decalin, which make a covalent bond with H atom in the hydriding state, can store hydrogen at the same level as liquid hydrogen. Meanwhile, liquid ammonia (NH<sub>3</sub>), which has a notably high gravimetric and volumetric hydrogen density compared with other light element hydrogen storage materials, has been recognized as a promising hydrogen carrier recently. Thus, the characteristic of ammonia as hydrogen storage material is focused on in this section.

#### ***1-3-1 Ammonia***

The molecular structure of ammonia is shown in Fig. 1-3-1. N atom has an unshared electron pair and three covalent electron pairs in an outer shell, namely, N atom forms covalent bonds with H by its sp<sup>3</sup> hybrid orbital. The angle between the N-H bonds of ammonia is 106.6 °, which is smaller than that of sp<sup>3</sup> hybrid orbital, 109.5 °, due to the repellent effect of the unshared electron pair. Since, H atoms in ammonia are positively charged, therefore, it is considered that ammonia can react easily with H atoms having negative charge, e.g. H atoms in alkaline metal hydride such as LiH, NaH, and KH.

The characteristic of ammonia, organic hydride, and hydrogen are listed in Table 1-3-1. The gravimetric hydrogen density of ammonia is 17.8 mass %, which is more than two times higher than those of organic hydrides. Besides, the volumetric hydrogen density of ammonia is 1.5 times higher than that of liquid hydrogen (7 kg/L) because it can be easily liquefied at 20 °C by compressing to 0.87 MPa[1-4]. Therefore, ammonia is recognized as a high capacity hydrogen storage material. Regarding the enthalpy change for hydrogen generation, the values of organic hydrides are 60-70kJ/molH<sub>2</sub>, which is more than two

times higher than that of hydrogen storage alloys. On the other hand, the enthalpy change of hydrogen generation from  $\text{NH}_3$  is  $30.6 \text{ kJ/molH}_2$  similarly to hydrogen storage alloys. Furthermore, it is noteworthy that hydrogen produced by using various energies can be converted into ammonia by the direct reaction of it to the nitrogen in the air. Therefore, ammonia is recognized as a renewable energy storage material.

The price of ammonia is  $600 \text{ \$/ton}$  (2014)[1-28]. Thus, the cost of hydrogen in ammonia is estimated to be  $35 \text{ \$/Nm}^3$ . The targeted cost of hydrogen supply is considered to be  $30 \text{ \$/Nm}^3$  for 2030[1-29]. Therefore, the cost of hydrogen in ammonia has already fulfilled the required value for 2030. Although ammonia has several advantages as hydrogen storage material as described above, it is designated as a specific mephitic substance and a deleterious substance under law. In this viewpoint, the safety of ammonia has been discussed in Risø National Laboratory (Denmark), where the harmful to body for ammonia is assessed as “3” which is higher than that of hydrogen (0), natural gas (1), and gasoline (1). On the other hand, the risk of flammability for ammonia is assessed as “1” which is lower than that of hydrogen (4), natural gas (4), and gasoline (3). Therefore, it's reported that the risk of ammonia shows comprehensively little difference from the other fuels which have already been used.

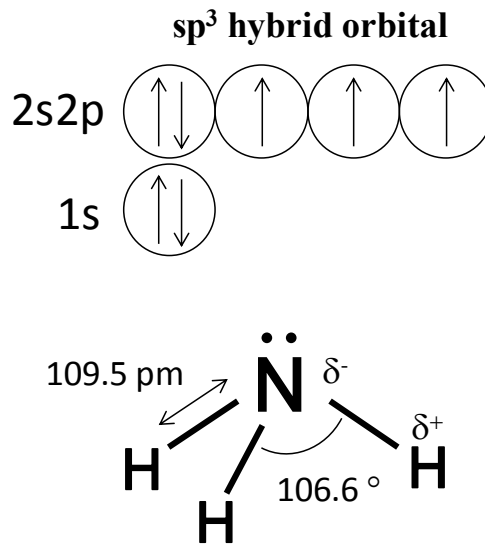


Figure 1-3-1 Molecular structure of ammonia

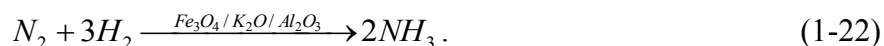
Table 1-3-1 Characteristics of liquid hydrogen, organic hydride, and liquid ammonia

Physical property	Ammonia	Decalin	Methylcyclohexane	Liquid hydrogen
	NH <sub>3</sub>	C <sub>10</sub> H <sub>12</sub>	C <sub>7</sub> H <sub>14</sub>	H <sub>2</sub>
Molecular weight (g/mol)	17.03	132.20	98.19	2.02
Density (g/cm <sup>3</sup> )	0.603*	0.97	0.769	0.0706
Gravimetric hydrogen density (mass%)	17.8	7.29	6.16	100
Volumetric hydrogen density (kg/100L)	10.7	7.07	4.73	7.06
Enthalpy change of hydrogen desorption (kJ/molH <sub>2</sub> )	30.6	59.6-61.8	67.5	0.899
Hydrogen desorption temperature (K)	623-1173	523-593	476-673	20.3

\* at 1.0 MPa, 298 K

### 1-3-2 Synthesis

Haber-Bosch process is a well-known ammonia synthesis technique for industrialized mass production under high temperature of 400-600 °C and high pressure of 20-40 MPa in the presence of iron oxide catalyst as follows [1-30],



The annual production of ammonia in the world by Haber-Bosch process reached as much as 1.3 hundred million tons in 2010[1-31]. The production of ammonia from hydrogen and nitrogen needs such a high temperature and pressure, even though the reaction is exothermic ( $\Delta H= 46$  kJ/mol  $NH_3$ ) due to the strong triple bond between N atoms in nitrogen molecule ( $945$  kJ mol<sup>-1</sup>)[1-32, 33]. Therefore, it is an important issue how to dissociate nitrogen efficiently for ammonia synthesis under mild condition. To find suitable catalyst, many studies for ammonia synthesis including  $Fe_3O_4$ -based iron catalysts,  $Fe_{1-x}O$ -based iron catalysts, ruthenium-based catalysts, and Co-Mo-N system catalyst, have been reported so far with a special emphasis on high-performing ruthenium-based catalysts during recent years.

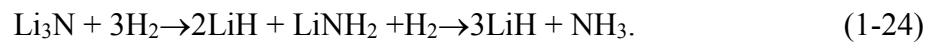
Ruthenium as an active component, potassium as a metal promoter, and carbon as a catalyst carrier, while combining together, showed high activity for ammonia synthesis[1-34]. As an advancement of this finding, often almost 20 years, a new ammonia synthesis process KAAP (Kellogg Advanced Ammonia Process) by using Ru/C catalyst was put into its industrial applications in 1992[1-35-37]. As a most recent report for ruthenium based catalyst, it was reported that ruthenium supported by electride ( $12CaO \cdot 7Al_2O_3$ ) which is one of the component material of cement functioned as a high-performance catalyst for ammonia synthesis at as low as 0.1 MPa and 400 °C[1-38, 39]. By using the

catalyst, the activation energy for the NH<sub>3</sub> synthesis became less than 50 kJ/mol, which is nearly a half of that reported previously for other Ru-based catalysts and Haber-Bosch catalyst.

As described above, it is an important issue how to dissociate nitrogen efficiently for ammonia synthesis under mild condition. In this view, the reaction of lithium (Li) with nitrogen attracts attention, described by the following chemical equation[1-40],



Only Li is the potential material to react with nitrogen below 100 °C, forming lithium nitride (Li<sub>3</sub>N). In other words, it is one of the simplest way to dissociate the nitrogen triple bond (N≡N), which possibly realizes the ammonia synthesis under milder condition by reaction between Li<sub>3</sub>N and hydrogen. Therefore, we proposed ammonia synthesis process applying reactions of the amide-imide hydrogen storage system (see section 1-2-2) and metal hydride-ammonia system (see section 1-4-2), described as follows,



Since each reaction proceeds below 300 °C and 0.5 MPa, it is expected that the ammonia synthesis process under moderate condition becomes possible by optimizing the reaction condition.

### ***1-3-3 Decomposition***

#### **Thermal decomposition (ammonia cracking)**

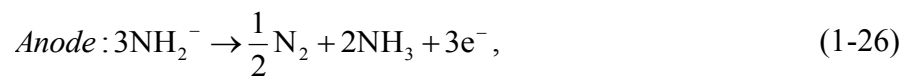
It is necessary to decompose ammonia to generate hydrogen. The decomposition of ammonia is expressed as follows,



In order to realize the reaction (1-25) with a reasonable fast reaction rate, alumina-supported nickel (Ni-Al<sub>2</sub>O<sub>3</sub>) which has an adequate mechanical strength and thermal stability had been studied as one of the first attempt followed by several authors[1-41, 42]. However, the temperature required for ammonia decomposition was still very high i.e. more than 1073 K. After several efforts, ruthenium is found to exhibit highest catalytic activity[1-43]. It, supported by carbon nano tube and potassium hydroxide (Ru-CNT-KOH), shows high reaction rate, resulting 50 % conversion rate at 0.1 MPa, 673 K, where the gas hourly space velocity (GHSV<sub>NH<sub>3</sub></sub>) is 60,000 ml/(h g<sub>cat</sub>)[1-44]. However this conversion yield (50 %) is still lower than that according to the equilibrium at 0.1 MPa and 673K (99 %). Therefore, further improvement of the catalyst to achieve full conversion yield is required.

## Electrolysis

Electrochemical process is one of the promising methods to decompose ammonia for generating hydrogen at moderate temperature. It was reported that ammonia dissolving in alkaline solution can be decomposed by electrolysis at room temperature, however, the gravimetric hydrogen density is as low as 6.1 mass % according to its solubility to water, 34.2 mass % at 20 °C. Thus, the direct electrolysis of liquid ammonia was investigated by Hanada *et al.*, where alkaline metal amide (MNH<sub>2</sub> ; M=Li, Na, K) was used as a supporting electrolyte[1-45, 46]. The redox reactions on the anode and the cathode are expressed as follows,



Namely,  $\text{NH}_2^-$  is electrically oxidized, generating nitrogen on the anode. Meanwhile, ammonia is electrically reduced, generating hydrogen and  $\text{NH}_2^-$  on the cathode. Thus, above redox reactions totally lead to decomposition of ammonia to generate hydrogen and nitrogen. Theoretically, the electrolysis voltage of liquid ammonia at 25 °C is estimated according to Nernst's equation,

$$E = -\frac{\Delta G^0}{3F} + \frac{RT \ln(p_{N_2}^{1/2} p_{H_2}^{3/2})}{3F}, \quad (1-28)$$

where  $\Delta G$  is standard Gibbs free energy,  $F$  is Faraday constant,  $T$  is temperature,  $R$  is gas constant,  $p_{N_2}$  is pressure of nitrogen, and  $p_{H_2}$  is pressure of hydrogen, respectively. The first term including the standard Gibbs free energy change and the second term including the hydrogen and nitrogen pressure are estimated to be 0.038 V, 0.039 V, respectively, indicating that the theoretical electrolysis voltage of liquid ammonia is 0.077 V. As a result, it was experimentally clarified that the current density for ammonia electrolysis becomes higher in the order of periodic table of alkali amide as an electrolyte ( $\text{Li} < \text{Na} < \text{K}$ ) due to the difference of the solubility of  $M\text{NH}_2$  in liquid ammonia. Namely, the solubility of  $M\text{NH}_2$  in liquid ammonia becomes higher in the order ( $\text{Li} < \text{Na} < \text{K}$ )[1-47], resulting higher concentration of  $\text{NH}_2^-$  in liquid ammonia. However, the experimental electrolysis voltage to obtain realistic reaction rate requires more than 1 V, which is still high for practical use. Furthermore, the ammonia electrolysis has a serious problem that the anode electrode is corroded during the electrolysis process. To decrease these over potential of ammonia electrolysis and to avoid the corrosion of the electrode, the effective electrode should be developed with the investigation of electrode reaction mechanism in the future.

#### 1-4 Metal amide- hydrogen system

As described above, more than 400 °C is required to generate hydrogen by thermal decomposition of ammonia even in the presence of Ru-based catalyst. Besides, although it was demonstrated that direct electrolysis of liquid ammonia at room temperature can proceed by using metal amide as a supporting electrolyte, the experimental electrolysis voltage is still high due to the over potential and it is difficult to avoid the corrosion of electrode up to now. Therefore, it is necessary to realize an efficient technique for ammonia to hydrogen conversion under moderate condition. In this viewpoint, ammonia and metal hydride ( $MH$ ;  $M = \text{Li, Na, K}$ ) system[1-48-52], widely known as  $MH\text{-NH}_3$  system or amide and hydrogen ( $M\text{NH}_2\text{-H}_2$ ) system, is focused as a reversible  $\text{NH}_3\text{-H}_2$  conversion technique. It can generate hydrogen even at room temperature by exothermic ammonolysis reaction, which is similar to the exothermic hydrolysis reaction of  $\text{NaBH}_4$  as described in section 1-2-2. Moreover, in contrast to difficult regeneration of  $\text{NaBH}_4$  from  $\text{NaBO}_2$  under moderate condition,  $MH$  and ammonia can be easily regenerated from  $M\text{NH}_2$  below 300 °C under hydrogen flow condition by following reaction[1-52],



The reaction enthalpy change and theoretical hydrogen density of  $M\text{NH}_2\text{-H}_2$  system are listed in Table 1-4-1. Although the reaction enthalpy change of Li system is somewhat large, those of Na system and K system are close to the target value for on-board hydrogen storage system (= 30~40 kJ/molH<sub>2</sub>). Herein, the target value of the reaction enthalpy is considered for hydrogen storage alloys as on-board hydrogen storage system. Since,  $M\text{NH}_2\text{-H}_2$  system is considered to be applied for a mass transportation system, therefore even the large reaction enthalpy change of Li system would be acceptable in the latter

case.

Table 1-4-1 Gravimetric hydrogen density and reaction enthalpy change of each  $MNH_2$ - $H_2$  system

	$ \Delta H^0 $ (kJ/molH <sub>2</sub> )	Gravimetric hydrogen density (wt%H <sub>2</sub> )
$LiH + NH_3 \leftrightarrow LiNH_2 + H_2$	43	8.1
$NaH + NH_3 \leftrightarrow NaNH_2 + H_2$	22	4.9
$KH + NH_3 \leftrightarrow KNH_2 + H_2$	25	3.5

#### ***1-4-1 Hydrogen generation reaction (Ammonolysis of MH)***

For  $MNH_2$ - $H_2$  system, hydrogen generation reaction (ammonolysis reaction) is exothermic reaction and expected to proceed at room temperature. The ammonolysis reaction of  $MH$  with gaseous phase ammonia at room temperature has been investigated before as a basic research. As a result, it was confirmed that the reaction rate become higher in the order of periodic table of alkali metal ( $Li < Na < K$ )[1-52]. Herein, considering that the ammonolysis reaction is a reaction between solid phase  $MH$  and gaseous phase ammonia, the oxide layer on the surface of  $MH$  should affect the reaction rate considerably. In fact, it was demonstrated that ball-milled  $MH$  showed much higher rate than that of as prepared  $MH$ , where it is claimed that the oxide layer is removed from the surface of  $MH$  by mechanical ball-milling.

Although K system has the highest reaction rate for hydrogen generation reaction, the gravimetric hydrogen density is much lower than that of Li system. On the other hand, the reaction of Li system, which has the highest hydrogen density, is considerably slow. Therefore, several studies concerning kinetic improvement of Li system were reported so far [1-50, 53]. Since the reaction of  $MH$  and ammonia is a gas-solid phase reaction, it is

possibly assumed that  $MNH_2$  formed on the surface blocks the contact of ammonia gas to  $MH$ , leading to the limited reaction rate. However, considering the rapid hydrogen generation reaction of K system with 100% reaction yield, it is inconsistent with the above assumption of the gas-solid phase reaction. Thus, it is proposed that ammonia could reach the interface of  $MH-MNH_2$  by forming ammoniate ( $MNH_2 \cdot xNH_3$ ) as a consistent reaction model [1-54]. According to this reaction model, the reaction rate is influenced by the interaction between  $MNH_2$  and ammonia. Therefore, it can be expected that the reaction rate must be improved by modification of the solid  $MNH_2$ .

When two kinds of metal hydrides are mixed or form a compound, the reaction shows different properties, e.g. melting point is lower than that of the individual components in the case of eutectic reaction[1-55]. Thus, if such interaction can be realized in the mixture or composite  $MNH_2$ , the fast atomic diffusion indicated in the K system could be realized with higher hydrogen capacity.

#### ***1-4-2 Regeneration reaction of MH and NH<sub>3</sub> (Hydrogenation of MNH<sub>2</sub>)***

In the case of  $M-H$  system, the hydrogen absorption reaction must be exothermic reaction to realize a reversible hydrogen storage system according to the thermodynamics, while it is endothermic for  $MNH_2-H_2$  system. The Gibbs free energy change for the hydrogenation reaction is expressed as follows,

$$\Delta G = \Delta H_a - T\Delta S^0 - TR \ln \left( \frac{P_{H_2}}{P_{NH_3}} \right), \quad \Delta H_a > 0, \Delta S^0 > 0 \quad (1-30)$$

where  $\Delta H_a$ ,  $\Delta S^0$ ,  $R$ ,  $T$ ,  $P_{H_2}$ , and  $P_{NH_3}$  are the enthalpy change, the standard entropy change, the gas constant, temperature, partial pressure of hydrogen, and partial pressure of

ammonia, respectively. According to the thermodynamic equation (1-30) for the regeneration reaction of  $MNH_2$ - $H_2$  system, the third term includes three variable numbers of  $T$ ,  $P_{H_2}$ , and  $P_{NH_3}$ , whereas the third term of the thermodynamic equation (1-20) for  $M$ - $H$  system includes only two variable numbers of  $T$  and  $P_{H_2}$ . Therefore, even though the hydrogenation reaction of  $MNH_2$  to regenerate  $MH$  and ammonia is endothermic reaction, it can proceed under realistic temperature and pressure by controlling the third entropy term by reducing  $P_{NH_3}$ . In fact, it was experimentally clarified that hydrogenation of  $MNH_2$  can proceed under hydrogen flow condition in open system below 300 °C, where  $LiNH_2$ ,  $NaNH_2$ , and  $KNH_2$  require 300, 200, and 100 °C, respectively to obtain more than 70% of reaction yield[1-52].

As described above, it is essential to control the entropy change by reducing ammonia partial pressure to realize such lower reaction temperature. Thus, the investigation for hydrogenation reaction was performed under hydrogen flow condition in open system, however, such flow condition which exhausts unreacted hydrogen gas and generated ammonia gas was totally different from practical condition. Therefore, it is required to perform the hydrogenation reaction of  $MNH_2$  also in a practical way without any waste of hydrogen and generated ammonia.

## References

- [1-1] Statistical Review of World Energy 2014,  
<http://www.bp.com/en/global/corporate/about-bp/energy-economics/statistical-review-of-world-energy.html>.
- [1-2] Nuclear Technology Review 2014,  
[http://www.iaea.org/About/Policy/GC/GC58/GC58InfDocuments/English/gc58inf-4\\_en.pdf](http://www.iaea.org/About/Policy/GC/GC58/GC58InfDocuments/English/gc58inf-4_en.pdf).
- [1-3] UBE Nylon Resin Used in High-Pressure Hydrogen Tank of Toyota Mirai Fuel Cell Sedan, [http://www.ube-ind.co.jp/japanese/news/2014/20141208\\_01.htm](http://www.ube-ind.co.jp/japanese/news/2014/20141208_01.htm).
- [1-4] NIST, National Institute of Standards and Technology., <http://www.nist.gov/>.
- [1-5] Kawasaki Hevy Industries, L.,  
[http://www.khi.co.jp/knews/backnumber/bn\\_2005/pdf/news138\\_05.pdf](http://www.khi.co.jp/knews/backnumber/bn_2005/pdf/news138_05.pdf).
- [1-6] M.H. Mintz, S. Vaknin, S. Biderman, Z. Hadari, *Journal of Applied Physics*, **52 (1)** (1981) 463-467.
- [1-7] Y. Osumi, *Hydrogen storage alloy*, (1999).
- [1-8] J.J. Reilly, R.H. Wiswall, *Inorganic Chemistry*, **7 (11)** (1968) 2254-&.
- [1-9] P. Chen, Z.T. Xiong, J.Z. Luo, J.Y. Lin, K.L. Tan, *Nature*, **420 (6913)** (2002) 302-304.
- [1-10] T. Ichikawa, N. Hanada, S. Isobe, H.Y. Leng, H. Fujii, *J. Phys. Chem. B*, **108 (23)** (2004) 7887-7892.
- [1-11] T. Ichikawa, S. Isobe, N. Hanada, H. Fujii, *Journal of Alloys and Compounds*, **365 (1-2)** (2004) 271-276.
- [1-12] T. Ichikawa, N. Hanada, S. Isobe, H.Y. Leng, H. Fujii, *Journal of Alloys and Compounds*, **404** (2005) 435-438.
- [1-13] S. Isobe, T. Ichikawa, S. Hino, H. Fujii, *J. Phys. Chem. B*, **109 (31)** (2005) 14855-14858.
- [1-14] S. Hino, T. Ichikawa, N. Ogita, M. Udagawa, H. Fujii, *Chem. Commun.*, **(24)** (2005) 3038-3040.
- [1-15] H.Y. Leng, T. Ichikawa, S. Hino, N. Hanada, S. Isobe, H. Fujii, *J. Power Sources*, **156 (2)** (2006) 166-170.
- [1-16] H. Leng, T. Ichikawa, H. Fujii, *J. Phys. Chem. B*, **110 (26)** (2006) 12964-12968.
- [1-17] H.Y. Leng, T. Ichikawa, S. Hino, H. Fujii, *Journal of Alloys and Compounds*, **463 (1-2)** (2008) 462-465.
- [1-18] H.Y. Leng, T. Ichikawa, S. Hino, N. Hanada, S. Isobe, H. Fujii, *J. Phys. Chem. B*, **108 (26)** (2004) 8763-8765.

- [1-19] J.C. Ingersoll, N. Mani, J.C. Thenmozhiyal, A. Muthaiah, *J. Power Sources*, **173** (1) (2007) 450-457.
- [1-20] Y. Kojima, K. Suzuki, K. Fukumoto, M. Sasaki, T. Yamamoto, Y. Kawai, H. Hayashi, *International Journal of Hydrogen Energy*, **27** (10) (2002) 1029-1034.
- [1-21] P. Krishnan, T.H. Yang, W.Y. Lee, C.S. Kim, *J. Power Sources*, **143** (1-2) (2005) 17-23.
- [1-22] J.H. Wee, *J. Power Sources*, **155** (2) (2006) 329-339.
- [1-23] U.B. Demirci, O. Akdim, P. Miele, *International Journal of Hydrogen Energy*, **34** (6) (2009) 2638-2645.
- [1-24] Y. Kojima, T. Haga, *International Journal of Hydrogen Energy*, **28** (9) (2003) 989-993.
- [1-25] T. Schober, H. Wenzel, *Hydrogen in Metals II*, ed.G. Alefeld, J. Volkl, **29** (1978).
- [1-26] L. Schlapbach, *Hydrogen in Intermetallic Compounds I*, ed.L. Schlapbach, **63** (1988).
- [1-27] Y. Fukai, H. Sugimoto, *Advances in Physics*, **34** (2) (1985) 263-326.
- [1-28] Price of ammonia, [bsikagaku.jp/fertilizer-price/AM-price.pdf](http://bsikagaku.jp/fertilizer-price/AM-price.pdf).
- [1-29] Roadmap for hydrogen energy, [www.meti.go.jp/press/2014/06/.../20140624004-1.pdf](http://www.meti.go.jp/press/2014/06/.../20140624004-1.pdf).
- [1-30] H. Liu, *Chinese Journal of Catalysis*, **35** (10) (2014) 1619-1640.
- [1-31] R. Lan, J.T.S. Irvine, S.W. Tao, *International Journal of Hydrogen Energy*, **37** (2) (2012) 1482-1494.
- [1-32] N.D. Spencer, R.C. Schoonmaker, G.A. Somorjai, *Journal of Catalysis*, **74** (1) (1982) 129-135.
- [1-33] R. Schlogl, *Angewandte Chemie-International Edition*, **42** (18) (2003) 2004-2008.
- [1-34] K. Aika, A. Ozaki, H. Hori, *Journal of Catalysis*, **27** (3) (1972) 424-&.
- [1-35] L. Forni, D. Molinari, I. Rossetti, N. Pernicone, *Applied Catalysis a-General*, **185** (2) (1999) 269-275.
- [1-36] D.E. Brown, T. Edmonds, R.W. Joyner, J.J. McCarroll, S.R. Tennison, *Catalysis Letters*, **144** (4) (2014) 545-552.
- [1-37] I. Rossetti, N. Pernicone, L. Forni, *Applied Catalysis a-General*, **208** (1-2) (2001) 271-278.
- [1-38] Y. Inoue, M. Kitano, S.-W. Kim, T. Yokoyama, M. Hara, H. Hosono, *Acs Catalysis*, **4** (2) (2014) 674-680.
- [1-39] M. Kitano, Y. Inoue, Y. Yamazaki, F. Hayashi, S. Kanbara, S. Matsuishi, T. Yokoyama, S.-W. Kim, M. Hara, H. Hosono, *Nature Chemistry*, **4** (11) (2012)

934-940.

- [1-40] T. Arakawa, K. Takizawa, *Japan patent P2002 - 3209A*, **P2002 - 3209A** (2002)
- [1-41] M. Amblard, R. Burch, B.W.L. Southward, *Catalysis Today*, **59 (3-4)** (2000) 365-371.
- [1-42] A.S. Chellappa, C.M. Fischer, W.J. Thomson, *Applied Catalysis a-General*, **227 (1-2)** (2002) 231-240.
- [1-43] S.F. Yin, B.Q. Xu, X.P. Zhou, C.T. Au, *Applied Catalysis a-General*, **277 (1-2)** (2004) 1-9.
- [1-44] S.J. Wang, S.F. Yin, L. Li, B.Q. Xu, C.F. Ng, C.T. Au, *Appl. Catal. B-Environ.*, **52 (4)** (2004) 287-299.
- [1-45] B.X. Dong, T. Ichikawa, N. Hanada, S. Hino, Y. Kojima, *Journal of Alloys and Compounds*, **509** (2011) S891-S894.
- [1-46] N. Hanada, S. Hino, T. Ichikawa, H. Suzuki, K. Takai, Y. Kojima, *Chem. Commun.*, **46 (41)** (2010) 7775-7777.
- [1-47] F.W. Bergstrom, W.C. Fernelius, *Chemical Reviews*, **12 (1)** (1933) 43-179.
- [1-48] Y.H. Hu, E. Ruckenstein, *J. Phys. Chem. A*, **107 (46)** (2003) 9737-9739.
- [1-49] Y. Kojima, K. Tange, S. Hino, S. Isobe, M. Tsubota, K. Nakamura, M. Nakatake, H. Miyaoka, H. Yamamoto, T. Ichikawa, *J. Mater. Res.*, **24 (7)** (2009) 2185-2190.
- [1-50] H. Miyaoka, H. Fujii, H. Yamamoto, S. Hino, H. Nakanishi, T. Ichikawa, Y. Kojima, *International Journal of Hydrogen Energy*, **37 (21)** (2012) 16025-16030.
- [1-51] H. Miyaoka, T. Ichikawa, S. Hino, Y. Kojima, *International Journal of Hydrogen Energy*, **36 (14)** (2011) 8217-8220.
- [1-52] H. Yamamoto, H. Miyaoka, S. Hino, H. Nakanishi, T. Ichikawa, Y. Kojima, *International Journal of Hydrogen Energy*, **34 (24)** (2009) 9760-9764.
- [1-53] Y.L. Teng, T. Ichikawa, H. Miyaoka, Y. Kojima, *Chem. Commun.*, **47 (44)** (2011) 12227-12229.
- [1-54] F. Kraus, N. Korber, *Z. Anorg. Allg. Chem.*, **631 (6-7)** (2005) 1032-1034.
- [1-55] M.B. Ley, E. Roedern, T.R. Jensen, *Phys. Chem. Chem. Phys.*, **16 (44)** (2014) 24194-24199.

## 2 Purpose

The metal amide and hydrogen ( $MNH_2-H_2$ ) system is recognized as a promising reversible hydrogen storage system due to the high hydrogen capacity of 3.5-8.1 % and lower operating temperature than 300 °C as mentioned in Introduction. However, slow reaction rate for the Li system with the highest hydrogen capacity is an important issue to be solved for practical use. In this thesis, modification of the reaction properties for the  $LiNH_2-H_2$  system is carried out from thermodynamic and kinetic points of view. Particularly, the novel ammonia synthesis technique is proposed by using reaction of the  $LiNH_2-H_2$  system.

To modify the reaction properties of the  $LiNH_2-H_2$  system, lithium hydride-potassium hydride ( $LiH-KH$ ) complex system is proposed, where  $KH$  shows high reaction rate. This complex system attracts attention for improving the reactivity synergistically with a high gravimetric hydrogen density. Namely, the mixture or composite of  $LiNH_2$  and  $KNH_2$  as the reaction product of the  $LiH-KH$  complex with  $NH_3$  could show better reactivity such as fast atomic diffusion, as is common with eutectic phenomenon. Thus, in this work, the reaction properties of the  $LiH-KH$  and  $LiNH_2-KNH_2$  complexes are investigated in further detail.

A technique for ammonia synthesis technique from  $Li_3N$ , based on the reactions of “Amide-imide system” and “Amide-hydrogen system” is proposed. For the 2-step ammonia synthesis process, it is important to decrease the reaction temperature of the amide-hydrogen system, as it is endothermic reaction. Previously, it was clarified that the hydrogenation of  $MNH_2$  proceed below 300 °C under hydrogen flow condition, however, the reaction condition to exhaust all gases is far from practical condition. Thus, in this work, the hydrogenation reaction of  $LiNH_2$  in open system is investigated by preparing

various types of reaction systems which are closed gas circuit system and a closed system with gas exchange using hydrogen storage alloys, and then the feasibility of the ammonia synthesis process in such practical conditions is discussed.

### 3 Experimental procedures

#### 3-1 Sample preparation

##### 3-1-1 Materials

All the samples used for this study with their purity, state, and maker are listed in Table 3-1-1. All the samples were handled in a glove-box (Miwa MFG, MP-P60W) filled with Ar (>99.9999 %) to avoid oxidation and pollution due to water.

Table 3-1-1 General information of materials used in this study

Material	Purity, State	Company
Lithium hydride (LiH)	99.4 %, powder	Alfa aesar
Potassium hydride (KH)	unknown, powder dispersed in mineral oil	Aldrich
Lithium amide (LiNH <sub>2</sub> )	95 %, powder	Aldrich
Lithium nitride (Li <sub>3</sub> N)	99.5 %, powder	Aldrich
Potassium bromide (KBr)	>99 %, powder	Aldrich
Argon (Ar)	99.9999 %, gas	
Ammonia (NH <sub>3</sub> )	99.999 %, liquid	
Hydrogen (H <sub>2</sub> )	99.9999 %, gas	
Heavy hydrogen (D <sub>2</sub> )	99.6 %, gas	
Anhydrous-hexane (C <sub>6</sub> H <sub>14</sub> )	95 %, liquid	Aldrich

##### 3-1-2 Mechanical ball- milling method

By the mechanical ball-milling process, physical energy is given to a sample in collision between the balls and inner wall surface of the milling container. Thus, the mechanical milling process is applied to various purposes such as synthesis of alloys, mechanochemical reaction, synthesis of composite with close contact between components, dispersion of catalyst, formation of small particle, induction of defects, and so on.

Figure 3-1-1 shows the schematic view of the rotating (planetary) ball-milling apparatus (Fritsch, P7) and a milling container used for this study. The milling container with the inner volume of about 30 cm<sup>3</sup> is designed and made of Cr steel (UMETOKU Co. Ltd., SKD-11), where a quick connector (Swagelok:SS-QC4-D-2PM) can be connected to the container to introduce several kinds of gases into the container. The ball-milling for activation and synthesis of samples for this study was performed by following procedure,

- (i) 300 mg sample and twenty steel (SUJ-2) balls with 7 mm in diameter are introduced into the milling container in a glove-box, which are sealed by o-ring stuck between an inner cover and the upper part of the milling container.
- (ii) Ar in the milling container is evacuated by a rotary pump, and then 1.0 MPa H<sub>2</sub> is introduced through the Sievert's-type equipment as shown in Fig. 3-1-2.
- (iii) The ball-milling is performed by repeating a set of 1h milling and 30 min rest to avoid excess temperature increase, where a rotation rate is fixed at 370 rpm.

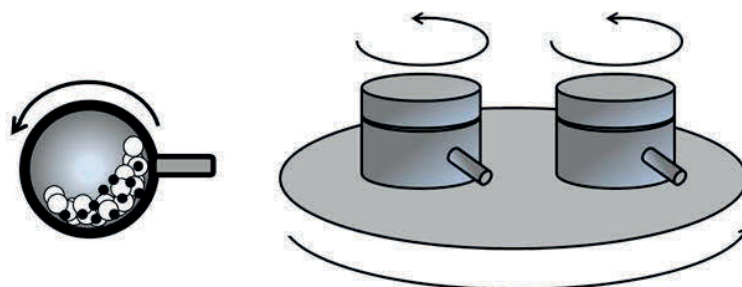


Figure 3-1-1 Schematic view of the planetary ball-milling apparatus.

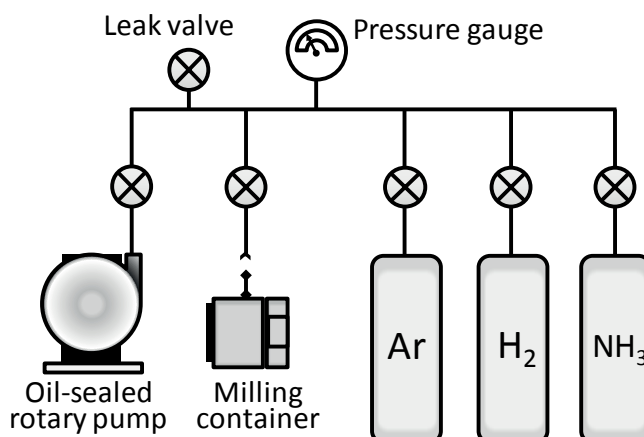


Figure 3-1-2 Schematic view of Sievert's-type equipment

### 3-1-3 Synthesis of samples

#### **KNH<sub>2</sub>**

KNH<sub>2</sub> was synthesized from potassium hydride (KH) and ammonia (NH<sub>3</sub>) by following procedure. First, KH powder stored in a mineral oil was washed by hydrous-hexane (95 %) in glove-box and vacuumed for a few hours to remove the remaining hexane completely. The washed KH powder was transferred into a metal container in the glove-box, and then NH<sub>3</sub> was introduced into this container cooled by liquid N<sub>2</sub>, thus not allowing the reaction to proceed at this moment. After that, the temperature of the container was increased to room temperature and the container was left for overnight to form KNH<sub>2</sub> by the reaction of KH with liquid NH<sub>3</sub>. After the reaction, remaining liquid NH<sub>3</sub> in the container was removed by trapping its vapor at an opposite part cooled with liquid N<sub>2</sub> as shown in Fig. 3-1-3.

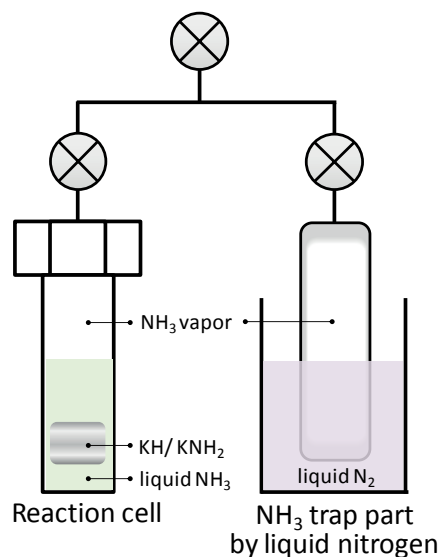


Figure 3-1-3 Schematic view of ammonia system for KNH<sub>2</sub> synthesis

### **MH complex**

Lithium hydride (LiH) and potassium hydride (KH) were used for the experiments. MH complex with a molar ratio of LiH/KH = 1 (= BM-(LiH-KH)), activated LiH (= BM-LiH), and activated KH (= BM-KH) were prepared by ball-milling for 10 h under 1.0 MPa of H<sub>2</sub> pressure using a planetary ball mill apparatus according to the process described in section 3-1-2. In addition, the milled samples were heat-treated at 220 °C under 1.0 MPa of H<sub>2</sub> pressure (= HT-(LiH-KH), HT-LiH, and HT-KH).

### **MNH<sub>2</sub> complex and MNH<sub>2</sub>-MH complex**

Potassium hydride (KH), lithium amide (LiNH<sub>2</sub>), potassium amide (KNH<sub>2</sub>) synthesized from KH and NH<sub>3</sub> were used for the experiments. MNH<sub>2</sub> complex with a molar ratio of LiNH<sub>2</sub>/KNH<sub>2</sub> = 1 (=BM-(LiNH<sub>2</sub>-KNH<sub>2</sub>)) and MH-MNH<sub>2</sub> complex with a molar ratio of LiNH<sub>2</sub>/KH = 1 (=BM-(LiNH<sub>2</sub>-KH)) were prepared by ball-milling for 10 h under 1.0 MPa of Ar pressure using a planetary ball mill apparatus.

## **LiND<sub>2</sub>-LiD mixture**

LiND<sub>2</sub>-LiD mixture with a molar ratio of LiD/LiND<sub>2</sub>=2 was synthesized from Lithium nitride (Li<sub>3</sub>N) and deuterium (D<sub>2</sub>) by following procedure. Li<sub>3</sub>N powder was introduced into a metal container, and then 0.5 MPa D<sub>2</sub> was introduced slowly over several hours to avoid excess exotherm with keeping the temperature of the container 200 °C.

The sample before and after each process was identified by X-ray diffraction (XRD) measurement (Rigaku, RINT-2100, CuKα radiation) and Fourier transform infrared spectroscopy (FT-IR) measurement (Perkin Elmer, Spectrum-One).

## **3-2 Experimental technique**

### ***3-2-1 Powder X-ray diffraction (XRD) measurement***

#### ***Principle***

X-ray structural analysis is realized by applying “Characteristic X-rays”. When the voltage applied to X-ray tube is increased over a certain value, quite sharp peak which has a substance-specific wavelength appears on the continuous X-ray spectrum as shown in Fig. 3-2-1. The sharp spectra are called characteristic X-rays because each spectrum shows a specific wavelength depending on the element of the metal. When an electron strikes a bound electron in an atom of a target with a sufficiently-high kinetic energy, the bound electron is ejected from the inner-shell of the atom, where the atom becomes an excited state with a vacant energy level, in other words, a core hole. Then, outer-shell electron falls into the vacant position in the inner shell to return to the static state and emit photon. The emitted photon has a specific wavelength depending on the difference of the

energy between the inner-shell and the outer-shell as shown in Fig. 3-2-2. Characteristic X-rays applied to X-ray structural analysis are generally  $K\alpha$  and  $K\beta$  of Cr, Fe, Co, Cu, and Mo. In this thesis, Cu- $K\alpha$  X-ray was used for XRD measurement. The intensity of characteristic X-ray is expressed by applied voltage  $V$ , current of X-ray tube  $i$ , excitation voltage of characteristic X-ray  $V_K$ , proportional constant  $B$ , and constant number  $n$  which is about 1.5 as follows,

$$I_K = Bi(V - V_K)^n. \quad (3-1)$$

Regarding powder X-ray diffraction (XRD) measurement, it is possible to identify a crystalline material and obtain information of crystalline structure such as crystal system, lattice constant, and others by analyzing the X-ray diffraction result for powder sample. The X-ray structural analysis is a comparatively easy method and well-known as commonly-used technique to estimate a structure characteristic of a solid phase material.

When crystal plane with a lattice spacing  $d$  is irradiated with monochromatic X-ray of wavelength  $\lambda$  at an incident angle  $\theta$ , the scattered X-rays from different crystal planes are coherent to each other and interface constructively. This leads to “Bragg’s law” and can be expressed as follows,

$$n\lambda = 2d_{hkl} \sin \theta, \quad (3-2)$$

where  $hkl$  are Miller indexes and  $d_{hkl}$  is the distance between the places. Thus, X-ray diffraction pattern reflecting the crystal structure is obtained by scanning the diffraction angle  $2\theta$  as shown in Figure 3-2-3.

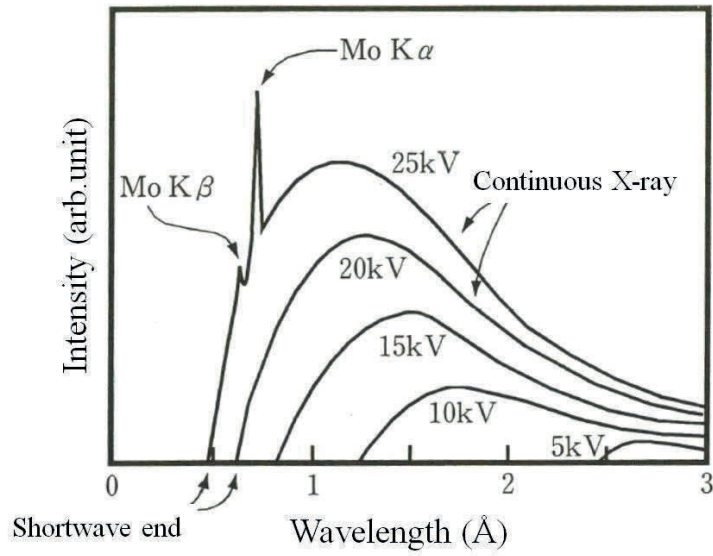


Figure 3-2-1 X-ray spectrum generated from molybdenum X-ray tube[3-1].

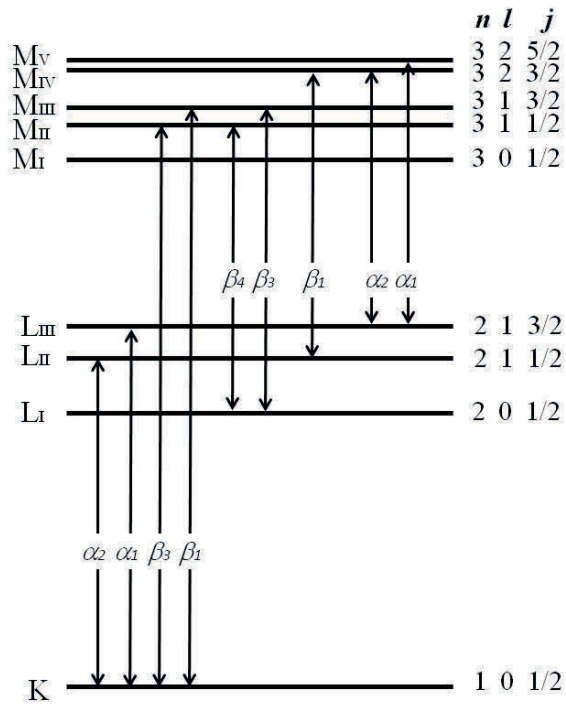


Figure 3-2-2 Relationship diagram between energy levels of electron shells and characteristic X-rays[3-1]

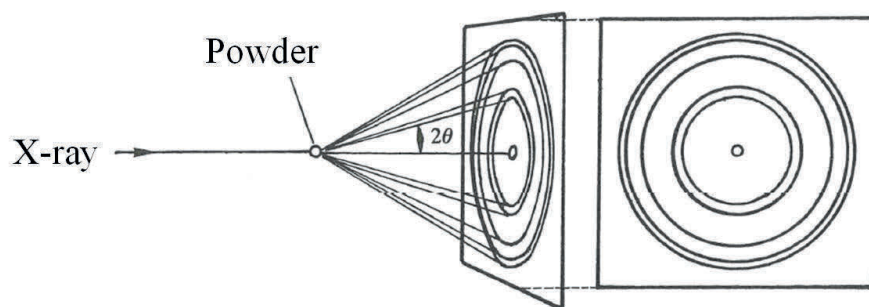


Figure 3-2-3 Aspect of powder X-ray diffraction measurement[3-2].

### ***Procedure***

In this work, powder XRD measurement for all of the samples were performed to identify the phases of the samples by using conventional X-ray diffractometer (Rigaku RINT 2000), equipped with Cu- $K\alpha$  ( $\lambda=1.54 \text{ \AA}$ ) X-ray source with the output energy of 8 kW (40 kV, 200 mA). The sample was spread on a glass plate and adhered to it using a high vacuum grease (Apiezon® Grease, M&I Material Ltd.). The sample was then covered with a polyimide sheet (8  $\mu\text{m}$  thickness, Kapton®, Du Pont-Toray Co., Ltd.) to avoid oxidation of the sample. The obtained XRD patterns were analyzed by using a software (PDXL) and powder diffraction files in the database.

### ***3-2-2 Fourier transform infrared (FT-IR) spectroscopy***

#### ***Principle***

Atoms that constitute a molecule, vibrate consistently while keeping their chemical bonds; this is known as “molecular vibration”. Since the energy of the molecular vibration is equivalent to the energy of infrared region, the molecule absorbs specific frequencies in the region according to its structure, resulting in their excitation from low energy state ( $E_h$ ) to high energy one ( $E_l$ ). The energy transition of the vibration mode in molecule can be expressed as follows,

$$h\nu = E_h - E_l, \quad (3-3)$$

where  $h$  is Planck constant and  $\nu$  is frequency.

Thus, infrared absorption spectra show information about the binding state of the atoms that constitute a molecule, in other words, the functioning group.

In the case of a diatomic molecule, these atoms vibrate along the straight-line between them, which is called “stretching vibration”. Regarding to a polyatomic molecule, it shows a variety of vibration modes such as “bending vibration” and “twisting vibration”. Herein, three vibration modes for  $\text{H}_2\text{O}$  molecule are shown in Fig. 3-2-4 (a) as an example, where  $\nu_1$ ,  $\nu_2$ , and  $\nu_3$  are called “OH-symmetric stretching vibration”, “HOH-bending vibration”, and “OH-asymmetric stretching vibration”, respectively. Besides, the wavenumber of these vibration modes for  $\text{H}_2\text{O}$  and  $\text{D}_2\text{O}$  are shown in Table 3-2-1. The important points in the table are listed as follows.

- Although the wavenumber of asymmetric stretching vibration is larger than that of symmetric stretching vibration, these are approximately the same.
- The wavenumber of bending vibration is much smaller than that of stretching vibration.
- For all of the vibration modes, there are a certain difference of the wavenumber between  $\text{H}_2\text{O}$  and  $\text{D}_2\text{O}$ .
- For all of the vibration modes, there are a certain difference of the wavenumber between liquid phase and gaseous phase due to the hydrogen bond for liquid phase.

In order to understand the difference between  $\text{H}_2\text{O}$  and  $\text{D}_2\text{O}$ , a simple spring model is introduced as shown in Fig. 3-2-5. Regarding the motional state, the frequency of the vibration is expressed by “Hooke’s law” as follows,

$$\nu = \frac{1}{2\pi} \sqrt{\frac{k}{\mu}}, \quad (3-4)$$

$$\mu = \frac{m_1 m_2}{m_1 + m_2}, \quad (3-5)$$

where  $\nu$  is frequency,  $m_1$  and  $m_2$  are mass of each atom,  $k$  is the force constant, and  $\mu$  is effective mass. Therefore, in the case of a deuterated sample, the IR absorption peak is shifted to lower energy than that of the hydrogenated sample, because  $\mu$  is larger than of hydrogenated sample.

When the number of atoms in a molecule is  $N$ , the number of vibration mode is  $3N-6$  for non-linear molecule, and  $3N-5$  for liner molecule, which are estimated by subtracting the translational degree of freedom ( $x$ ,  $y$ ,  $z$  axis) for each atom from the translational and rotational degree of freedom for the molecule. However, not every vibration mode shows an IR absorption spectrum, namely; only vibration mode associated with the change in dipole moment shows the IR absorption phenomenon. The requirement is related closely to the molecule structure and the symmetric property of the vibration mode. In the vibration modes of  $H_2O$  molecule,  $\nu_1$  and  $\nu_2$  are regarded as “totally-symmetric vibration”, and  $\nu_3$  is regarded as “asymmetric vibration”. Since all the vibration in  $H_2O$  molecule occurs through change in dipole moment, all the vibrational modes shows IR absorption and can be termed as IR-active. On the other hand, in the case of  $CO_2$  molecule of which vibration modes are shown in Fig 3-2-4 (b), the symmetric stretching mode  $\nu_1$  is not IR active because the dipole moment doesn't change.

The frequency of the molecule vibration corresponding to the functional group is remained almost constant, even though the molecule becomes more complicated; the frequency is known as “characteristic absorption” or “group frequency”. Therefore, these

group frequencies are widely used in the IR absorption spectroscopy for the identification of functional groups and are listed in the Table 3-2-2[3-3].

Table 3-2-1 The wavenumber of the vibration modes for H<sub>2</sub>O and D<sub>2</sub>O

	$\nu_1$	$\nu_2$	$\nu_3$
H <sub>2</sub> O (gas)	3654.5	1595	3755.8
H <sub>2</sub> O (liquid)	3210	1650	3430
D <sub>2</sub> O (gas)	2668	1178.7	2789
D <sub>2</sub> O (liquid)	2512	1220	2630

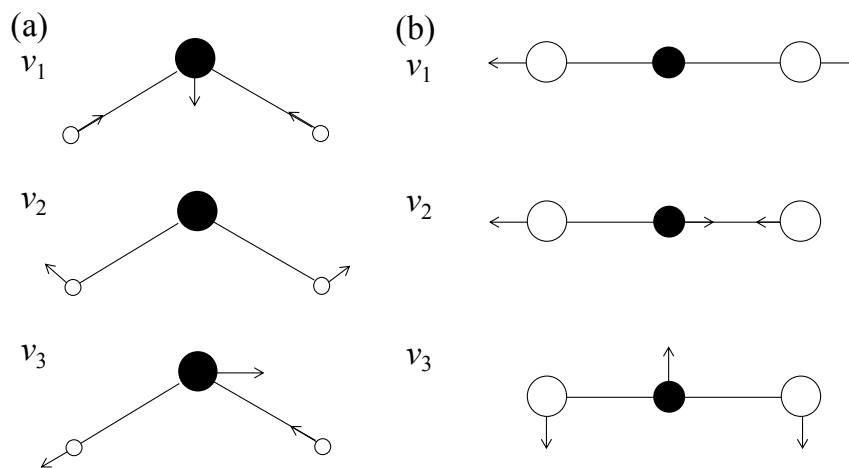


Figure 3-2-4 Vibration modes for H<sub>2</sub>O molecule (a) and CO<sub>2</sub> (b).

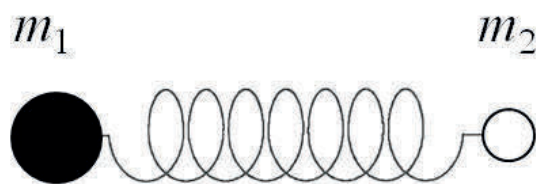


Figure 3-2-5 Schematic view of stretching vibration for diatomic molecule.

Table 3-2-2 Typical group frequencies

Functional Group	Characteristic Absorptions ( $\text{cm}^{-1}$ )
<b>OH stretching vibration</b>	
H-bonded	3650~3590
free	~3000
<b>NH stretching vibration</b>	
H-bonded	~3000
free	3500~3200
<b>CH stretching vibration</b>	
$\text{CH}_3$	~2960, ~2870
$\text{CH}_2$	~2930, ~2850
CH	~2890
CH=	3040~3010
$\text{CH}_2=$	3095~3075, 2985~2965
$\text{CH}\equiv$	3300
CH (Aromatic)	~3030
<b><math>\text{C}\equiv\text{C}</math> stretching vibration</b>	1974 ( $\text{HC}\equiv\text{CH}$ ), 2420~2310
<b><math>\text{C}\equiv\text{N}</math> stretching vibration</b>	2089 ( $\text{HC}\equiv\text{N}$ ), 2280~2230
<b><math>\text{C}=\text{C}</math> stretching vibration</b>	1680~1630
<b><math>\text{C}=\text{N}</math> stretching vibration</b>	1680~1610
<b><math>\text{C}=\text{O}</math> stretching vibration</b>	
Ketone	1715 ( $\text{CH}_3\text{COCH}_3$ ) 1760~1660
acid, Aldehyde, Ester	1710 ( $\text{CH}_3\text{COOH}$ ) 1820~1660
<b><math>\text{CH}_3</math>, <math>\text{CH}_2</math> bending vibration</b>	1480~1380
<b>C-Halide stretching vibration</b>	
C-F	1400~1000
C-Cl	800~600
C-Br	700~500
C-I	~500

### ***Procedure***

The Fourier transform infrared (FT-IR) spectroscopy measurement (Spectrum One Perkin-Elmer) was performed at room temperature by using a diffuse reflection cell to investigate the IR active stretching modes of the groups such as N-H bonds in the solid powder sample. Each sample was hand-milled and mixed with potassium bromide (KBr) by using a pestle mortar in a glove box. The sample diluted down to 5mass% was packed into aluminium (Al) pan, and then the Al pan with the sample was introduced and sealed into the diffuse reflection cell with IR silent KBr window on top. Before measuring the sample, background of IR spectra was assessed by measuring a KBr powder without any samples. Thus, IR spectrum for the sample without the background spectrum was obtained.

### ***3-2-3 Differential scanning calorimetry (DSC)***

#### ***Principle***

For the DSC (Differential scanning calorimetry) measurement, calorimetric measurement is performed in addition to temperature measurement for DTA (Differential thermal analysis). As shown in Fig. 3-2-6, a sample cell and a reference cell are placed in a furnace, then the furnace temperature is increased at a fixed heating rate. The profiles of the temperature variation with time for the sample cell ( $T_S$ ), the reference cell ( $T_R$ ), and the furnace ( $T_P$ ) are shown in Fig. 3-2-7 (a). The temperatures  $T_S$  and  $T_R$  increase at fixed rate along with the temperature increase in  $T_P$  at the static state after the orientation time, which is expressed as follows,

$$\frac{dT_P}{dt} = \frac{dT_R}{dt} = \frac{dT_S}{dt}. \quad (3-6)$$

At a certain time in the static state, heat transfer  $q_s$  per unit of time from the furnace to the sample cell, as it is called heat flux  $dq_s/dt$ , is expressed by “Newton’s law of cooling” as follows,

$$\frac{dq_s}{dt} = \frac{1}{R}(T_p - T_s). \quad (3-7)$$

The equation (3-7) shows that thermal flux is proportional to the temperature difference between the sample cell and the furnace, where the proportional constant is given by inverse of thermal resistance  $R$  between the sample cell and the furnace. The thermal resistance is usually regarded as an apparatus constant depending on the furnace and the cell, which is given by inverse of heat conduction coefficient. Besides, heat flux  $dq_R/dt$  from the furnace to the reference cell is given in a similar way as follows,

$$\frac{dq_R}{dt} = \frac{1}{R}(T_p - T_R). \quad (3-8)$$

Herein, following equation is given by subtracting equation (3-8) from equation (3-7) as follows,

$$\begin{aligned} \frac{dq_s}{dt} - \frac{dq_R}{dt} &= -\frac{1}{R}(T_s - T_R), \\ \therefore \frac{d\Delta q}{dt} &= -\frac{1}{R}\Delta T. \end{aligned} \quad (3-9)$$

$\Delta T$  against time is measured with a thermocouple as shown in Fig. 3-2-7 (b). Furthermore, the relation between the temperature difference ( $\Delta T$ ) and thermoelectric power ( $\Delta E$ ) is expressed as follows,

$$\Delta E = S_{AB}\Delta T, \quad (3-10)$$

where  $S_{AB}$  is given by difference between the thermopowers of the couple of thermoelements ( $S_A - S_B$ ). Thus, equation (3-9) is transcribed by  $\Delta E$  as follows,

$$\frac{d\Delta q}{dt} = -\frac{1}{R \cdot S_{AB}}\Delta E. \quad (3-11)$$

By this means, the measured value of the  $\Delta E$  is converted to  $d\Delta q/dt$ . As a result,  $d\Delta q/dt$  plot against time is given as shown in Fig. 3-2-7 (c).

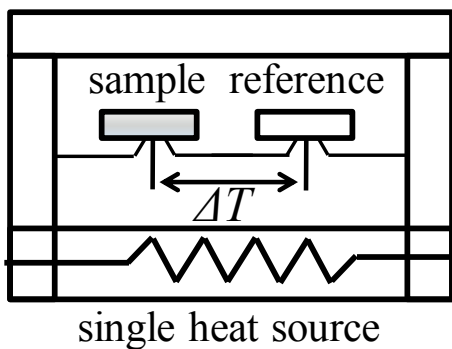


Figure 3-2-6 Heat-flux DSC

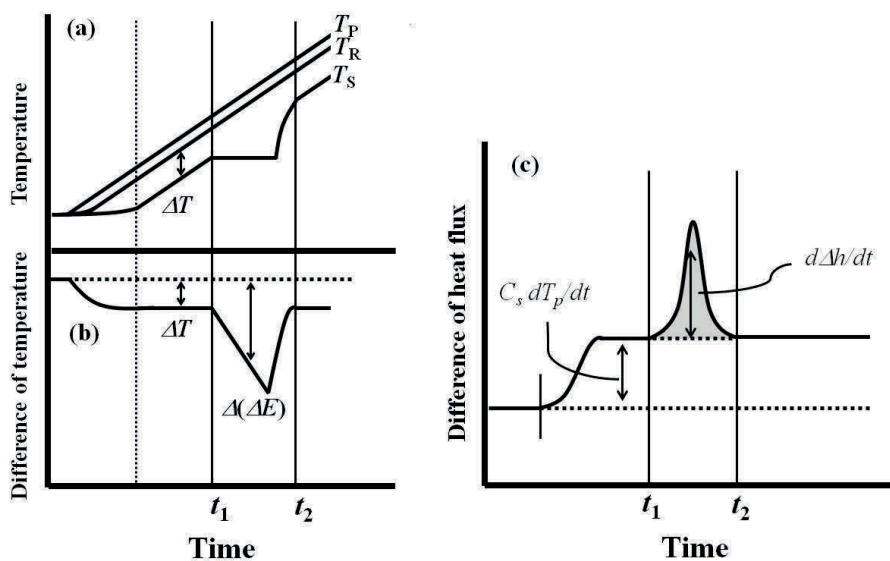


Figure 3-2-7 Time variation of temperature of furnace  $T_P$ , reference cell  $T_R$ , and sample cell  $T_S$  (a), time variation of temperature difference between reference cell and sample cell  $\Delta T$  (b), and time variation of difference of heat flux between reference cell and sample cell ( $d\Delta q/dt$ ) (c) .

### ***Procedure***

Differential scanning calorimetry (DSC) (TA Instruments, Q10 PDSC) measurement was performed in a glove-box to avoid exposing the sample to air. The thermal properties of  $\text{LiK}(\text{NH}_2)_2$  and  $\text{LiNH}_2\text{-KH}$  complex were investigated by DSC with an alumina ( $\text{Al}_2\text{O}_3$ ) pan under 0.1 MPa Ar atmosphere and 0.5 MPa  $\text{H}_2$  atmosphere, respectively, where the heating rate was fixed to be 5 °C/min in the temperature range from room temperature to 250~270 °C. The products after the DSC measurements were identified by XRD measurement.

Hydrogenation reaction of  $\text{LiK}(\text{NH}_2)_2$  was investigated by DSC with an aluminium (Al) pan under 0.5 MPa  $\text{H}_2$  flow condition, where the flow rate was 200 sccm (= cc/min at 0.1 MPa, 0 °C) and the heating rate was fixed to be 5 °C/min in the temperature range from room temperature to 160 °C and 220 °C. The weights of the samples before and after hydrogenation reaction were measured to estimate the reaction yield. The reaction products were identified by XRD measurement.

Hydrogenation reaction of  $\text{Li}_3\text{N}$  was investigated by DSC with an aluminium (Al) pan under 0.5 MPa  $\text{H}_2$  flow condition, where the flow rate was 200 sccm (= cc/min at 0.1 MPa, 0 °C) and the heating rate was fixed to be 1 °C/min in the temperature range from room temperature to 300 °C. The reaction products were identified by XRD measurement.

### ***3-2-4 Thermal desorption mass spectroscopy (TDMS)***

#### ***Principle***

In this study, thermal gases desorption profiles during DSC measurement are given by thermal desorption mass spectroscopy (TDMS) connected to the DSC apparatus. Fig. 3-2-8 shows the schematic view of the TDMS apparatus used for this thesis. This apparatus

includes an ionization source, a linear quadruple mass spectrometer, and a detector. A turbomolecular pump is used to maintain ultra-high vacuum condition in the TDMS chamber. As the first step for the TDMS measurement, the gaseous molecules desorbed from the sample during DSC measurement are ionized at the ionization part by interaction with energetic electrons which are accelerated and concentrated into a beam. Then, the ionized gas molecules are separated by difference of mass-to-charge ratio (=  $m/z$ ) in the quadruple mass spectrometer, where the generated molecular ions with excess internal energy split to fragment ions. Fig. 3-2-9 shows the schematic view of the quadruple mass spectrometer. The spectrometer is composed of two twin electrodes, where the voltage applied to the electrodes  $\Phi_0$  was expressed by direct current (DC) component  $U$ , amplitude of alternating-current (AC) component  $V$ , and frequency of AC  $\omega$  as follows,

$$\Phi_0 = U + V \cos \omega t . \quad (3-12)$$

Herein, the molecular ions can pass through the electrodes, provided that  $m/z$  can be expressed as following equations by the incircle radius of quadruple electrodes  $r_0$  and frequency of voltage  $f$  ,

$$\frac{m}{z} = \frac{1}{7.22} \frac{V}{r_0^2 \cdot f^2} , \quad (3-13)$$

$$f = \frac{\omega}{2\pi} . \quad (3-14)$$

Therefore,  $m/z$  value of a certain ion which passes through the quadruple electrodes is scanned from the higher to the lower value by varying  $U$  and  $V$  values with keeping  $U/V$  value constant. Finally, the ions which pass through the quadruple electrodes are detected by a detector.

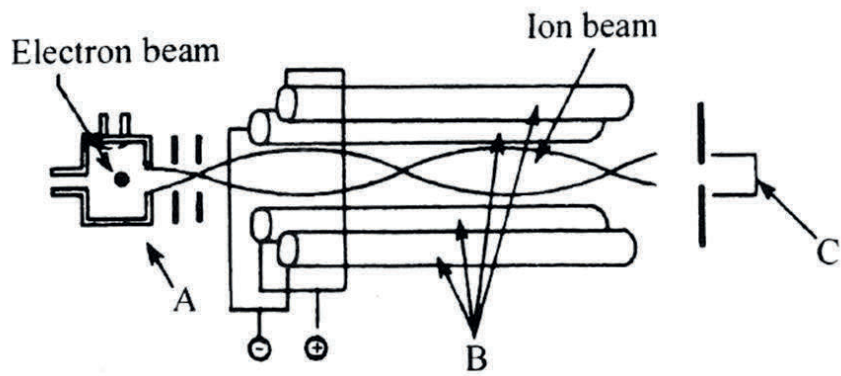


Figure 3-2-8 TDMS apparatus (A:ionization source, B:quadruple mass spectrometer, C:detector)[3-4].

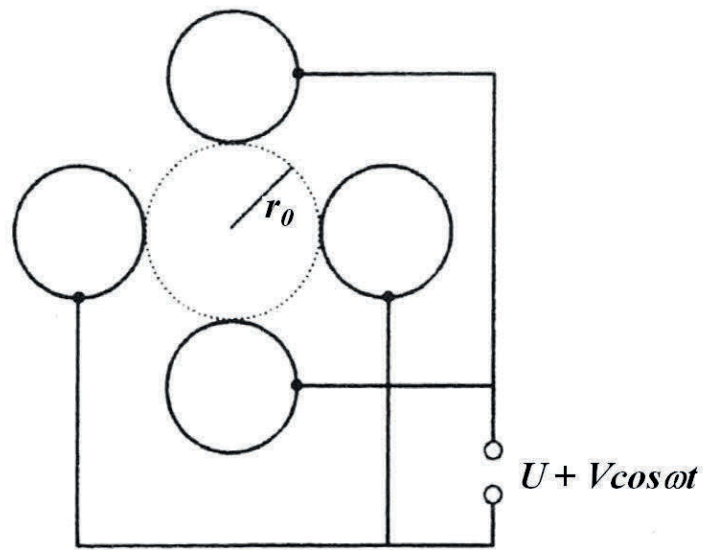


Figure 3-2-9 Quadruple mass spectrometer[3-4].

### **Procedure**

Thermal gas desorption properties under H<sub>2</sub> flow condition of Li<sub>3</sub>N, LiNH<sub>2</sub>, and LiK(NH<sub>2</sub>)<sub>2</sub> were performed by TDMS apparatus (Anelva, M-QA200TS) connected to the DSC equipment. In the DSC-MS measurement, high purity H<sub>2</sub> gas was flowed for the hydrogenation reaction of the all samples. The heating rate was 1 or 5 °C/min in accordance with the heating rate of the DSC measurement.

### **3-2-5 Ammonolysis reaction of MH**

#### **Principle**

Metal hydride (s) reacts with NH<sub>3</sub> (g) even at room temperature, forming MNH<sub>2</sub> (s) and H<sub>2</sub> (g) in a closed system, where the maximum pressure of NH<sub>3</sub> at room temperature (20 °C) is 0.857 MPa, which is introduced by using the Sievert's-type equipment as shown in Fig. 3-1-2. The weight of the solid sample increases with the progression of the reaction because solid MH reacts to form solid MNH<sub>2</sub>. Thus, the reaction yield (Y) can be estimated from the weight gain ( $\Delta m_g$ ) by following equation,

$$Y(\%) = \frac{100 \cdot M_{MH} \cdot \Delta m_g}{15.01 \cdot m_1}, \quad (3-15)$$

where  $m_1$  is the weight of the MH before reaction, and  $M_{MH}$  is molecular weight of MH. Besides, the reaction yield of hydrogenation reaction of MNH<sub>2</sub> can also be estimated from weight decrease ( $\Delta m_d$ ) during the reaction by following equation,

$$Y(\%) = \frac{100 \cdot M_{MNH_2} \cdot \Delta m_d}{15.01 \cdot m_2}, \quad (3-16)$$

where  $m_2$  is the weight of the MNH<sub>2</sub> before reaction, and  $M_{MNH_2}$  is molecular weight of MNH<sub>2</sub>.

### ***Procedure***

BM-*MH* and HT-*MH* (*MH*: LiH, KH, LiH-KH) were used as starting material for the experiments. The hydrogen generation properties were investigated in a closed system at room temperature by following procedure. First of all, a weighed amount of *MH* was loaded into a reaction cell in the glove box, then 0.8 MPa NH<sub>3</sub> with a molar ratio of NH<sub>3</sub>/*MH* = 1 was introduced in the cell, thus allowing the reaction of *MH* with NH<sub>3</sub> for 360 min as the total time. However, the process was interrupted at a duration of 10, 60, 180 min by evacuating the chamber. The weight gain of the sample was measured to estimate the reaction yield every time. After that, the reactor was again refilled with the same amount of NH<sub>3</sub> as the initial one. The products after hydrogen generation reaction were identified by XRD and FT-IR measurements.

## References

- [3-1] Y. Waseda, E. Matsubara, *Zairiyogaku series X-ray structural analysis*, ed.M. Dobayashi, (1998).
- [3-2] S. Lesley, M. Elaine, *SOLID STATE CHEMISTRY (Japanese translation)*, ed.R. Sone, K. Komoto, K. Hirao, (2006).
- [3-3] T. Hirokawa, *Instrumental Analysis Chemistry* ed.T. Tsuda, T. Hirokawa, (2004).
- [3-4] S. Tanaka, Y. Iida, *Instrumental Analysis, Shokabo (Japanese)*, (2000).

## 4 Results and discussion

### 4-1 Hydrogen generation reaction of metal hydride complex with ammonia

#### 4-1-1 Synthesis of LiH-KH complex

MH (LiH-KH) complex and activated MH (LiH, KH) were prepared by mechanical ball-milling method for investigation of ammonolysis reaction. Fig. 4-1-1 shows X-ray diffraction patterns of as prepared LiH, as prepared KH, BM-LiH (activated LiH), BM-KH (activated KH), and BM-(LiH-KH) (LiH-KH complex). By the ball-milling, the diffraction peaks corresponding to LiH and KH are weakened and broadened due to a decrease of the crystallite size and the crystal distortion, which possibly influences the reaction kinetics of the ammonolysis reaction. Especially, BM-(LiH-KH) showed remarkable difference from the hydrides before ball-milling. It is noteworthy that the peaks of LiH are not observed even though BM-LiH showed clear peaks, and the intensity reduction and broadening of peaks assigned to KH are more obvious. To explain these results, following two possibilities are considered. When the two kinds of materials are milled together, the ball-milling effects could be changed, suggesting that the ball-milling effects to LiH-KH are enhanced each other by coexistence of both materials. As another possibility, the formation of LiH-KH compound phase is expected by “mechanical alloying” effect because LiH and KH are similar ionic crystal with 1:1 ratio of alkali metal cation and H<sup>-</sup>. Therefore, we call BM-(LiH-KH) as LiH-KH complex.

As mentioned above, these MH prepared by ball-milling are expected to be in the activated state due to small crystalline size and structural distortion. However, such active state would be lost after the repeated practical uses of MH-NH<sub>3</sub> due to heat treatment at 200 °C needed for the regeneration of MNH<sub>2</sub>. In order to evaluate the influence of such milling effects and to know the essential properties, BM-LiH, BM-KH, and BM-(LiH-

KH) were heat-treated at 220 °C, which was chosen as a possible temperature to regenerate amide phases and, to restore the structural disorder by the crystallization. The heat-treated samples are denoted as HT-LiH, HT-KH, and HT-(LiH-KH). It is confirmed that the observed diffraction peaks of all the samples are sharpened with higher intensities as those before the ball-milling process, shown in Fig. 4-1-2. On the other hand, the peaks corresponding to LiH are quite weak in the profile of HT-(LiH-KH).

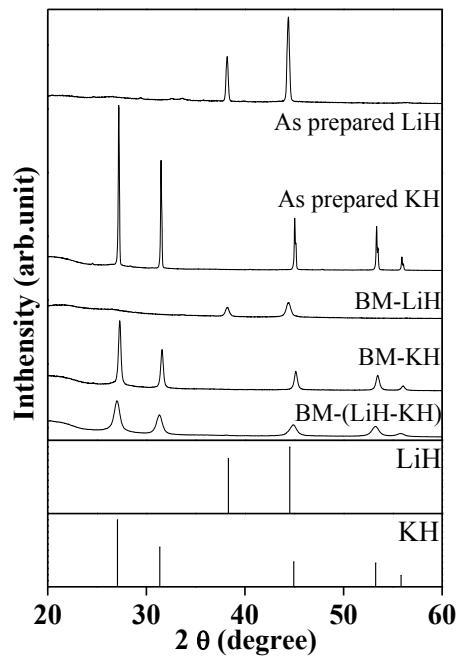


Figure 4-1-1 XRD patterns of the as prepared hydrides and the ball milled samples; XRD pattern of LiH (PDF#78-0838) , KH (PDF#65-9244) are referred from databases.

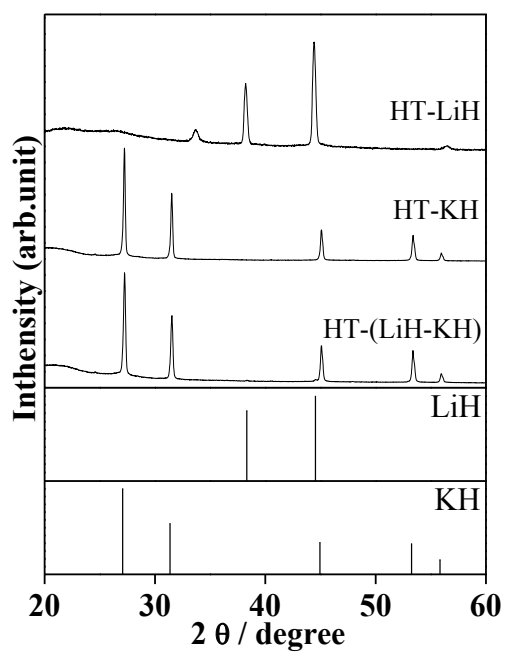


Figure 4-1-2 XRD patterns of the heat-treated samples after the ball milling; XRD pattern of LiH (PDF#78-0838), KH (PDF#65-9244) are referred from databases.

#### ***4-1-2 Hydrogen generation reaction of LiH-KH complex with ammonia***

Fig. 4-1-3 shows reaction yields as a function of the reaction time for the hydrogen generation reaction of BM-LiH, BM-KH, and BM-(LiH-KH) with NH<sub>3</sub> at room temperature. In this figure, the reaction yield of the simple mixture of BM-LiH and BM-KH (LiH/KH = 1 mol/mol) calculated from the results of each ball-milled hydride ( $= 0.5 \times$  reaction yield of BM-LiH +  $0.5 \times$  reaction yield of BM-KH) is also plotted for the comparison, which is shown as dotted line in the figure, to evaluate the reaction rate of BM-(LiH-KH). The reaction yields for 10 min of BM-LiH, BM-KH, and BM-(LiH-KH) are 18.9, 84.1, and 40.7% respectively. The reaction rate is found to be increased in the order of periodic table of alkali metal (Li<Na<K), which is consistent with the previous results[4-1]. The reaction yield of 40.7% for BM-(LiH-KH) is 10.8 % lower than the expected reaction yield of 51.5 % ( $=0.5 \times 18.9 \% + 0.5 \times 84.1 \%$ ). On the other hand, the reaction yields for 360 min of BM-LiH, BM-KH, and BM-(LiH-KH) are 80.2 %, 98.7 % and 98.0%, respectively. The reaction yield of BM-(LiH-KH) significantly increased and then it is found to be 8.5 % higher than the expected reaction yield as 89.5 % ( $= 0.5 \times 80.2 \% + 0.5 \times 98.7 \%$ ). From these results, it is noted that the LiH-KH complex showed a characteristic reactivity with NH<sub>3</sub>. Considering the reaction process for the solid-gas reaction in the NH<sub>3</sub>-MH system, it is expected that the reaction rate at initial and late stages are controlled by the surface reaction and NH<sub>3</sub> diffusion in the product, respectively. Thus, the higher diffusion rate, namely higher solubility of NH<sub>3</sub> into the amide as the reaction product, than the LiH-NH<sub>3</sub> system would be realized by the formation of the LiNH<sub>2</sub>-KNH<sub>2</sub> complex.

Fig. 4-1-4 shows diffraction patterns of the products after the reaction of BM-LiH, BM-KH, BM-(LiH-KH) with NH<sub>3</sub>. The diffraction patterns for the reaction products of BM-

LiH with  $\text{NH}_3$  showed  $\text{LiNH}_2$  phase, where diffraction peak of remaining LiH could not be observed due to its relatively weak intensity. The diffraction patterns for the reaction products of BM-KH with  $\text{NH}_3$  showed only  $\text{KNH}_2$  phase without KH phase, indicating that the reaction was almost completed. On the other hand, in the diffraction pattern of the reaction product of BM-(LiH-KH) with  $\text{NH}_3$ , unknown phase appeared, where the observed peaks did not match with any known structures i.e.  $\text{K}_2\text{Li}(\text{NH}_2)_3$ ,  $\text{KLi}(\text{NH}_2)_2$ ,  $\text{KLi}_3(\text{NH}_2)_4$ , and  $\text{KLi}_7(\text{NH}_2)_8$  reported so far[4-2, 3] and others listed in the ICDD database. Besides, the peak intensity of the unknown phase is relatively weak compared with the products of BM-LiH and BM-KH with  $\text{NH}_3$ . In order to characterize the unknown phase, FT-IR measurement for the product was performed. Fig. 4-1-5 shows the IR spectra of as prepared  $\text{LiNH}_2$ ,  $\text{KNH}_2$ , and the reaction product of BM-(LiH-KH) with  $\text{NH}_3$ . The two absorption peaks observed in the energy range corresponds to stretching mode of the  $-\text{NH}_2$  group, and the positions are inherent of the materials. The peaks observed in the spectra of the product after the reaction of BM-(LiH-KH) with  $\text{NH}_3$  are not equivalent to those of either  $\text{LiNH}_2$  or  $\text{KNH}_2$ , indicating that a different amide phase such as double-cation amide compound ( $\text{LiK}(\text{NH}_2)_2$ ) could be formed by the reaction of LiH-KH complex with  $\text{NH}_3$ . This behavior is consistent with the XRD result.

Fig. 4-1-6 shows the reaction yields as a function of the time for the hydrogen generation reaction of HT-LiH, HT-KH, and HT-(LiH-KH) with  $\text{NH}_3$  at room temperature. Here, the dotted line shows expected reaction yield. The reaction yields of HT-LiH at 10, 60, 180, and 360 min are 16.2, 39.4, 64.6, and 81.8 % which are almost similar to the reaction yields of BM-LiH as 18.9, 50.7, 69.2 and 80.2 % at the same reaction time. Similarly, the reaction yields of HT-KH reveal almost the same reaction yields of BM-KH for each reaction time. On the other hand, the reaction yields of HT-(LiH-KH) at 10,

60, 180, and 360 min are 67.3, 96.9, 97.5, and 98.1%, which are clearly higher than expected ones. It is noteworthy that the reaction yield of HT-(LiH-KH) for 60 min is found to be 96.9 %, which is 28.7 % higher than the expected reaction yield as 68.2 % ( $= 0.5 \times 39.4 \% + 0.5 \times 96.9 \%$ ). Interestingly, although the reaction yields of HT-LiH and HT-KH were almost the same or slightly lowered compared with the ball milled samples, the reaction rate of the heat treated LiH-KH complex (HT-(LiH-KH)) is dramatically higher than BM-(LiH-KH) at all the reaction time. Diffraction pattern and IR spectrum corresponding to the product after the reaction of HT-(LiH-KH) with  $\text{NH}_3$  showed no difference from those of the reaction product of BM-(LiH-KH) with  $\text{NH}_3$  samples as shown in Fig. 4-1-7 and Fig. 4-1-8, respectively. Thus, it is considered that slow reaction rate in the initial-stage of the ball milled LiH-KH complex could be improved by restoring the crystalline disorder by thermal crystallization, resulting in high reactivity with  $\text{NH}_3$  similar to the KH system.

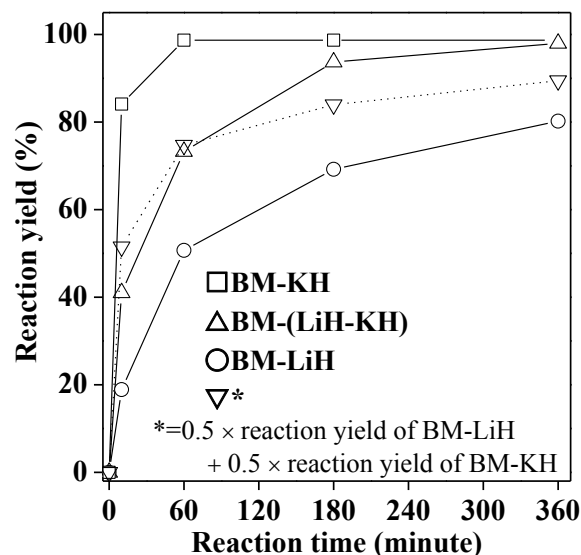


Figure 4-1-3 Hydrogen generation profiles for the reactions of BM-MH with  $\text{NH}_3$ . The broken line is the expected reaction yield of BM-(LiH-KH) without interaction each other (\* =  $0.5 \times$  reaction yield of BM-LiH +  $0.5 \times$  reaction yield of BM-KH).

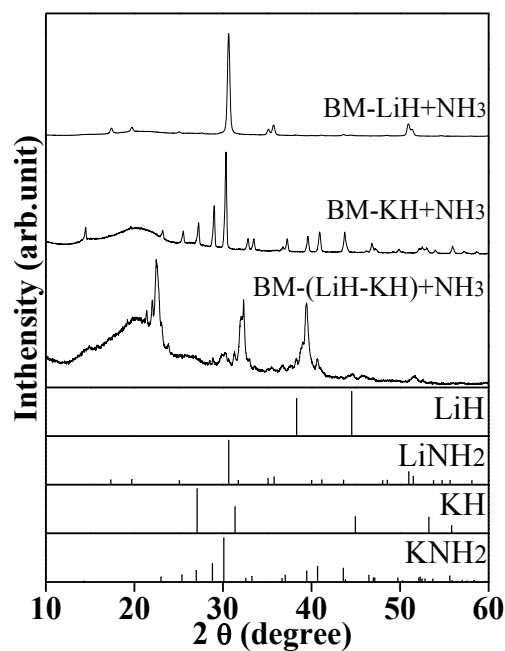


Figure 4-1-4 XRD patterns of reaction products of BM-LiH, BM-KH, and BM-(LiH-KH) with NH<sub>3</sub>; XRD pattern of LiH (PDF#78-0838), KH (PDF#65-9244), LiNH<sub>2</sub> (PDF#75-0049), KNH<sub>2</sub> (PDF#74-0188) are referred from databases.

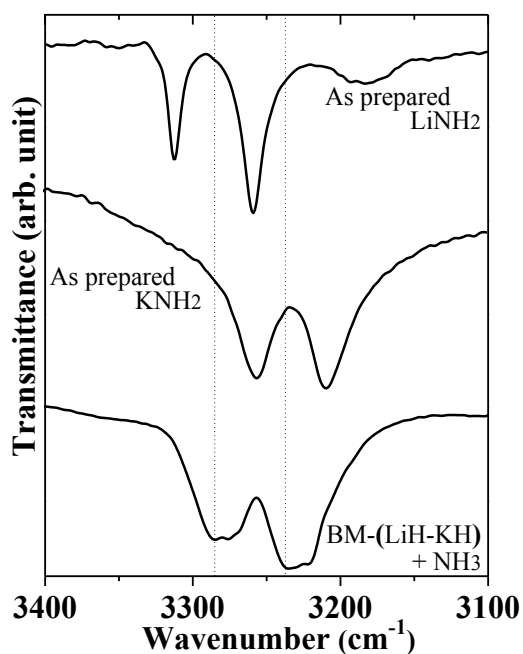


Figure 4-1-5 FT-IR spectra of LiNH<sub>2</sub>, KNH<sub>2</sub>, and reaction product of BM-(LiH-KH) with NH<sub>3</sub>.

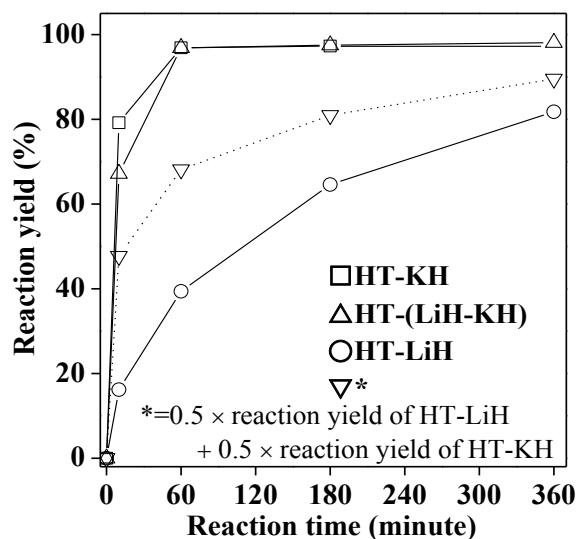


Figure 4-1-6 Hydrogen generation profiles for the reactions of HT-MH with  $\text{NH}_3$ . The broken line is the expected reaction yield of HT-(LiH-KH) without interaction each other (\* =  $0.5 \times$  reaction yield of HT-LiH +  $0.5 \times$  reaction yield of HT-KH)

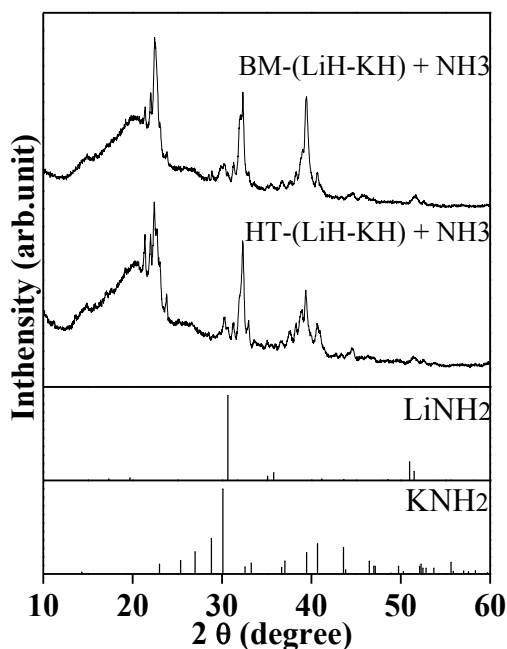


Figure 4-1-7 XRD patterns of reaction products of BM-(LiH-KH) and HT-(LiH-KH) with  $\text{NH}_3$ ; XRD pattern of LiH (PDF#78-0838), KH (PDF#65-9244),  $\text{LiNH}_2$  (PDF#75-0049),  $\text{KNH}_2$  (PDF#74-0188) are referred from databases.

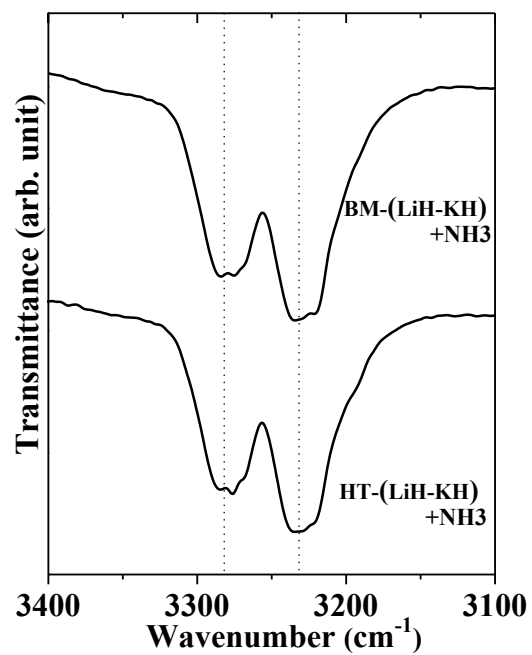


Figure 4-1-8 FT-IR spectra of reaction product of BM-(LiH-KH) and HT-(LiH-KH) with NH<sub>3</sub>.

#### ***4-1-3 Summary***

In this study, the ammonolysis reaction of LiH-KH complex synthesized by ball-milling has been investigated at room temperature. The LiH-KH complex showed high reaction rate at a later stage due to high diffusion rate of  $\text{NH}_3$  into  $\text{LiK}(\text{NH}_2)_2$  as a reaction product. After the heat treatment, the reaction rate of LiH and KH are found to be almost similar, suggesting that the crystalline size and structural disorder are not effective for the reactivity with  $\text{NH}_3$  after the first activation by the ball milling, which would have been mainly originated by removing the stable oxide or hydroxide layer on the *MH* surface[4-1, 4]. On the other hand, the LiH-KH complex showed different and interesting behaviors, in the term of significant improvement of the reactivity by the heat treatment. Namely, the reaction rate in the initial-stage seems to be inhibited due to crystalline disorder of the LiH-KH complex phase induced by the ball-milling process, which is especially noticeable from the XRD results for the LiH-KH complex system shown in Fig. 4-1-1. Furthermore, it is demonstrated that slow reaction rate in the initial-stage of the LiH-KH complex can be improved by restoring the crystalline disorder by thermal crystallization, resulting in high reactivity with  $\text{NH}_3$  similar to the KH system. Therefore, crystalline LiH-KH complex is easily transformed to  $\text{LiK}(\text{NH}_2)_2$ , which is important product to improve the reaction rate due to the high solubility of  $\text{NH}_3$ , although the disordered state requires longer time to form  $\text{LiK}(\text{NH}_2)_2$ . The interaction between complex amide and  $\text{NH}_3$  is found to be similar to that in the case of  $\text{KNH}_2$  because the reaction rates of HT-KH and HT-(LiH-KH) shows no significant difference.

## 4-2 Hydrogenation reaction of $\text{LiK}(\text{NH}_2)_2$

### 4-2-1 Thermal properties of $\text{LiK}(\text{NH}_2)_2$

The new complex amide phase denoted as  $\text{LiK}(\text{NH}_2)_2$  should be characterized to further discuss the reaction properties. Thus, thermal properties of  $\text{LiK}(\text{NH}_2)_2$  prepared by ball-milling from  $\text{LiNH}_2$  and  $\text{KNH}_2$  (=BM-( $\text{LiNH}_2$ - $\text{KNH}_2$ )) and produced by reaction of HT-( $\text{LiH}$ - $\text{KH}$ ) with  $\text{NH}_3$  (=DE-HT-( $\text{LiH}$ - $\text{KH}$ )) were investigated. Fig. 4-2-1 shows X-ray diffraction patterns of BM-( $\text{LiNH}_2$ - $\text{KNH}_2$ ) and DE-HT-( $\text{LiH}$ - $\text{KH}$ ). It is confirmed that BM-( $\text{LiNH}_2$ - $\text{KNH}_2$ ) showed diffraction peaks similar to those of DE-HT-( $\text{LiH}$ - $\text{KH}$ ) except  $\text{LiNH}_2$  and  $\text{KNH}_2$  phases although the observed peaks were weakened and broadened due to the milling effects. Fig. 4-2-2 shows IR spectra of BM-( $\text{LiNH}_2$ - $\text{KNH}_2$ ) and DE-HT-( $\text{LiH}$ - $\text{KH}$ ). The observed two absorption peaks corresponding to the  $-\text{NH}_2$  group of BM-( $\text{LiNH}_2$ - $\text{KNH}_2$ ) are located in the same energy range with that of DE-HT-( $\text{LiH}$ - $\text{KH}$ ). These results indicate that a double-cation amide ( $\text{LiK}(\text{NH}_2)_2$ ) is formed by ball-milling process as well as the ammonolysis reaction of the  $\text{LiH}$ - $\text{KH}$  complex.

Figure 4-2-3 shows DSC profiles of BM-( $\text{LiNH}_2$ - $\text{KNH}_2$ ) and DE-HT-( $\text{LiH}$ - $\text{KH}$ ) under Ar atmosphere. For the both profiles of BM-( $\text{LiNH}_2$ - $\text{KNH}_2$ ) and DE-HT-( $\text{LiH}$ - $\text{KH}$ ), two reversible peaks are observed around 180 °C and 210 °C, respectively, suggesting that the both peaks are originated due to phase transitions. The phase transition at higher temperature must be melting because the well separated powder samples are changed to piece rock type state after the measurements. It is noteworthy that the melting point of  $\text{LiK}(\text{NH}_2)_2$  is lower than that of  $\text{LiNH}_2$  and  $\text{KNH}_2$ .

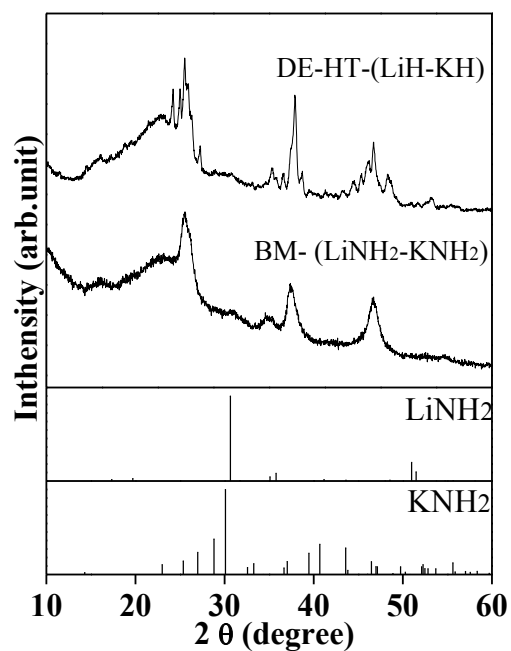


Figure 4-2-1 XRD patterns of BM-(LiNH<sub>2</sub>-KNH<sub>2</sub>) and DE-HT-(LiH-KH); XRD pattern of LiNH<sub>2</sub> (PDF#75-0049), KNH<sub>2</sub> (PDF#74-0188) are referred from databases.

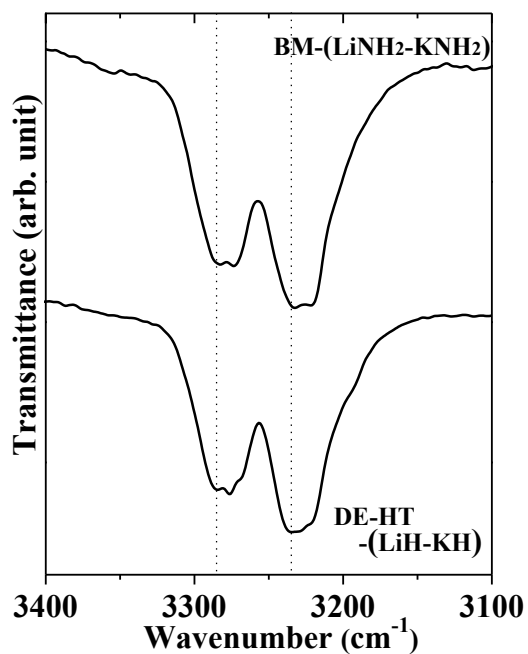


Figure 4-2-2 FT-IR spectra of BM-(LiNH<sub>2</sub>-KNH<sub>2</sub>) and DE-HT-(LiH-KH).

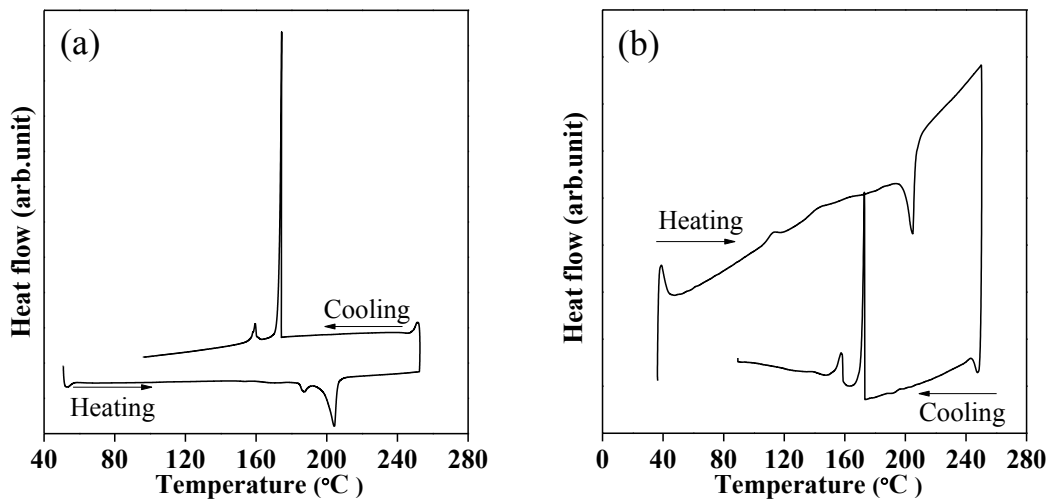


Figure 4-2-3. DSC profile of DE-HT-(LiH-KH) (a) and BM-(LiNH<sub>2</sub>-KNH<sub>2</sub>) (b) under Ar atmosphere by heating up to 250 °C

#### ***4-2-2 Hydrogenation reaction of LiK(NH<sub>2</sub>)<sub>2</sub>***

The investigation for hydrogenation reaction of LiK(NH<sub>2</sub>)<sub>2</sub>, which is the reaction product of the LiH-KH complex with NH<sub>3</sub> (=DE-HT-(LiH-KH)) as described in section 4-1-2, has been performed under H<sub>2</sub> flow condition in an open system by using DSC-MS apparatus. As mentioned in section 4-2-1, it is found that the phase transition of LiK(NH<sub>2</sub>)<sub>2</sub> occurred at around 180 °C and 210 °C. Therefore, the hydrogenation temperature of DE-HT-(LiH-KH) was firstly set to 160 °C to avoid the influence the phase transitions. Fig. 4-2-4 shows the DSC-MS profile of DE-HT-(LiH-KH) under H<sub>2</sub> flow condition during the heating up to 160 °C. In the DSC profile, a decrease of heat flow started below 100 °C, indicating endothermic reaction started at such a low temperature. On the other hand, generation of NH<sub>3</sub> gas is clearly observed to be started from 80 °C and decreased during the isothermal step at 160 °C in the mass spectra, indicating that the expected reaction proceeded. However, the reaction yield for the hydrogenation reaction at 160 °C for 1 h is estimated as 56.3 %, i.e. half amount of LiK(NH<sub>2</sub>)<sub>2</sub> is still remained unreacted. Fig. 4-2-5 shows XRD patterns of the samples before and after the hydrogenation during above mentioned DSC experiment. By the hydrogenation, the peaks of LiK(NH<sub>2</sub>)<sub>2</sub> totally disappeared, and the observed peaks are assigned to KH and LiNH<sub>2</sub>. These results indicated that the LiK(NH<sub>2</sub>)<sub>2</sub> reacted with H<sub>2</sub> to form KH and LiNH<sub>2</sub> below 160 °C, suggesting that the component of KNH<sub>2</sub> in complex amide selectively reacted with H<sub>2</sub> as prior reaction to the LiNH<sub>2</sub> component. In fact, it was reported that the hydrogenation of KNH<sub>2</sub> under H<sub>2</sub> flow condition proceeded even at 50 °C, which is lower than the hydrogenation temperature of LiNH<sub>2</sub>, 200 °C[4-1].

In order to hydrogenate LiK(NH<sub>2</sub>)<sub>2</sub> completely, it is necessary to increase the hydrogenation temperature of DE-HT-(LiH-KH). As a preliminary experiment, DSC

experiment under H<sub>2</sub> atmosphere is performed on the LiNH<sub>2</sub>-KH mixture as obtained from the hydrogenation of LiK(NH<sub>2</sub>)<sub>2</sub> at 160 °C as shown in Fig. 4-2-6. A reversible sharp peak around 240 °C is observed, which could be attributed to the melting. To confirm the melting phenomenon, thermal properties of LiNH<sub>2</sub>-KH complex prepared by ball-milling are investigated, which is described in section 4-2-3. Considering the results, the hydrogenation of the KH and LiNH<sub>2</sub> mixture has been performed at 220 °C, which is lower temperature than that of the phase transition. Fig. 4-2-7 shows the DSC-MS profile of DE-HT-(LiH-KH) under H<sub>2</sub> flow condition during heating up to 220 °C, where the temperature was increased and kept at 160 °C and at 220 °C for 1 h and 4 h, respectively. After the reaction at 160 °C with NH<sub>3</sub> release, the other endothermic peak is observed while heating up to 220 °C. In the mass spectrum, the generation of NH<sub>3</sub> is clearly observed starting from 180 °C and decreased during the isothermal step at 220 °C, indicating that the remaining LiNH<sub>2</sub> reacted with H<sub>2</sub> to form LiH and NH<sub>3</sub>. In fact, from the XRD results of the product shown in Fig. 4-2-8, it is confirmed that the peaks corresponding to LiNH<sub>2</sub> are not observed, and only KH and LiH phases are found. The intensity of LiH peaks is very low, so enlarged figure is shown as the inset to find the peaks of LiH. The total reaction yield obtained by the heating to 220 °C for the regeneration reaction is 95.6 %, which indicated that LiK(NH<sub>2</sub>)<sub>2</sub> is almost hydrogenated at this temperature. Previously, it was reported that the reaction yield for hydrogenation of LiNH<sub>2</sub> itself for 4 h was 4.2 % at 200 °C and 71.0 % at 300 °C[4-1]. In another paper, the reaction yield for hydrogenation of LiNH<sub>2</sub> for 4 h was 24.3 % at 200 °C and 96 % at 300 °C[4-5]. Even though it is difficult to make a comparison between these previous results and the results in this study due to the difference of the reaction conditions such as temperature, H<sub>2</sub> flow rate, and sample scale; it can be stated that the hydrogenation

properties of  $\text{LiK}(\text{NH}_2)_2$  are better than those of the hydrogenation of  $\text{LiNH}_2$  itself and then those of the previous results due to almost complete hydrogenation of DE-HT-(LiH-KH) at 220 °C. From the experimental results, it is clear that the interaction between  $\text{LiNH}_2$  and KH resulted in the decreased melting point to 240°C, which causes a high reactivity of the complex amide containing KH and  $\text{LiNH}_2$ . This is very similar to the observation by Yamamoto et al[4-1], where they claimed drastically fast hydrogenation of  $\text{NaNH}_2$  at 200 °C – very near to the melting point of  $\text{NaNH}_2$  i.e. 210 °C[4-6]. This high reactivity can be explained on the basis of high mobility and active state of atoms near melting point in comparison to that in solid phase. Such a high atomic mobility is very crucial for the hydrogenation of  $\text{LiK}(\text{NH}_2)_2$  in order to release heavy N atoms as  $\text{NH}_3$ .

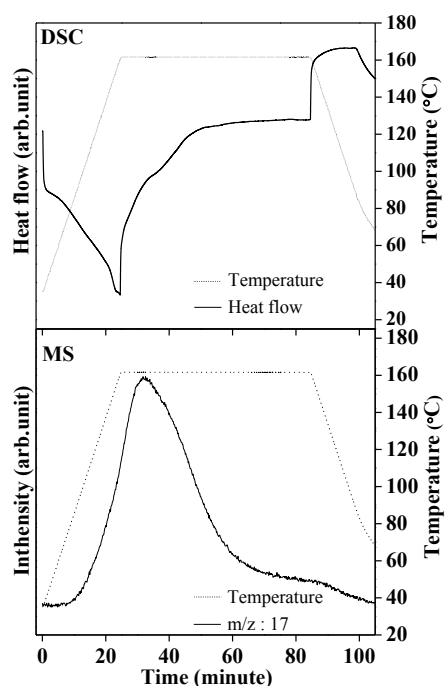


Figure 4-2-4 DSC-MS profile of DE-HT-(LiH-KH) under 0.5 MPa H<sub>2</sub> flow condition at 160 °C for 1 h, where the heating rate is 5 °C/min.

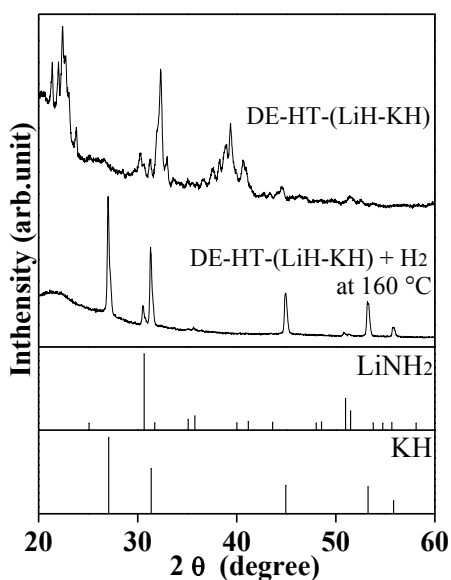


Figure 4-2-5 XRD patterns of DE-HT-(LiH-KH) before and after hydrogenation at 160 °C for 1 h; XRD pattern of LiNH<sub>2</sub> (PDF#75-0049), KH (PDF#65-9244) are referred from databases.

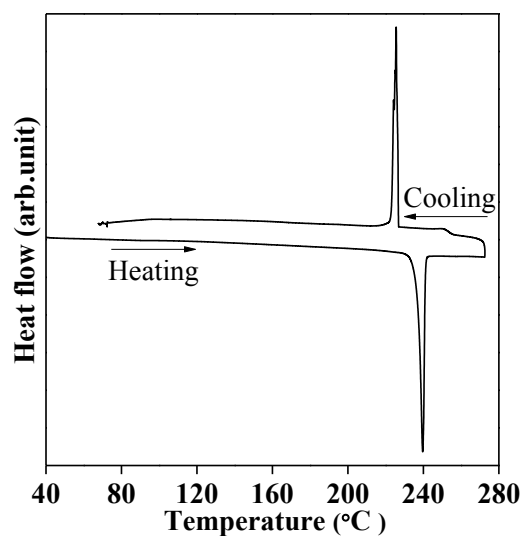


Figure 4-2-6 DSC profile under H<sub>2</sub> atmosphere for the reaction product after hydrogenation at 160 °C for DE-HT-(LiH-KH)

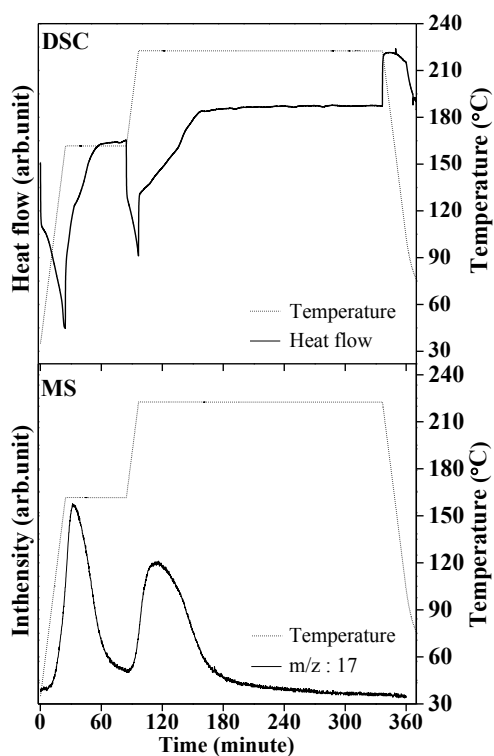


Figure 4-2-7 DSC-MS profile of DE-HT-(LiH-KH) under 0.5 MPa H<sub>2</sub> flow condition at 160 °C for 1h and following 220 °C for 4h, where the heating rate is 5 °C/min

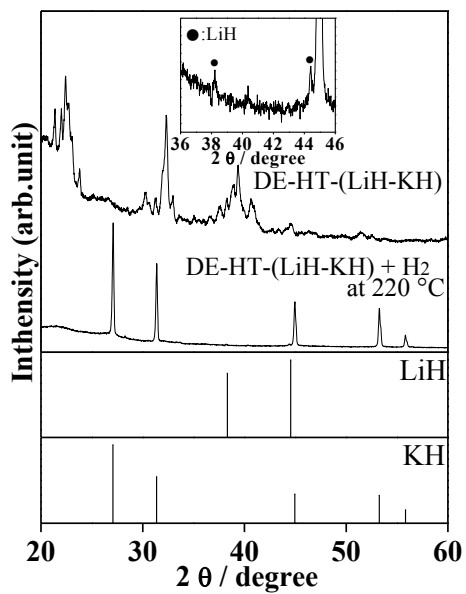


Figure 4-2-8 XRD patterns of DE-HT-(LiH-KH) before and after hydrogenation at 160 °C for 1h and following 220 °C for 4h ; XRD pattern of LiNH<sub>2</sub> (PDF#75-0049) , KH (PDF#65-9244) are referred from databases.

### 4-2-3 Thermal property of $\text{LiNH}_2\text{-KH}$ complex

In the investigation for hydrogenation reaction of  $\text{LiK}(\text{NH}_2)_2$ , a mixture of  $\text{LiNH}_2$  and  $\text{KH}$  was obtained as a first product as described in section 4-2-2. Therefore, thermal properties of  $\text{LiNH}_2\text{-KH}$  complex prepared by ball-milling (=BM-( $\text{LiNH}_2\text{-KH}$ )), which is composed of the same components with the product after hydrogenation of  $\text{LiK}(\text{NH}_2)_2$ , have been investigated to discuss the hydrogenation reaction of  $\text{LiK}(\text{NH}_2)_2$ .

Figure 4-2-9 shows DSC profile of BM-( $\text{LiNH}_2\text{-KH}$ ) under  $\text{H}_2$  atmosphere. Consistently with the DSC measurement of the mixture of  $\text{LiNH}_2$  and  $\text{KH}$  as a reaction product after the hydrogenation of  $\text{LiK}(\text{NH}_2)_2$ , this experiment also shows a reversible sharp peak around  $240\text{ }^\circ\text{C}$ . It is interesting to note here that none of  $\text{LiNH}_2$  and  $\text{KH}$  show any structural phase transition at this temperature and the melting point of  $\text{KH}$  and  $\text{LiNH}_2$  are higher than  $300\text{ }^\circ\text{C}$ [4-1, 7]. Besides, the sample after the DSC measurement is found to be a lump state as shown in Fig. 4-2-10. Furthermore, the XRD results of the sample before and after DSC measurement interestingly showed only  $\text{LiNH}_2$  and  $\text{KH}$  phases without any phase changes as shown in Fig. 4-2-11 although the peak intensity and shape are altered slightly by annealing effect during the DSC measurement. These results indicate that the observed peak in DSC profile is caused by the melting and solidification of the sample, and the phase transition would be originated in eutectic melting phenomenon due to coexistence of  $\text{KH}$  and  $\text{LiNH}_2$ .

The eutectic melting phenomenon of  $M_{\text{I}}(\text{NH}_2)_m\text{-}M_{\text{II}}\text{H}$  complex ( $M_{\text{I}}, M_{\text{II}} = \text{Li, Na, K, Ca, Mg}$  with valence number of cations) would be important as an advantage for the amide-imide hydrogen storage system.

As described in section 1-2-2, the hydrogen generation reaction of the amide-imide systems proceeds in the solid-solid reaction. Therefore, it is considered that there should

be a close relationship between the melting phenomenon of the  $M_I(\text{NH}_2)_m\text{-}M_{II}\text{H}$  composite and its reaction kinetics, however, no information for melting point of the  $M_I(\text{NH}_2)_m\text{-}M_{II}\text{H}$  composite have been reported so far. In this study, eutectic melting phenomenon of the  $\text{LiNH}_2\text{-KH}$  composite under  $\text{H}_2$  atmosphere has been confirmed for the first time. Thus, it is expected that systematic investigation for such a eutectic melting phenomenon of the  $M_I(\text{NH}_2)_m\text{-}M_{II}\text{H}$  composites leads to a breakthrough to develop the amide-imide systems in future.

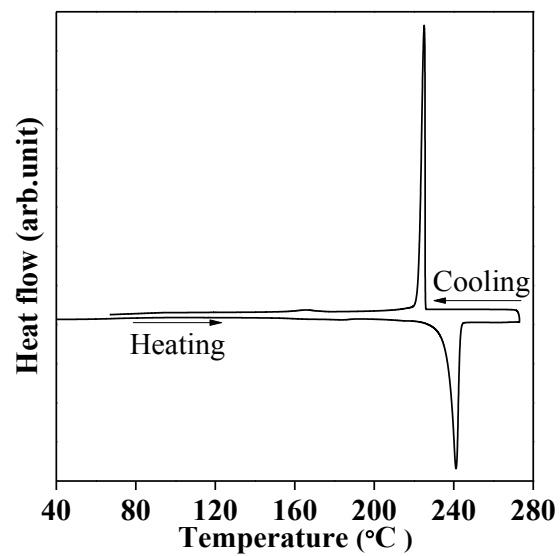


Figure 4-2-9 DSC profile under H<sub>2</sub> atmosphere by heating up to 270 °C for BM-(LiNH<sub>2</sub>-KH).

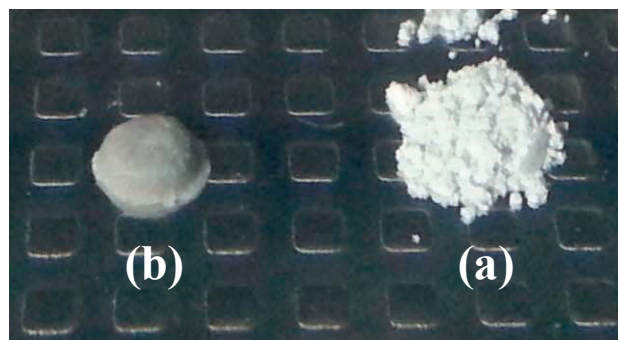


Figure 4-2-10 Appearance of BM-(LiNH<sub>2</sub>-KH) (a) before and (b) after DSC measurement under H<sub>2</sub> atmosphere by heating up to 270 °C.

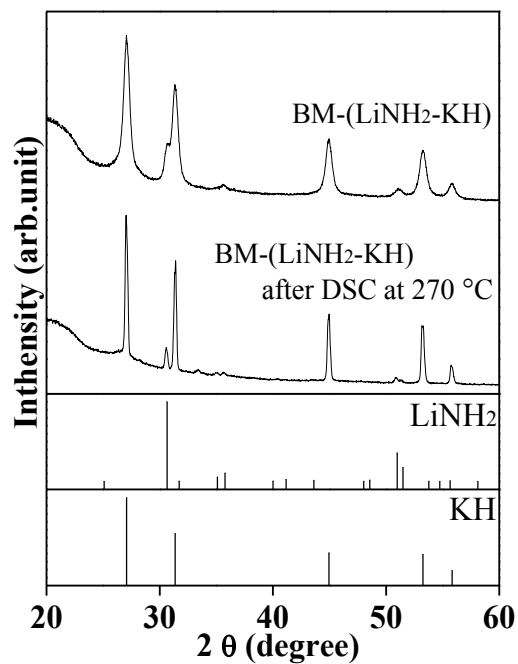


Figure 4-2-11 XRD patterns of BM-(LiNH<sub>2</sub>-KH) before and after DSC measurement under H<sub>2</sub> atmosphere by heating up to 270 °C; XRD pattern of LiNH<sub>2</sub> (PDF#75-0049), KH (PDF#65-9244) are referred from databases.

#### **4-2-4 Hydrogenation reaction of $\text{LiNH}_2$ and $\text{LiK}(\text{NH}_2)_2$ in closed system**

In this section, feasibility of hydrogenation reaction of  $\text{LiNH}_2$  and  $\text{LiK}(\text{NH}_2)_2$  have been further investigated in a closed system by using gas circuit system, which would be more practical condition than that of DSC experiments.

In order to realize the reaction (1-29) in a closed system, a gas circuit system was designed. Fig. 4-2-12 shows the schematic image of the gas circulating system. This apparatus includes a gas densimeter (Yokogawa Electric Corporation, GD400), circulation pump (Nittou kouatsu), gas flow meter and pressure gauge to *in-situ* measure the concentration of  $\text{H}_2$  and  $\text{NH}_3$  up to a maximum of 0.6 MPa pressure and 200 sccm gas flow rate in the circulating system. Additionally,  $\text{NH}_3$  trap by using liquid  $\text{N}_2$  is equipped into the circulating line, thus the generated  $\text{NH}_3$  can be removed from the circulated gases. It is expected that the partial pressure of  $\text{NH}_3$  can be reduced to a sufficient level to realize the progress of the reaction, as the temperature of liquid  $\text{N}_2$  is low enough compared with the freezing point of  $\text{NH}_3$ . Here, the inner volume of the trap part is sufficiently large. Thus, almost all the generated  $\text{NH}_3$  can be trapped even if the experiments are performed by a maximum circulation rate, in other words, the generated  $\text{NH}_3$  cannot be reached to sample part again during the circulation. A reaction cell loading a weighed amount of commercial  $\text{LiNH}_2$  was connected to the gas circuit system and 0.5 MPa  $\text{H}_2$  was introduced. After that, the experiments were carried out under gas circulated condition with 16 and 88 sccm of flow rates at 300 °C.  $\text{NH}_3$  trap using liquid  $\text{N}_2$  was used to reduce the partial pressure of  $\text{NH}_3$  in the circuit system. In order to estimate the reaction yield, the amount of  $\text{NH}_3$  trapped during the reaction was measured by using a gas densimeter after the reaction. The solid materials have been identified by XRD before and after the reaction.

Fig. 4-2-13 shows XRD pattern of LiNH<sub>2</sub> after the hydrogenation for 8 h at 300 °C, where the circulating rate was 16 sccm. Although diffraction peaks corresponding to LiH could be observed, LiNH<sub>2</sub> still remained in the product. In this case, the reaction yield is found to be 35.6 %. These results indicate that the  $P_{\text{NH}_3}$  is reduced enough and the reaction proceeded by using the circulating system. However, the 16 sccm of circuit rate was not enough to reach the same level of  $P_{\text{NH}_3}$  as the DSC condition due to slow diffusion rate of NH<sub>3</sub> gas in the solid sample part, indicating that NH<sub>3</sub> could not be removed enough from the reaction field. Therefore, the reaction condition was changed to higher circulating rate of 88 sccm. Fig. 4-2-14 shows XRD patterns of the product in circulating system for 4 and 6 h at 300 °C. The diffraction peaks corresponding to LiNH<sub>2</sub> observed after the previous experiments have been totally disappeared with 16 sccm rate. Here, Li<sub>2</sub>O phase observed in XRD profile should be derived from the impurity in the reagent. Generally, X-ray diffraction intensity is strongly related to electron number of atoms in the material. If the amount of Li<sub>2</sub>O is considerable in the samples, the diffraction intensity have to be stronger than that of LiH. Thus, it is considered that the amount of the impurity is small by taking account of the intensity of LiH and Li<sub>2</sub>O phases, suggesting that any effects of the impurity into the essential reaction could be negligible. The reaction yields for 4 and 6 h were estimated from NH<sub>3</sub> concentration by using the gas densimeter, and the values were respectively 75.3 % and 91.6 %. As described above, it is important to decrease the partial pressure of NH<sub>3</sub> by removing NH<sub>3</sub> gas effectively from the reaction field (1-29). In this experiment, the gas in the closed system was circulated and NH<sub>3</sub> was simultaneously trapped. As the results, sufficiently low  $P_{\text{NH}_3}$  and highly efficient condition for NH<sub>3</sub> production could be realized using faster circulating rate.

From the above experiments, the feasibility of hydrogenation of LiNH<sub>2</sub> under H<sub>2</sub> circuit

condition in the closed system has been demonstrated. Then, the hydrogenation process of  $\text{LiK}(\text{NH}_2)_2$  in closed system has also been investigated by using the gas circuit system to demonstrate its feasibility and understand the hydrogenation process in more detail by following procedure. A reaction cell loading a weighed amount of BM- $(\text{LiNH}_2\text{-KNH}_2)$  was connected to the gas circuit system and 0.5 MPa  $\text{H}_2$  was introduced. After that, the experiment was carried out under gas circulated condition with 100 sccm of flow rate at 160 °C and 220 °C. The solid materials have been identified by XRD and IR before and after the reaction.

Fig. 4-2-15 and Fig. 4-2-16 show XRD patterns and IR spectra of the product in circulating system for each reaction time at 160 °C and 220 °C, respectively. For the product after the hydrogenation reaction for 1 h at 160 °C, diffraction pattern corresponding to KH phase is clearly observed, indicating that hydrogenation reaction proceeds in the condition. However, diffraction patterns corresponding to remaining  $\text{LiK}(\text{NH}_2)_2$  and  $\text{Li}_3\text{K}(\text{NH}_2)_4$  are also observed, suggesting that  $\text{LiK}(\text{NH}_2)_2$  is hydrogenated in the initial stage to form  $\text{Li}_3\text{K}(\text{NH}_2)_4$  and KH as the first hydrogenation products. In fact, in the IR spectrum of the hydrogenation product, the absorption peak at 3290 ~ 3300  $\text{cm}^{-1}$  corresponding to  $\text{Li}_3\text{K}(\text{NH}_2)_4$  reported before is observed as shoulder structure. Thus, the product has been employed for further hydrogenation at the same condition. For the product after the hydrogenation reaction for totally 3h at 160 °C, diffraction pattern corresponding to  $\text{LiK}(\text{NH}_2)_2$  phase is almost disappeared and mainly KH and  $\text{Li}_3\text{K}(\text{NH}_2)_4$  phases are observed. In addition, in the IR spectrum of the hydrogenation product, mainly absorption peaks corresponding to  $\text{Li}_3\text{K}(\text{NH}_2)_2$  and a small absorption peaks corresponding to  $\text{LiNH}_2$  are observed, indicating that  $\text{Li}_3\text{K}(\text{NH}_2)_4$  can react with  $\text{H}_2$  to form KH and  $\text{LiNH}_2$  at 160 °C. Then, from the following results of XRD pattern and IR

spectra of the hydrogenation products for totally 6, 10, and 14 h, it is confirmed that all of  $\text{Li}_3\text{K}(\text{NH}_2)$  could be hydrogenated to form  $\text{LiNH}_2$  and  $\text{KH}$  at  $160\text{ }^\circ\text{C}$ , which is consistent with the result in DSC-MS for hydrogenation of  $\text{LiK}(\text{NH}_2)_2$  as described in section 4-2-2. Finally, it is confirmed by XRD and IR that the mixture of  $\text{LiNH}_2$  and  $\text{KH}$  has been hydrogenated totally to form  $\text{LiH}$  at  $220\text{ }^\circ\text{C}$  for 10 h. Thus, it has been demonstrated that  $\text{LiK}(\text{NH}_2)_2$  could be hydrogenated to regenerate  $\text{LiH-KH}$  complex and  $\text{NH}_3$  below  $250\text{ }^\circ\text{C}$  even in the closed circuit system.

#### ***4-2-5 Summary***

In this study, hydrogenation reaction of  $\text{LiK}(\text{NH}_2)_2$  prepared by ball-milling from  $\text{LiNH}_2$  and  $\text{KNH}_2$ , and produced by ammonolysis of the  $\text{LiH-KH}$  complex have been investigated in the open system by DSC-MS and in the closed system by a gas circuit apparatus. As a result, it has been confirmed that the hydrogenation process of  $\text{LiK}(\text{NH}_2)_2$  proceeds through several steps. At  $160\text{ }^\circ\text{C}$ ,  $\text{LiK}(\text{NH}_2)_2$  reacts with  $\text{H}_2$  to form  $\text{Li}_3\text{K}(\text{NH}_2)_2$  and  $\text{KH}$  as the first product, and then the  $\text{Li}_3\text{K}(\text{NH}_2)_2$  is hydrogenated at the same temperature to form  $\text{LiNH}_2$  and  $\text{KH}$ . Finally, the remaining  $\text{LiNH}_2$  is hydrogenated at  $220\text{ }^\circ\text{C}$ . It is noteworthy that the interaction between  $\text{LiNH}_2$  and  $\text{KH}$  realizes high reactivity for the hydrogenation process at the lower temperature. Furthermore, it has also been demonstrated that this hydrogenation process of  $\text{LiK}(\text{NH}_2)_2$  can proceed even in the closed circuit system.

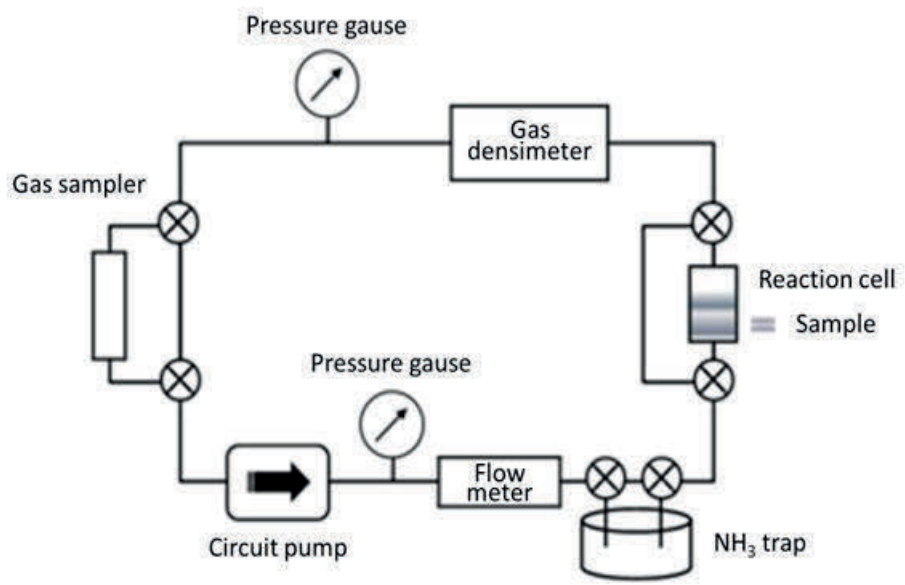


Figure 4-2-12 Schematic view of gas circuit system.

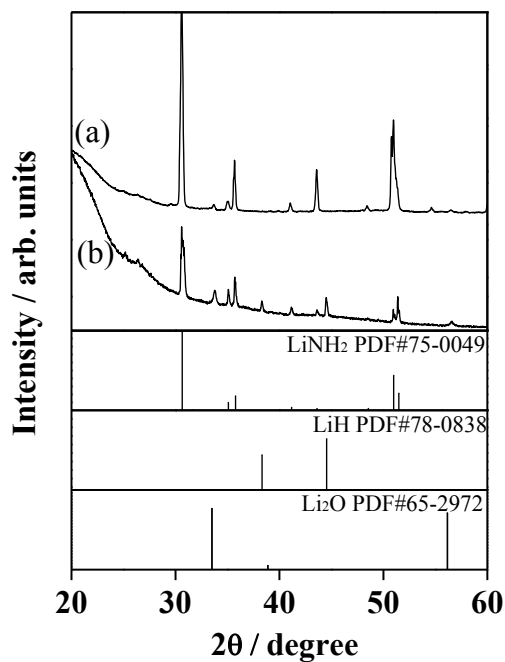


Figure 4-2-13 XRD patterns of LiNH<sub>2</sub> (a) before and (b) after the treatment under 16 sccm H<sub>2</sub> flow condition for 8 h at 300 °C. XRD pattern of LiNH<sub>2</sub> (PDF#75-0049), LiH (PDF#78-0838), and Li<sub>2</sub>O (PDF#65-2972) are referred from databases.

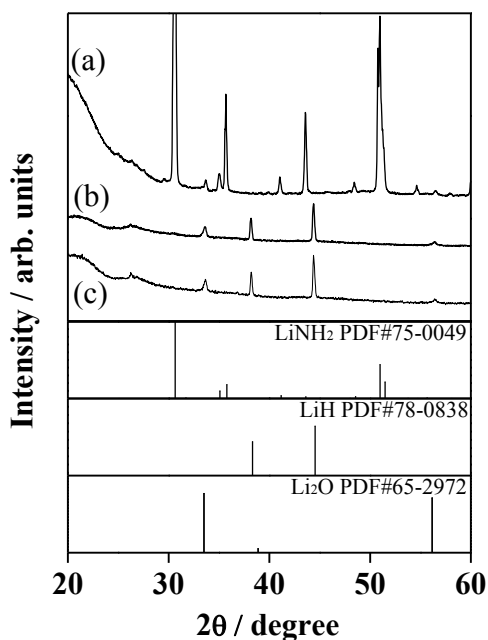


Figure 4-2-14 XRD patterns of LiNH<sub>2</sub> (a) before, (b) after the treatment under 88 sccm H<sub>2</sub> flow condition for 4 h, and (c) 6 h at 300 °C. XRD pattern of LiNH<sub>2</sub> (PDF#75-0049), LiH (PDF#78-0838), and Li<sub>2</sub>O (PDF#65-2972) are referred from databases.

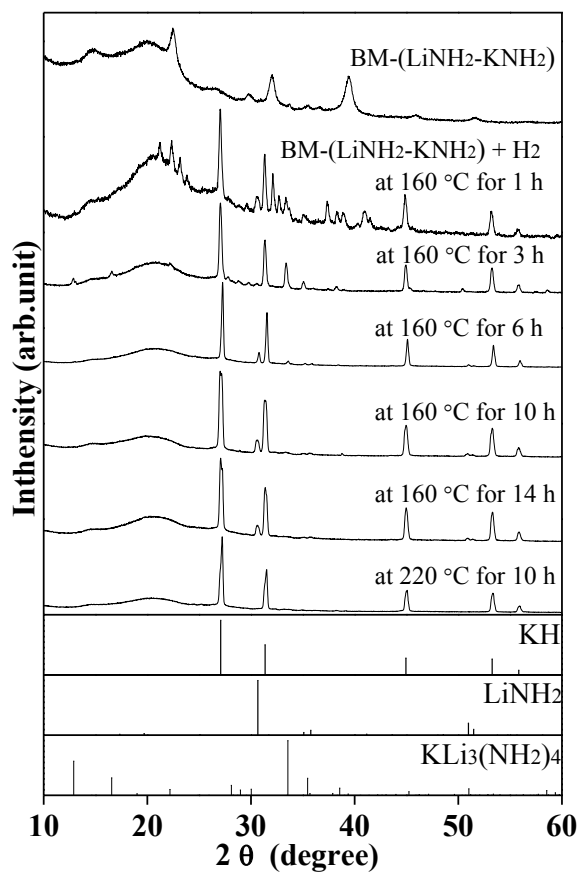


Figure 4-2-15 XRD patterns of BM-(LiNH<sub>2</sub>-KNH<sub>2</sub>) before and after the treatment under 100 sccm H<sub>2</sub> flow condition at 160 °C for 1-14 h and at 220 °C for 10 h. XRD pattern of LiNH<sub>2</sub> (PDF#75-0049), KH (PDF#65-9244), and KLi<sub>3</sub>(NH<sub>2</sub>)<sub>4</sub> (PDF# 75-2490) are referred from databases.

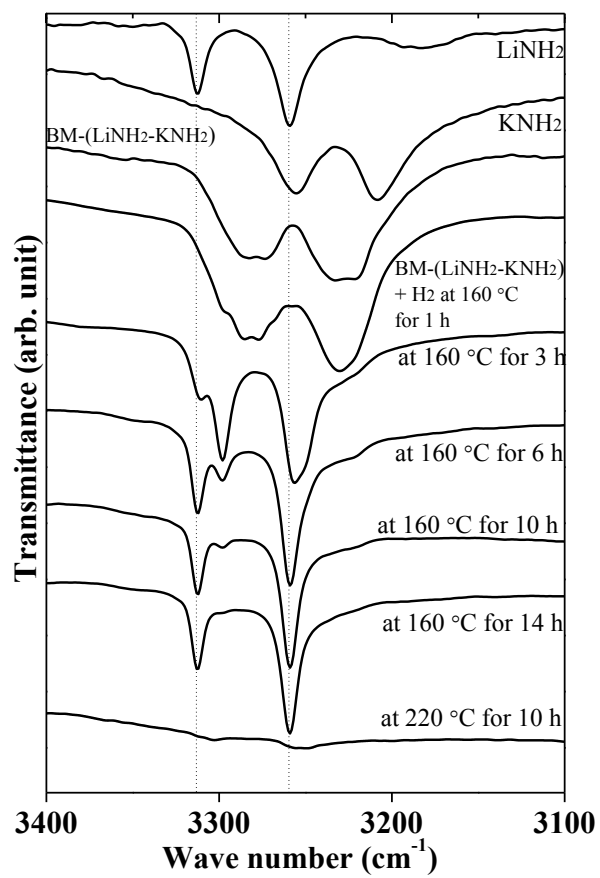


Figure 4-2-16 XRD patterns of BM-(LiNH<sub>2</sub>-KNH<sub>2</sub>) before and after the treatment under 100 sccm H<sub>2</sub> flow condition at 160 °C for 1-14 h and at 220°C for 10 h.

### 4-3 Ammonia synthesis from Lithium nitride

#### 4-3-1 Hydrogenation reaction of $\text{Li}_3\text{N}$

$\text{NH}_3$  production by hydrogenation of  $\text{Li}_3\text{N}$  has been investigated by DSC-MS under  $\text{H}_2$  flow condition in an open system. In order to realize the reaction progress at lower temperature, it is essential to decrease the value of the last entropy term in equation (1-30:  $\Delta G = \Delta H_a - T\Delta S^0 - TR \ln(P_{\text{H}_2}/P_{\text{NH}_3})$ ). In the DSC-MS experiments, the reaction has been investigated under the  $\text{H}_2$  flow condition in the open system, suggesting that the value of the entropy is increased by reducing the partial pressure of  $\text{NH}_3$ ,  $P_{\text{NH}_3}$ . Fig. 4-3-1 shows the DSC-MS profile of  $\text{Li}_3\text{N}$  under 0.5 MPa of the  $\text{H}_2$  flow condition. As shown in this DSC profile, exothermic peak is observed from 200 °C during heating, which should be originated due to the hydrogenation of  $\text{Li}_3\text{N}$  described by the reaction (1-1:  $\text{Li}_3\text{N} + 2\text{H}_2 \rightarrow 2\text{LiH} + \text{LiNH}_2$ ). The temperature for this reaction is consistent with the results reported before[4-8]. It is also possible that the hydrogenation of  $\text{LiNH}_2$  by the reaction (1-29:  $\text{LiNH}_2 + \text{H}_2 \rightarrow \text{LiH} + \text{NH}_3$ ) could have proceeded at 200 °C in this condition[4-1]. However, it is difficult to distinguish the reaction temperature because the smaller endothermic peak due to the hydrogenation of  $\text{LiNH}_2$  may be overlapped by the larger exothermic peak due to the hydrogenation of  $\text{Li}_3\text{N}$ . In the mass spectrum, the generation of  $\text{NH}_3$  gas is clearly observed above 230 °C. It is expected that the  $\text{NH}_3$  generation originated in hydrogenation of  $\text{LiNH}_2$ . The onset temperature for  $\text{NH}_3$  desorption is about 230 °C, which is very close to that reported so far[4-1]. The  $\text{NH}_3$  desorption intensity is found to be increased with temperature increase, indicating that the hydrogenation of  $\text{LiNH}_2$  gradually proceeds, starting at 230 °C after the  $\text{LiNH}_2$  formation by the hydrogenation of  $\text{Li}_3\text{N}$  around 200 °C. Here, the MS signal of our experimental system is slightly delayed by the DSC signal due to a long distance between the reaction place and

the gas sampling place, and the reaction kinetics of the light elements based materials is generally slow. From the above facts, it is difficult to estimate the accurate reaction temperature of the hydrogenation of  $\text{LiNH}_2$ . Fig. 4-3-2 shows XRD pattern of the product after the DSC-MS measurement. The X-ray diffraction pattern of the reaction product suggests the existence of  $\text{LiH}$  only without any traces of  $\text{Li}_3\text{N}$  and  $\text{LiNH}_2$ . This indicates that  $\text{LiNH}_2$  generated by the prior hydrogenation of  $\text{Li}_3\text{N}$  gradually reacted with  $\text{H}_2$  to form  $\text{NH}_3$  and  $\text{LiH}$ . Here, in these experiments, a small amount of  $\text{Li}_2\text{O}$  derived from impurity in the reagent is also observed by XRD, however such a small amount cannot influence the essential reaction pathway due to the same reason as discussed in section 4-2-4.

From the above results, it is confirmed that the objective two-step process for  $\text{NH}_3$  production proceeded at relatively lower temperature and pressure in the  $\text{H}_2$  flow condition. In thermodynamic analyses based on the experimental results and equation (1-30), the partial pressure of  $\text{NH}_3$  is reduced to be 4 ~ 12 Pa as an overestimation under the experimental conditions, where the  $\Delta H$  and  $\Delta S^0$  are calculated by combining reported  $\Delta^f H^0$  and  $S^0$  values as shown in Table 4-3-1,  $-90.5 \text{ kJ mol}^{-1}$  and  $20.0 \text{ J mol}^{-1} \text{ K}^{-1}$  for  $\text{LiH}$ ,  $-45.9 \text{ kJ mol}^{-1}$  and  $192.8 \text{ J mol}^{-1} \text{ K}^{-1}$  for  $\text{NH}_3$ ,  $130.7 \text{ J mol}^{-1} \text{ K}^{-1}$  for  $\text{H}_2$ ,  $-179.5 \text{ kJ mol}^{-1}$  for  $\text{LiNH}_2$ [4-9-11], and approximate  $S^0$  values of  $\text{LiNH}_2$ , 80-90  $\text{J mol}^{-1} \text{ K}^{-1}$ , which is chosen as similar value to the  $S^0$  value of complex hydrides such as  $\text{LiBH}_4$  and  $\text{LiAlH}_4$  as an assumption[4-12].

Table 4-3-1 Standard enthalpy of formation and standard entropy for H<sub>2</sub>, NH<sub>3</sub>, LiH, and LiNH<sub>2</sub>

Compounds	Enthalpy of formation $\Delta_f H^\circ$ (kJ·mol <sup>-1</sup> )	Entropy $S^\circ$ (J·K <sup>-1</sup> ·mol <sup>-1</sup> )
LiH (s)	-90.5	20
LiNH <sub>2</sub> (s)	-179.5	80 - 90*
H <sub>2</sub> (g)	0	130.7
NH <sub>3</sub> (g)	-45.9	192.8

\*Assumed  $S^\circ$  value for LiNH<sub>2</sub>

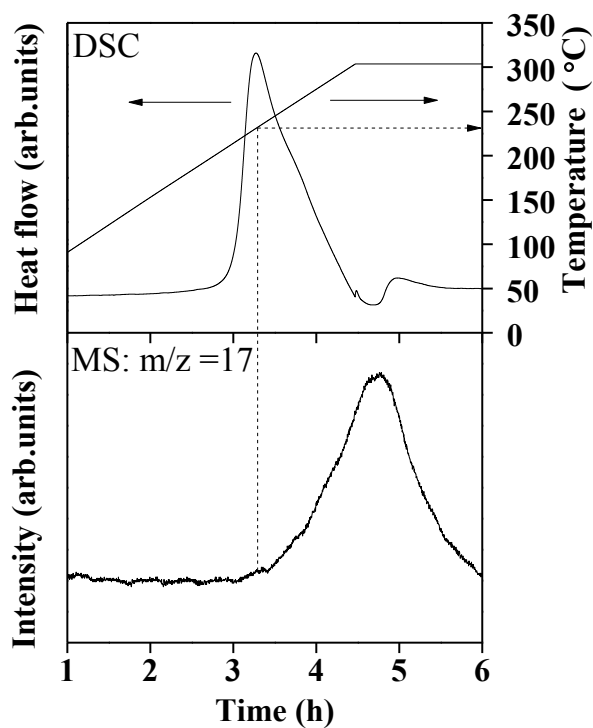


Figure 4-3-1 DSC - MS profiles of Li<sub>3</sub>N under 0.5 MPa of H<sub>2</sub> flow condition at 1.0 °C min<sup>-1</sup> heating rate. NH<sub>3</sub> generation temperature is indicated with the auxiliary line (- - -).

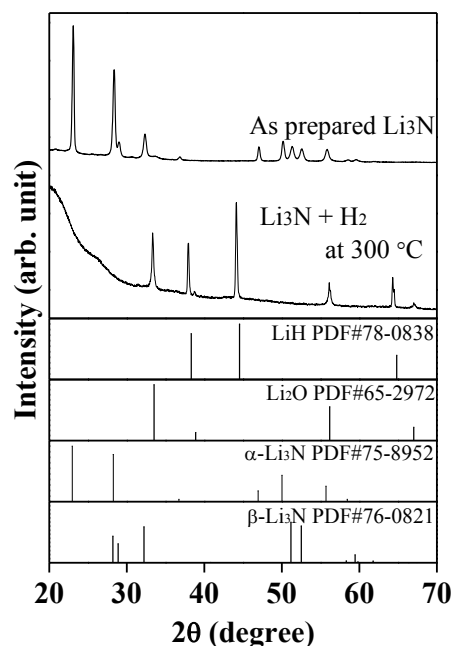


Figure 4-3-2 XRD patterns of  $\text{Li}_3\text{N}$  (a) before and (b) after the treatment under  $\text{H}_2$  flow condition for 4 h at 300 °C. XRD pattern of  $\text{LiH}$  (PDF#78-0838),  $\text{Li}_2\text{O}$  (PDF#65-2972),  $\alpha\text{-Li}_3\text{N}$  (PDF#75-8952), and  $\beta\text{-Li}_3\text{N}$  (PDF#76-0821) are referred from databases.

#### 4-3-2 $\text{ND}_3$ synthesis

The scale up test of the two step reaction ( $1\text{-}24\text{:Li}_3\text{N} + 3\text{H}_2 \rightarrow 2\text{LiH} + \text{LiNH}_2 + \text{H}_2 \rightarrow 3\text{LiH} + \text{NH}_3$ ) has been performed for the  $\text{ND}_3$  synthesis. As described in section 4-2-4, the diffusion rate of generated  $\text{NH}_3$  from reaction field is important for efficient  $\text{NH}_3$  production from  $\text{LiNH}_2$ . Therefore, it is necessary to make the higher  $\text{H}_2$  flow rate for larger scale  $\text{NH}_3$  production. Fig. 4-3-3 shows the schematic image of the  $\text{D}_2$  flow system designed and assembled for the experiment. This system is composed of reaction cell, two hydrogen storage tanks, heaters, pressure gauge, flow meter, and  $\text{NH}_3$  trap. The couple of tanks loaded by the same hydrogen storage alloy are connected to both ends of reaction cell and thermally controlled. When the temperatures of the tanks are kept at high and low temperatures, the pressure gradient is generated due to different  $\text{D}_2$  equilibrium

pressure of the hydrogen storage alloys. By this pressure difference, it is expected that the sufficient D<sub>2</sub> flow condition through reaction cell is realized. In this process, the unreacted D<sub>2</sub> is collected into the alloys kept at lower temperature, and the D<sub>2</sub> can be reused by exchanging the flow direction with temperature control of tanks. As a result, the D<sub>2</sub> loss except the ND<sub>3</sub> generation reaction is suppressed, which is an advantage point as productive NH<sub>3</sub> synthesis. The pressure and flow rate of inside gas are monitored, and the generated NH<sub>3</sub> is collected in the trap. It is clarified that flow rate prepared by this reaction system is 1.0 L/min, which is approximately ten times faster than that required in the above circulating system to complete the reaction. In this study, mixture of LiD and LiND<sub>2</sub> as a product by the reaction of Li<sub>3</sub>N with D<sub>2</sub> expressed by chemical equation (1-1;  $\text{Li}_3\text{N} + 2\text{D}_2 \rightarrow 2\text{LiD} + \text{LiND}_2$ ) was used as a starting material. By using this reaction system, 1.0 g ND<sub>3</sub> was successfully produced by heating the mixture of LiD and LiND<sub>2</sub> in 1.0 MPa of D<sub>2</sub> flow condition with 1.0 L/min of flow rate at 300 °C for 4 h, resulting in 0.25 g/h of production rate. Whereas Haber-Bosch process needs high temperature of 400-600 °C and high pressure of 20-40 MPa, the result in this study indicates that the NH<sub>3</sub> production by the reaction (1-24:  $\text{Li}_3\text{N} + 3\text{D}_2 \rightarrow 2\text{LiD} + \text{LiND}_2 + \text{D}_2 \rightarrow 3\text{LiD} + \text{ND}_3$ ) can be operated under comparatively mild condition and is remarkably useful as efficient NH<sub>3</sub> or ND<sub>3</sub> synthesis method at laboratory-scale.

#### ***4-3-3 Summary***

In this work, NH<sub>3</sub> production by the hydrogenation of Li<sub>3</sub>N and LiNH<sub>2</sub> have been investigated to propose a novel NH<sub>3</sub> synthesis method in laboratory-scale. As a result, the NH<sub>3</sub> generation from Li<sub>3</sub>N in 0.5 MPa of H<sub>2</sub> flow condition below 300 °C was confirmed by DSC-MS and XRD, indicating that the NH<sub>3</sub> production from Li<sub>3</sub>N can proceed in

milder condition than conventional method by using the two step reactions. Furthermore,  $\text{NH}_3$  synthesis test on a larger scale was conducted, where the higher  $\text{D}_2$  flow system by pressure gradient between couple of hydrogen storage alloy tanks was designed for the experiment. By using the system, the  $\text{ND}_3$  production with realistic reaction rate (0.25 g/h) has been demonstrated in 1.0 L/min of  $\text{D}_2$  flow condition below  $300^\circ\text{C}$  and 1.0 MPa.

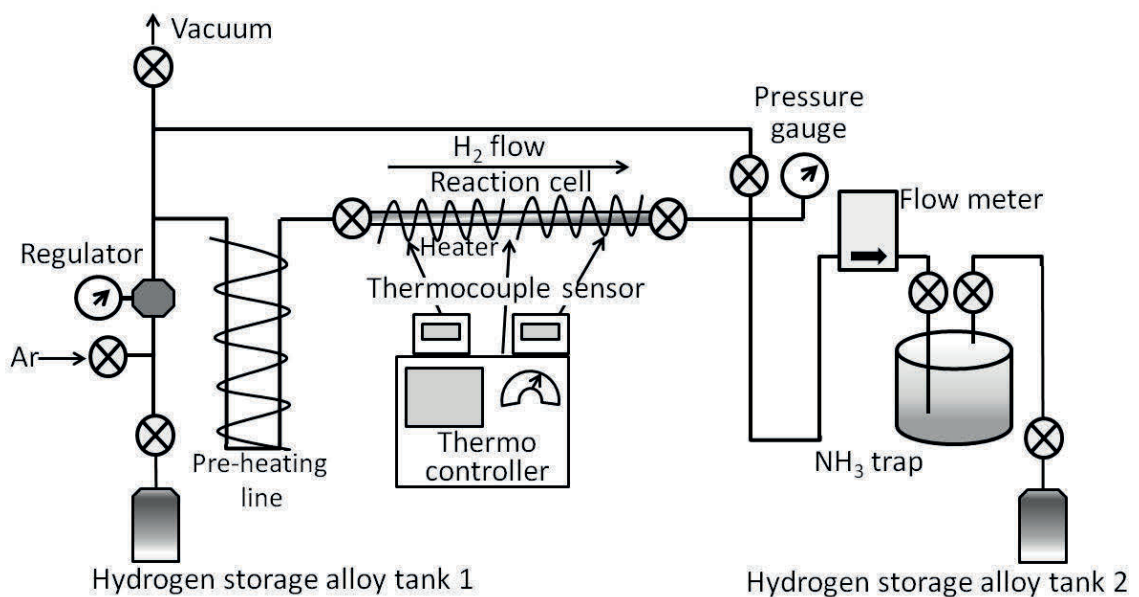


Figure 4-3-3 Schematic view of  $\text{H}_2$  flow system for  $\text{NH}_3$  synthesis.

## References

- [4-1] H. Yamamoto, H. Miyaoka, S. Hino, H. Nakanishi, T. Ichikawa, Y. Kojima, *International Journal of Hydrogen Energy*, **34 (24)** (2009) 9760-9764.
- [4-2] F. Kraus, N. Korber, *Journal of Solid State Chemistry*, **178 (4)** (2005) 1241-1246.
- [4-3] H. Jacobs, B. Harbrecht, *Z. Anorg. Allg. Chem.*, **518 (11)** (1984) 87-100.
- [4-4] Y. Kojima, K. Tange, S. Hino, S. Isobe, M. Tsubota, K. Nakamura, M. Nakatake, H. Miyaoka, H. Yamamoto, T. Ichikawa, *J. Mater. Res.*, **24 (7)** (2009) 2185-2190.
- [4-5] B.X. Dong, Y.L. Teng, J. Ge, L. Song, S.Y. Zhang, *Rsc Advances*, **3 (38)** (2013) 16977-16980.
- [4-6] C. Wu, Y. Bai, J.H. Yang, F. Wu, F. Long, *International Journal of Hydrogen Energy*, **37 (1)** (2012) 889-893.
- [4-7] T. Izuhara, H.T. Takeshita, H. Miyake, *J. Jpn. Inst. Met.*, **75 (2)** (2011) 115-121.
- [4-8] P. Chen, Z.T. Xiong, J.Z. Luo, J.Y. Lin, K.L. Tan, *Nature*, **420 (6913)** (2002) 302-304.
- [4-9] D. Lide, R. , *CRC Handbook of Chemistry and Physics, 89th ed.*(CRC, Boca Raton, FL, 2008).
- [4-10] M. Chase, W., *J. Phys. Chem. Ref. Data Monogr.*, **9** (1998) 1224-1293.
- [4-11] S. Hino, N. Ogita, M. Udagawa, T. Ichikawa, Y. Kojima, *Journal of Applied Physics*, **105 (2)** (2009) 1-3.
- [4-12] NIST, National Institute of Standards and Technology., <http://www.nist.gov/>.

## 5 Conclusion

In this thesis, the LiH-KH complex-NH<sub>3</sub> system and its regeneration reaction were investigated to modify the slow reaction rate of the Li system. In addition, the hydrogenation reaction of LiNH<sub>2</sub> and LiK(NH<sub>2</sub>)<sub>2</sub> in a closed system was investigated under more practical condition by using a gas circuit apparatus. Finally, ND<sub>3</sub> synthesis at laboratory scale from Li<sub>3</sub>N was performed by D<sub>2</sub> flow system using hydrogen storage alloy tanks. The results obtained in these studies are summarized as follows.

1. Hydrogen generation reaction of the LiH-KH complex with NH<sub>3</sub> (ammonolysis) was discussed in section 4-1. For the investigation of the ammonolysis reaction at room temperature, it was clarified that reaction of the LiH-KH complex prepared by ball-milling with NH<sub>3</sub> showed much higher reaction rate in the late-stage than that expected from the reaction rate of LiH and KH with NH<sub>3</sub>. After the reaction, unknown phase was formed as a reaction product. By characterizing the product by XRD measurement and IR spectroscopy, the formation of novel amide phase LiK(NH<sub>2</sub>)<sub>2</sub> was indicated. The enhancement of the reaction rate must be caused by forming the LiK(NH<sub>2</sub>)<sub>2</sub> phase, which possess better kinetic properties on the reaction with NH<sub>3</sub> such as high solubility and/or diffusivity of NH<sub>3</sub> into the LiK(NH<sub>2</sub>)<sub>2</sub> phase. Furthermore, the LiH-KH complex with high crystallinity revealed higher reaction rate from the initial time range than the ball-milled one, and then the reaction yield reached almost 100% after only 1 h. Thus, the disordered state slowed the formation of LiK(NH<sub>2</sub>)<sub>2</sub>, leading to low reaction rate at initial-stage in the case of ball-milled MH complex. The gravimetric hydrogen generation capacity for the LiH-KH complex - NH<sub>3</sub> system was estimated to be 4.87 mass % from the composition, and the utilizable capacity was 4.72 mass %, which was

obtained by the reaction yield for 1h in this study, 96.9 %. This value is higher than that of the KH system, 3.39 mass %, and LiH system, 3.19 mass %, estimated by using the experimental reaction yield for 1 h. From the above results, it is concluded that the LiH-KH complex - NH<sub>3</sub> system reversibly generates and absorbs hydrogen with high capacity and reactivity, which are realized by synergetic effect of the advantageous properties of LiH (high capacity) and KH (high reactivity).

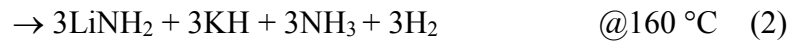
2. Hydrogenation reaction of LiK(NH<sub>2</sub>)<sub>2</sub> (=Regeneration reaction of LiH-KH complex) was investigated and the properties were discussed in section 4-2. The hydrogenation reaction of LiK(NH<sub>2</sub>)<sub>2</sub> was performed in an open system by DSC-MS and in a closed system by gas circuit system. Furthermore, thermal properties of LiK(NH<sub>2</sub>)<sub>2</sub> and LiNH<sub>2</sub>-KH complex were investigated by DSC. It was clarified that the both of LiK(NH<sub>2</sub>)<sub>2</sub> and LiNH<sub>2</sub>-KH complex melt at much lower temperature than those of each individual components, which could promote its atomic diffusion rate, resulting in the higher reactivity. For the hydrogenation reaction of LiK(NH<sub>2</sub>)<sub>2</sub> by DSC-MS, LiK(NH<sub>2</sub>)<sub>2</sub> was hydrogenated at 160 °C, which is lower temperature than that of its melting, and then the product could be identified to be a mixture of LiNH<sub>2</sub> and KH by XRD. To complete the hydrogenation reaction, the mixture of LiNH<sub>2</sub> and KH was hydrogenated subsequently at 220 °C, which is slightly below its melting point. As a result, the hydrogenation of LiNH<sub>2</sub> with KH was almost completed to form LiH at this temperature. The temperature and reaction yield is clearly lower and higher than those of only LiNH<sub>2</sub> in previous reports. This improvement of hydrogenation property is originated by the eutectic phenomenon between LiNH<sub>2</sub> and KH. Herein, it was confirmed that the regeneration proceeded by two steps. In the first step below 160 °C,

the regeneration of the component  $\text{KNH}_2$  occurred to form  $\text{KH}$  and  $\text{NH}_3$ . After that, the remaining  $\text{LiNH}_2$  was hydrogenated to form  $\text{LiH}$  and  $\text{NH}_3$  at  $220\text{ }^\circ\text{C}$ . In this case, the higher reactivity was realized by the interaction between  $\text{KH}$  and  $\text{LiNH}_2$ . Therefore, the  $\text{LiH-KH}$  complex- $\text{NH}_3$  system is recognized as one of promising systems to realize a reversible conversion technique between  $\text{NH}_3$  and  $\text{H}_2$  under moderate condition.

3. Hydrogenation reaction of  $\text{LiNH}_2$  and  $\text{LiK}(\text{NH}_2)_2$  in a closed system by using a gas circuit apparatus were performed as more practical condition and the obtained results were discussed in section 4-2-4. For the experiment, the gas circuit system has been newly designed, which can circulate mixture gas of  $\text{NH}_3\text{-H}_2$  at maximum 0.6 MPa pressure and 200 sccm circulating rate with trapping the generated  $\text{NH}_3$  gas in the closed system. Although hydrogenation reaction of  $\text{LiNH}_2$  proceeded below  $300\text{ }^\circ\text{C}$  even in a closed system, the reaction yield for 8 h was only 35.6 %. This result must be due to deficient diffusivity of generated  $\text{NH}_3$  gas from the reaction field, when the circulating rate was low. Thus, the hydrogenation reaction with higher circulation rate was performed. As a result, the higher reaction rate, 91.6% for 6h at  $300\text{ }^\circ\text{C}$ , was realized.

Furthermore, the hydrogenation reaction of  $\text{LiK}(\text{NH}_2)_2$  was investigated in further detail by using the closed system. The products after the hydrogenation reaction for various reaction time were identified by XRD and IR. It was confirmed that  $\text{Li}_3\text{K}(\text{NH}_2)_4$  and  $\text{KH}$  were generated as the products at  $160\text{ }^\circ\text{C}$  by reaction (1), which was further hydrogenated at the same temperature to form mixture of  $\text{LiNH}_2$  and  $\text{KH}$  by reaction (2). Thus,  $\text{Li}_3\text{K}(\text{NH}_2)_4$  was identified as an intermediate phase in the hydrogenation. Finally, remaining  $\text{LiNH}_2$  in the mixture with  $\text{KH}$  was totally hydrogenated at  $220\text{ }^\circ\text{C}$  to form  $\text{LiH}$  by reaction (3). Thus, it was demonstrated that the hydrogenation reaction of

LiK(NH<sub>2</sub>)<sub>2</sub> can proceed by several steps even in closed circuit system under 220 °C.



4. NH<sub>3</sub> production by the hydrogenation of Li<sub>3</sub>N was investigated and the properties were discussed in section 4-3 to propose a novel NH<sub>3</sub> synthesis method applying “amid-imide hydrogen storage system” and “metal hydride-ammonia system” at laboratory-scale. As a preliminary experiment, the hydrogenation reaction of Li<sub>3</sub>N under 0.5 MPa of H<sub>2</sub> flow condition was investigated by DSC-MS. The clear exothermic peak was observed from 200 °C during the heating. This exothermic reaction was originated in the hydrogenation of Li<sub>3</sub>N to form a mixture of LiH and LiNH<sub>2</sub>. Following the process, the NH<sub>3</sub> generation was observed at 230 °C in MS profile, suggesting that the hydrogenation of LiNH<sub>2</sub> to form NH<sub>3</sub> and LiH proceeds at this temperature. Thus, it was demonstrated that the NH<sub>3</sub> production from Li<sub>3</sub>N can proceed in milder condition than that of “Haber-Bosch process” by using the objective two step reactions. To achieve a larger scale of NH<sub>3</sub> production, the D<sub>2</sub> flow system by using couple of hydrogen storage alloys was newly designed. The flow rate of more than 1 L /min without waste of D<sub>2</sub> gas can be realized in the system. As a result, 0.25 g /h of ND<sub>3</sub> production was demonstrated below 300°C and under 1.0 MPa of pressure.



# 公表論文

- (1) Ammonia Synthesis via Non-Equilibrium Reaction of Lithium Nitride  
in Hydrogen Flow Condition  
Kiyotaka Goshome, Hiroki Miyaoka, Hikaru Yamamoto, Tomoyuki  
Ichikawa, Takayuki Ichikawa, and Yoshitsugu Kojima  
Materials Transaction, **56** (3), 410-414 (2015).

# Ammonia Synthesis via Non-Equilibrium Reaction of Lithium Nitride in Hydrogen Flow Condition\*<sup>1</sup>

Kiyotaka Goshome<sup>1,\*2</sup>, Hiroki Miyaoka<sup>2</sup>, Hikaru Yamamoto<sup>1,\*3</sup>, Tomoyuki Ichikawa<sup>3</sup>, Takayuki Ichikawa<sup>1,4,\*4</sup> and Yoshitsugu Kojima<sup>1,4</sup>

<sup>1</sup>Graduate School of Advanced Sciences of Matter, Hiroshima University, Higashi-Hiroshima 739-8530, Japan

<sup>2</sup>Institute for Sustainable Sciences and Development, Hiroshima University, Higashi-Hiroshima 739-8530, Japan

<sup>3</sup>Hydrolabo Inc., Higashi-Hiroshima 739-8530, Japan

<sup>4</sup>Institute for Advanced Materials Research, Hiroshima University, Higashi-Hiroshima 739-8530, Japan

Lithium nitride Li<sub>3</sub>N is hydrogenated below 300°C under 0.5 MPa of H<sub>2</sub>, and then LiNH<sub>2</sub> and LiH are formed as products. Furthermore, the reaction between LiNH<sub>2</sub> and H<sub>2</sub> proceeds below 250°C under 0.5 MPa of H<sub>2</sub> flow condition, which forms NH<sub>3</sub> and LiH. In this study, we proposed and investigated another synthesis method of ammonia by combining these two reactions, which proceed in laboratory-scale under more moderate conditions than those of Haber–Bosch process. As a result, it was experimentally clarified that the ammonia synthesis were able to be operated below 300°C with realistic reactions rate by non-equilibrium reaction field under 0.5 MPa H<sub>2</sub> flow condition, where a gas circuit system and a larger scale NH<sub>3</sub> synthesis system were designed and assembled for the experiments. [doi:10.2320/matertrans.M2014382]

(Received October 29, 2014; Accepted December 17, 2014; Published February 6, 2015)

**Keywords:** ammonia synthesis, lithium nitride, non-equilibrium reaction

## 1. Introduction

Ammonia (NH<sub>3</sub>) has been produced on massive scale in the world and used as various feedstock of nitrogenous chemical products. Recently, NH<sub>3</sub> is regarded as hydrogen carrier for sustainable society, which potentially leads to strong demands for large-scale synthesis of NH<sub>3</sub> with high efficiency and moreover laboratory-scale synthesis of high purity NH<sub>3</sub> or deuterated ammonia (ND<sub>3</sub>) for fundamental researches on NH<sub>3</sub> utilization as energy carrier.<sup>1)</sup> Haber-Bosch process is a well-known ammonia synthesis technique for industrialized mass production. The annual production of NH<sub>3</sub> in the world by this Haber-Bosch process reached as much as 1.3 hundred million tons in 2010.<sup>2)</sup> Although this process is recognized as the most efficient method for large scale NH<sub>3</sub> production, it needs high temperature of 400–600°C and high pressure of 20–40 MPa even in the presence of iron oxide catalyst.<sup>3,4)</sup> Therefore, it should be difficult to adopt the process for the synthesis of high purity NH<sub>3</sub> or ND<sub>3</sub> in laboratory-scale.

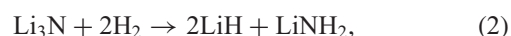
The reason that the production of NH<sub>3</sub> from H<sub>2</sub> and N<sub>2</sub> needs such high temperature and pressure even though the reaction is exothermic ( $\Delta H = 46$  kJ/mol NH<sub>3</sub>), is due to the strong triple bond between N atoms in N<sub>2</sub> molecule.<sup>5)</sup>

Therefore, it is an important issue how to dissociate N<sub>2</sub> efficiently for NH<sub>3</sub> synthesis under mild condition. In this view, the reaction of lithium (Li) with N<sub>2</sub> attracts attention, described by the following reaction (1),



Only Li is potential material to react with N<sub>2</sub> below 100°C, forming lithium nitride (Li<sub>3</sub>N).<sup>6)</sup> In other words, it is one of the simplest way to dissociate the nitrogen triple bond (N≡N), which possibly realizes the NH<sub>3</sub> synthesis under milder condition by reaction between Li<sub>3</sub>N and H<sub>2</sub>.

Therefore, we proposed NH<sub>3</sub> synthesis process applying reactions of the amide-imide hydrogen storage system<sup>7–11)</sup> and metal hydride-ammonia system,<sup>12–15)</sup> respectively described by the following reactions,



Since each reaction proceeds below 300°C and 0.5 MPa, it is expected that the NH<sub>3</sub> synthesis process under moderate condition becomes possible by optimizing the reaction condition. Regarding the cycle of materials, Li should be regenerated from LiH as the final product in reaction (3). However, the thermal decomposition of LiH requires more than 500°C. The effective regeneration process of Li metal below 300°C differently from simple decomposition is necessary, e.g. the metallic Li can be obtained below 500°C by using a reaction between crystalline graphite and LiH.<sup>16)</sup>

In this study, the reaction conditions of the proposed NH<sub>3</sub> synthesis process from Li<sub>3</sub>N were investigated by preparing various types of reaction systems, which were open system, closed gas circuit system, and closed system with gas exchange using hydrogen storage alloys, and the feasibility of the proposed process was discussed from the experimental results.

\*<sup>1</sup>This Paper was Originally Published in Japanese in J. Japan Inst. Met. Mater. 77 (2013) 580–584. In order to more precisely explain the background, the experimental procedures, and the results, some parts of the contents were revised as follows. X ray diffraction profile of lithium nitride powder and the corresponding patterns in database ( $\alpha$ -Li<sub>3</sub>N; PDF#75-8952 and  $\beta$ -Li<sub>3</sub>N; PDF#76-0821) were added in Fig. 4. The sentence of the abstract was slightly modified. References of 2–7), 15–19), and 20) were added and the reference of the Japanese website was removed from this paper.

\*<sup>2</sup>Graduate Student, Hiroshima University

\*<sup>3</sup>Hikaru Yamamoto who contributed to the development for the gas circuit apparatus is added as a coauthor in this paper on reconsidering the matter.

\*<sup>4</sup>Corresponding author, E-mail: tichi@hiroshima-u.ac.jp

## 2. Experimental Procedure

### 2.1 Investigation of NH<sub>3</sub> production from Li<sub>3</sub>N by DSC and MS

Commercial lithium nitride (Li<sub>3</sub>N) (99.5%, Aldrich) was used for the experiments in this work. The reaction of Li<sub>3</sub>N with H<sub>2</sub> for NH<sub>3</sub> production was investigated by using differential scanning calorimetry (DSC) (TA Instruments, Q10 PDSC), which is installed into a glove box (Miwa MFG, MP-P60 W) filled with purified Ar (> 99.9999%). The generated gases during the DSC measurements is *in-situ* monitored by using mass spectrometry (MS) (Canon Anelva Corporation, M-100QA), which is connected to the reactor of DSC apparatus. The reaction condition using H<sub>2</sub> flow is regarded as thermodynamic non-equilibrium state because the gaseous product, NH<sub>3</sub>, is immediately removed from the reaction field. The solid samples before and after the reaction were identified by X-ray diffraction (XRD) measurement (Rigaku, RINT-2100, CuKα radiation), where the samples were covered by a polyimide sheet (Du Pont-Toray Co., LTD., Kapton<sup>®</sup>) to protect the samples from oxidation during XRD measurements.

### 2.2 Investigation of NH<sub>3</sub> production from LiNH<sub>2</sub> in gas circuit system

In order to realize the reaction (3) in closed system, a gas circuit system was designed. Figure 1 shows the schematic image of the gas circulating system designed for this experiment. This apparatus includes a gas densimeter (Yokogawa Electric Corporation, GD400), circulation pump (Nittou kouatsu), gas flow meter (ACE Inc., AFM-150), pressure gauge, and NH<sub>3</sub> trap chamber. A reaction cell loading a weighed amount (42 mg) of commercial LiNH<sub>2</sub> (LiNH<sub>2</sub>) (95%, Aldrich) was connected to the gas circuit system and 0.5 MPa H<sub>2</sub> with a molar ratio of H<sub>2</sub>/LiNH<sub>2</sub> = 100 was introduced. After that, the experiments were carried out under gas circulated condition with 16 and 88 sccm (= cc min<sup>-1</sup> at 0.1 MPa, 0°C) of flow rates at 300°C. NH<sub>3</sub> trap using liquid N<sub>2</sub> was used to reduce the partial pressure of NH<sub>3</sub> in the circuit system. In order to estimate the reaction yield, the amount of NH<sub>3</sub> trapped during the reaction was measured by using a gas densimeter. The solid materials were identified by XRD before and after the reaction.

### 2.3 Scale up test for NH<sub>3</sub> and ND<sub>3</sub> synthesis

Mixture of LiD and LiND<sub>2</sub> were synthesized as starting materials for this experiments by reaction between Li<sub>3</sub>N (99.5%, Aldrich) and high purity D<sub>2</sub> gas (> 99.8%) instead of the reaction (2). In order to realize a certain amount of D<sub>2</sub> flow condition for the reaction (3), gas collecting system by hydrogen storage alloys without waste of D<sub>2</sub> was designed and assembled. Figure 2 shows the schematic image of the closed H<sub>2</sub> flow system used for scale up test. This system is composed of reaction cell, hydrogen storage tanks, heaters, pressure gauge, flow meter, and NH<sub>3</sub> trap. The couple of tanks loaded by the same hydrogen storage alloy were connected to both ends of reaction cell and thermally controlled. Then, a sufficient amount of mixture of LiD and LiND<sub>2</sub> loaded in the reaction cell and heated under D<sub>2</sub> flow condition (1.0 MPa, 1.0 L min<sup>-1</sup>) at 300°C with ND<sub>3</sub> trap.

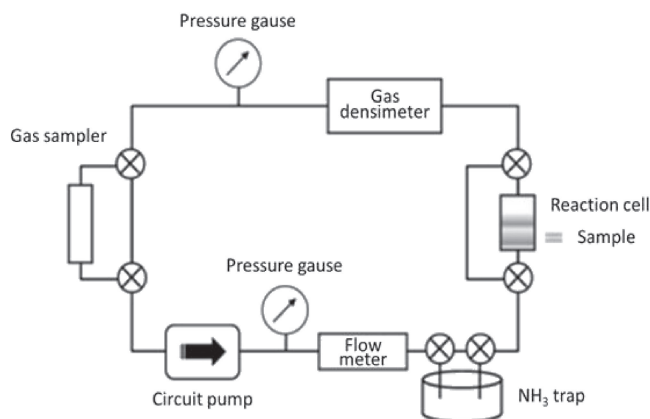


Fig. 1 Schematic view of gas circuit system.

After the reaction, the amount of generated ND<sub>3</sub> in the trap was weighted.

## 3. Result and Discussions

### 3.1 Investigation of NH<sub>3</sub> production from Li<sub>3</sub>N by DSC and MS

Hydrogenation of Li<sub>3</sub>N under H<sub>2</sub> flow was investigated by DSC and MS. Since the NH<sub>3</sub> production reaction of LiH-NH<sub>3</sub> system described by reaction (3) is endothermic reaction, the thermodynamics should be considered to control the reaction process at a moderate temperature. Gibbs free energy change  $\Delta G$  on this reaction is expressed as follows,

$$\Delta G = \Delta H - T(\Delta S^0 + R \ln(P_{H_2}/P_{NH_3})) \quad (4)$$

where  $\Delta H$ ,  $\Delta S^0$ ,  $R$ ,  $P_{H_2}$ , and  $P_{NH_3}$  are, respectively, the enthalpy change, the standard entropy change, the gas constant, partial pressure of H<sub>2</sub>, and partial pressure of NH<sub>3</sub>. In order to manage the reaction progress at lower temperature, it is essential to decrease the value of the last entropy term in the equation (4). In the DSC-MS experiments, the reaction was investigated under the H<sub>2</sub> flow condition in an open system, suggesting that the value of the entropy is increased by reducing  $P_{NH_3}$ . Figure 3 shows the DSC-MS profile of Li<sub>3</sub>N under 0.5 MPa of the H<sub>2</sub> flow condition. As shown in this DSC profile, exothermic peak was observed from 200°C during heating, which would be originated in the hydrogenation of Li<sub>3</sub>N described by the reaction (2). The temperature for this reaction is consistent with the results reported before.<sup>8)</sup> It is also possible that the reaction (3) proceeds 200°C in this condition.<sup>14)</sup> However, it is difficult to distinguish the reaction temperature because the smaller endothermic peak due to the reaction (3) would be overlapped with the larger exothermic peak due to the reaction (2). In the mass spectra, generation of NH<sub>3</sub> gas was clearly observed above 230°C. It was expected that the NH<sub>3</sub> generation originated in hydrogenation of LiNH<sub>2</sub>. The onset temperature for NH<sub>3</sub> desorption was about 230°C, which was closed to that reported before.<sup>14)</sup> The NH<sub>3</sub> desorption intensity was increased with during the heating, indicating that the reaction (3) gradually proceeds from 230°C after the LiNH<sub>2</sub> formation by the reaction (2) around 200°C. Here, the MS detection of our experimental system is slightly delayed

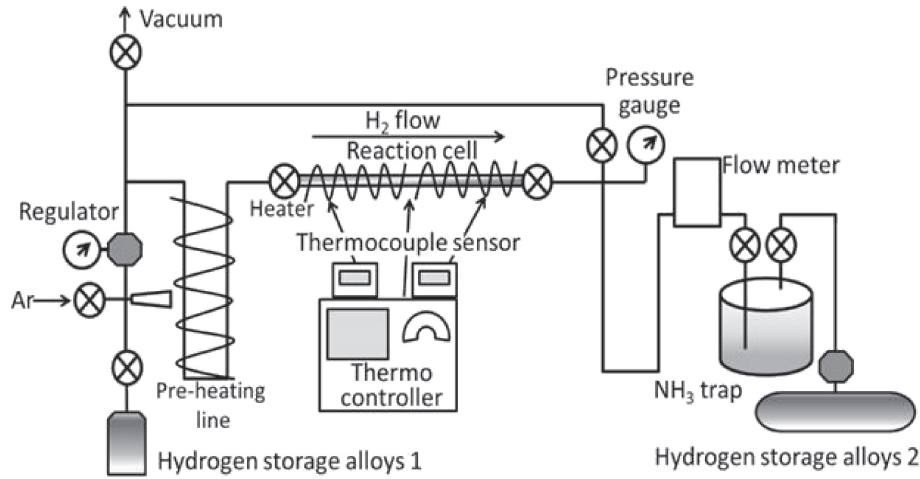


Fig. 2 Schematic view of D<sub>2</sub> flow system for ND<sub>3</sub> synthesis.

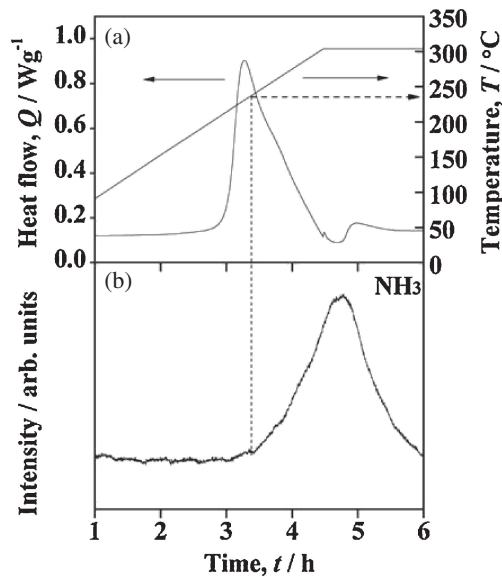


Fig. 3 DSC (a)-MS (b) profiles of Li<sub>3</sub>N under 0.5MPa of H<sub>2</sub> flow condition at 1.0°C min<sup>-1</sup> heating rate. NH<sub>3</sub> generation temperature is indicated with the auxiliary line (---).

from the DSC signal with fast response, and the reaction kinetics of the light elements based materials are generally slow. From the above facts, it is suggested that the accurate reaction temperature of (3) is difficult to be distinguished. Figure 4 shows XRD pattern of the product after the DSC-MS measurement. The X-ray diffraction peaks of LiH was observed as the reaction product without any traces for the diffraction peaks of Li<sub>3</sub>N and LiNH<sub>2</sub>. This indicates that the LiNH<sub>2</sub> generated by the prior hydrogenation of Li<sub>3</sub>N gradually reacted with H<sub>2</sub> to form NH<sub>3</sub> and LiH. Here, Li<sub>2</sub>O phase observed in XRD profile would be derived from impurity in the reagent. Generally, X-ray diffraction intensity is strongly related to electron number of atoms in the material. If the amount of Li<sub>2</sub>O is considerable in the samples, the diffraction intensity has to be much stronger than that of LiH. Thus, it is considered that the amount of the impurity was small by taking account of the intensity of LiH phase and Li<sub>2</sub>O phase, suggesting that any effects of the impurity into the essential reaction could be negligible. From

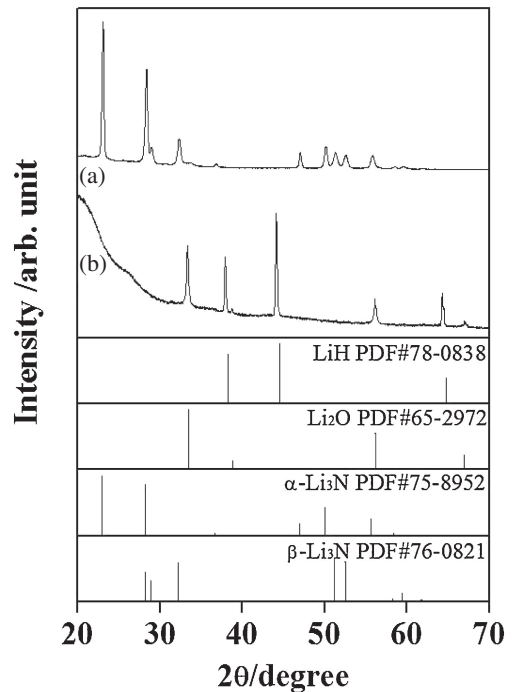


Fig. 4 XRD patterns of Li<sub>3</sub>N before: (a) and after: (b) the treatment under H<sub>2</sub> flow condition for 4 h at 300°C. XRD pattern of LiH (PDF#78-0838), Li<sub>2</sub>O (PDF#65-2972), α-Li<sub>3</sub>N (PDF#75-8952) β-Li<sub>3</sub>N (PDF#76-0821) are referred from databases.

the above results, it was confirmed that the objective two-step process for NH<sub>3</sub> production proceeded under relatively lower temperature and pressure in the H<sub>2</sub> flow condition. In thermodynamic analyses based on the experimental results and equation (4), the partial pressure of NH<sub>3</sub> is reduced to be 4~12 Pa as an overestimation under the experimental conditions, where the  $\Delta H$  and  $\Delta S^0$  were calculated by combining reported  $\Delta^f H^0$  and  $S^0$  values as shown in Table 1,  $-90.5 \text{ kJ mol}^{-1}$  and  $20.0 \text{ J mol}^{-1} \text{ K}^{-1}$  for LiH,  $-45.9 \text{ kJ mol}^{-1}$  and  $192.8 \text{ J mol}^{-1} \text{ K}^{-1}$  for NH<sub>3</sub>,  $130.7 \text{ J mol}^{-1} \text{ K}^{-1}$  for H<sub>2</sub>,  $-179.5 \text{ kJ mol}^{-1}$  for LiNH<sub>2</sub>,<sup>17-19</sup> and approximate  $S^0$  values of LiNH<sub>2</sub>, 80~90 J mol<sup>-1</sup> K<sup>-1</sup> which is similar to the  $S^0$  value of complex hydrides such as LiBH<sub>4</sub> and LiAlH<sub>4</sub>.<sup>20</sup>

Table 1 Standard enthalpy of formation and standard entropy for H<sub>2</sub>, NH<sub>3</sub>, LiH, and LiNH<sub>2</sub>.

Compounds	Enthalpy of formation $\Delta_f H^\circ$ (kJ·mol <sup>-1</sup> )	Entropy $S^\circ$ (J·K <sup>-1</sup> ·mol <sup>-1</sup> )
LiH (s)	-90.5	20
LiNH <sub>2</sub> (s)	-179.5	80-90*
H <sub>2</sub> (g)	0	130.7
NH <sub>3</sub> (g)	-45.9	192.8

\*Assumed  $S^\circ$  value for LiNH<sub>2</sub>.

### 3.2 Investigation of NH<sub>3</sub> production from LiNH<sub>2</sub> in gas circuit system

From the above DSC experiments, the feasibility of NH<sub>3</sub> generation from Li<sub>3</sub>N under H<sub>2</sub> flow was demonstrated. In the process, the reaction (2) is not difficult to be operated because this exothermic reaction proceeds even at closed system. In order to control the proposed NH<sub>3</sub> production process, the most important issue is how to control the reaction (3). Thus, the hydrogenation property of LiNH<sub>2</sub> was further investigated in closed-circuit system. For the experiment, the gas circuit apparatus was used as mentioned in the experimental part. By using the gas circuit system, it becomes possible to *in-situ* measure the concentration of H<sub>2</sub> for NH<sub>3</sub> under a certain pressure and gas flow rate in the circulating system. Additionally, NH<sub>3</sub> trap by using liquid N<sub>2</sub> is equipped into the circulating line, thus the generated NH<sub>3</sub> can be removed from the circulated gases. It is expected that the partial pressure of NH<sub>3</sub> is reduced to a sufficient level to realize the progress of reaction (3) because the temperature of liquid N<sub>2</sub> is low enough compared with the freezing point of NH<sub>3</sub>. Here, the inner volume of the trap part is sufficiently-large. Thus, almost all the generated NH<sub>3</sub> can be trapped even if the experiments are performed by a maximum circuit rate, in other words, the generated NH<sub>3</sub> is not reached to sample part again during the circulation. As described above, it is essential to control the entropy change by reducing NH<sub>3</sub> partial pressure for the hydrogenation of LiNH<sub>2</sub>. Therefore, the investigation for hydrogenation reaction of Li<sub>3</sub>N was performed under H<sub>2</sub> flow condition in open system by DSC-MS in section 3.1. However, such flow condition, which exhausts unreacted H<sub>2</sub> and generated NH<sub>3</sub> gases, is totally different from practical condition, because the hydrogen gas has to be consumed a lot in the open system. On the other hand, in the case of above gas circuit system, it is expected that the hydrogenation reaction proceeds even in closed system without the H<sub>2</sub> loss, which would be more practical condition than that of DSC experiments. Figure 5 shows XRD pattern of the product after the LiNH<sub>2</sub> hydrogenating treatment for 8 h at 300°C, where the circulating rate was 16 sccm. Although diffraction peaks corresponding to LiH was observed, it was confirmed that a trace of LiNH<sub>2</sub> remained in the product. In this case, the reaction yield was 35.6%. These results indicated that the  $P_{\text{NH}_3}$  was reduced to less than 12 Pa and the reaction proceeded by using the circulating system because LiH was clearly generated. However, the 16 sccm of circuit rate was not enough to reach the same level of  $P_{\text{NH}_3}$  as the DSC condition due to slow diffusion rate of NH<sub>3</sub> gas in the solid sample part,

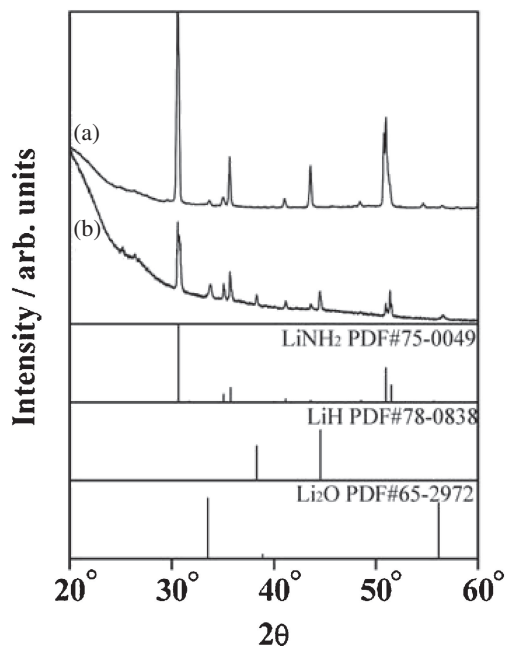


Fig. 5 XRD patterns of LiNH<sub>2</sub> before: (a) and after: (b) the treatment under 16 sccm H<sub>2</sub> flow condition for 8 h at 300°C. XRD pattern of LiNH<sub>2</sub> (PDF#75-0049), LiH (PDF#78-0838), and Li<sub>2</sub>O (PDF#65-2972) are referred from databases.

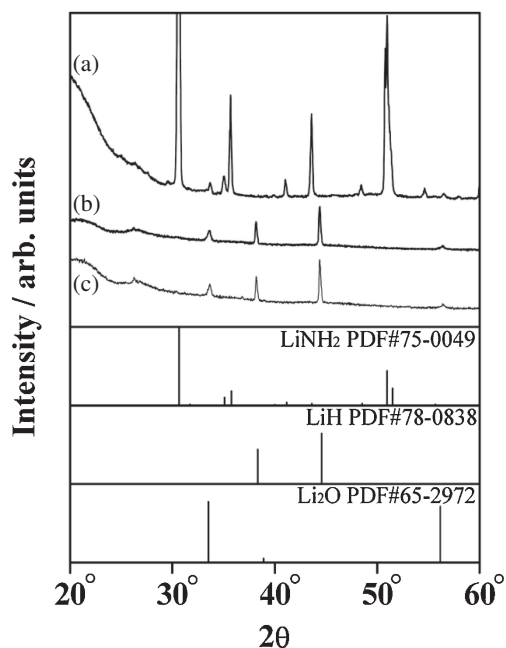


Fig. 6 XRD patterns of LiNH<sub>2</sub> before: (a) and after the treatment under 88 sccm H<sub>2</sub> flow condition for 4 h: (b) and 6 h: (c) at 300°C. XRD pattern of LiNH<sub>2</sub> (PDF#75-0049), LiH (PDF#78-0838), and Li<sub>2</sub>O (PDF#65-2972) are referred from databases.

indicating that NH<sub>3</sub> was not removed enough from reaction field. Therefore, the reaction condition was changed to higher circulating rate of 88 sccm. Figure 6 shows XRD pattern of the product in circulating system for 4 h and 6 h at 300°C. The diffraction peaks corresponding to LiNH<sub>2</sub> observed after the experiments with 16 sccm totally disappeared. Here, in these experiments, although a small amount of Li<sub>2</sub>O derived from impurity in the reagent was observed by XRD, it would

not influence the quantitative discussion because of the same reason as section 3.1. The reaction yields for 4 and 6 h were estimated from  $\text{NH}_3$  concentration by using the gas densimeter, and the values were respectively 75.3% and 91.6%. As described above, it is important to decrease the partial pressure of  $\text{NH}_3$  by diffusing  $\text{NH}_3$  gas effectively from the reaction field for the reaction (3). In this experiment by using gas circulating system, the gas in the closed system was circulated and simultaneously  $\text{NH}_3$  was trapped. As the results, sufficiently low  $P_{\text{NH}_3}$  and highly efficient condition for  $\text{NH}_3$  production can be realized when the faster circulating rate.

### 3.3 Scale up test for $\text{ND}_3$ synthesis

The scale up test of the reaction (3) for the  $\text{ND}_3$  synthesis was performed. As described above, a certain diffusion rate of generated  $\text{NH}_3$  from reaction field is important for efficient  $\text{NH}_3$  production from  $\text{LiNH}_2$ . Therefore, it is necessary to make the higher  $\text{H}_2$  flow rate for larger scale  $\text{NH}_3$  production. Thus, the gas flow system with higher  $\text{H}_2$  flow rate by hydrogen storage alloys was designed and assembled. When the temperatures of the tanks were controlled in high and low temperatures, the pressure gradient was generated because of different  $\text{H}_2$  equilibrium pressure of the hydrogen storage alloy. By this pressure difference, it was expected that the sufficient  $\text{H}_2$  flow condition through reaction cell is realized. In this process, the unreacted  $\text{H}_2$  is collected into the alloys controlled at lower temperature, and  $\text{H}_2$  can be reused by exchanging the flow direction with temperature control of tanks. As a result, the  $\text{H}_2$  loss except the  $\text{NH}_3$  generation reaction is suppressed, where this would be advantage point as productive  $\text{NH}_3$  synthesis. In the actual experiment, we used  $\text{D}_2$  gas instead of  $\text{H}_2$  gas. Then the pressure and flow rate of inside gas were monitored, and the generated  $\text{ND}_3$  was collected in the trap. It was clarified that flow rate prepared by this reaction system was  $1.0 \text{ L min}^{-1}$ , which is approximately ten times faster than that required in the above circulating system to complete the reaction. By using this reaction system,  $1.0 \text{ g ND}_3$  was successfully produced by heating the mixture of  $\text{LiD}$  and  $\text{LiND}_2$  in  $1.0 \text{ MPa}$  of  $\text{D}_2$  flow condition with  $1.0 \text{ L min}^{-1}$  of flow rate at  $300^\circ\text{C}$  for 4 h, resulting in  $0.25 \text{ g h}^{-1}$  of production rate. Whereas Haber-Bosch process needs high temperature of  $400\text{--}600^\circ\text{C}$  and high pressure of  $20\text{--}40 \text{ MPa}$ , the result in this study indicates that the  $\text{NH}_3$  production by the reactions (1) and (2) can be operated under comparatively mild condition and is remarkably useful as efficient  $\text{ND}_3$  synthesis method in laboratory-scale.

## 4. Conclusions

In this work,  $\text{NH}_3$  production by the hydrogenation  $\text{Li}_3\text{N}$  and the reaction of  $\text{LiNH}_2$  and  $\text{H}_2$  were investigated to propose a novel  $\text{NH}_3$  synthesis method in laboratory-scale.

As a result, the  $\text{NH}_3$  generation from  $\text{Li}_3\text{N}$  in  $0.5 \text{ MPa}$  of  $\text{H}_2$  flow condition below  $300^\circ\text{C}$  was confirmed by DSC-MS and XRD, indicating that the  $\text{NH}_3$  production from  $\text{Li}_3\text{N}$  can proceed in milder condition than conventional method by using the objective two step reactions. For the investigation of  $\text{NH}_3$  generation from  $\text{LiNH}_2$  in the closed system, a gas circuit system was designed and used for the experiment. The system can circulate mixture gas of  $\text{NH}_3$  and  $\text{H}_2$  with enough flow rate and reduce the partial pressure of  $\text{NH}_3$  by the trap using liquid  $\text{N}_2$ . As a result, it was clarified that  $\text{NH}_3$  generation proceeded even in the closed system, which would be considered as more practical condition. Furthermore,  $\text{NH}_3$  synthesis test on a larger scale was conducted, where the higher  $\text{D}_2$  flow system by pressure gradient between couple of hydrogen storage alloy tanks was designed for the experiment. By using the system, a certain amount of  $\text{ND}_3$  production at realistic reaction rate ( $0.25 \text{ g h}^{-1}$ ) was demonstrated in  $1.0 \text{ L min}^{-1}$  of  $\text{D}_2$  flow condition below  $300^\circ\text{C}$  and  $1.0 \text{ MPa}$ .

## REFERENCES

- 1) U.S. Department of Energy: Potential Roles of Ammonia in a Hydrogen Economy, <http://www.hydrogen.energy.gov/pdfs/nh3-paper.pdf>
- 2) R. Lan, J. T. S. Irvine and S. W. Tao: *Int. J. Hydrogen Energy* **37** (2012) 1482–1494.
- 3) A. Barański, A. Kotarba, J. M. Lagan, A. Pattekkjanczyk, E. Pyrczak and A. Reizer: *Appl. Catal. A-Gen.* **112** (1994) 13–36.
- 4) T. Kandemir, M. E. Schuster, A. Senyshyn, M. Behrens and R. Schlogl: *Angew. Chem. Int. Ed.* **52** (2013) 12723–12726.
- 5) N. D. Spencer, R. C. Schoonmaker and G. A. Somorjai: *J. Catal.* **74** (1982) 129–135.
- 6) T. Arakawa and K. Takizawa: JP2002-3209A (2002).
- 7) P. Chen, Z. T. Xiong, J. Z. Luo, J. Y. Lin and K. L. Tan: *J. Phys. Chem. B* **107** (2003) 10967–10970.
- 8) P. Chen, Z. T. Xiong, J. Z. Luo, J. Y. Lin and K. L. Tan: *Nature* **420** (2002) 302–304.
- 9) T. Ichikawa, N. Hanada, S. Isobe, H. Y. Leng and H. Fujii: *J. Phys. Chem. B* **108** (2004) 7887–7892.
- 10) T. Ichikawa, S. Isobe, N. Hanada and H. Fujii: *J. Alloy. Compd.* **365** (2004) 271–276.
- 11) S. Isobe, T. Ichikawa, S. Hino and H. Fujii: *J. Phys. Chem. B* **109** (2005) 14855–14858.
- 12) H. Miyaoka, H. Fujii, H. Yamamoto, S. Hino, H. Nakanishi, T. Ichikawa and Y. Kojima: *Int. J. Hydrogen Energy* **37** (2012) 16025–16030.
- 13) H. Miyaoka, T. Ichikawa, S. Hino and Y. Kojima: *Int. J. Hydrogen Energy* **36** (2011) 8217–8220.
- 14) H. Yamamoto, H. Miyaoka, S. Hino, H. Nakanishi, T. Ichikawa and Y. Kojima: *Int. J. Hydrogen Energy* **34** (2009) 9760–9764.
- 15) Y. H. Hu and E. Ruckenstein: *J. Phys. Chem. A* **107** (2003) 9737–9739.
- 16) H. Miyaoka, W. Ishida, T. Ichikawa and Y. Kojima: *J. Alloy. Compd.* **509** (2011) 719–723.
- 17) D. R. Lide: *CRC Handbook of Chemistry and Physics, 89th ed.*, (CRC press, London, 2008).
- 18) M. W. Chase: *J. Phys. Chem. Ref. Data Monogr.* **9** (1998) 1224–1293.
- 19) S. Hino, N. Ogita, M. Udagawa, T. Ichikawa and Y. Kojima: *J. Appl. Phys.* **105** (2009) 023527.
- 20) NIST Web book, <http://webbook.nist.gov/chemistry>

# 参考論文

- (1) Lithium Hydrazinidoborane: A Polymorphic Material with Potential for Chemical Hydrogen Storage  
Romain Moury, Umit B. Demirci, Voraksmy Ban, Yaroslav Filinchuk, Takayuki Ichikawa, Liang Zeng, Kiyotaka Goshome, and Philippe Miele  
*Chemistry of Materials*, **26**(10), 3249-3255 (2014).

# Lithium Hydrazinidoborane: A Polymorphic Material with Potential for Chemical Hydrogen Storage

Romain Moury,<sup>†</sup> Umit B. Demirci,<sup>\*,†</sup> Voraksmy Ban,<sup>‡</sup> Yaroslav Filinchuk,<sup>‡</sup> Takayuki Ichikawa,<sup>§</sup> Liang Zeng,<sup>||</sup> Kiyotaka Goshome,<sup>||</sup> and Philippe Miele<sup>†</sup>

<sup>†</sup>IEM (Institut Européen des Membranes), UMR5635 (CNRS, ENSCM, UM2), Université Montpellier 2, Place Eugene Bataillon, CC047, F-34095, Montpellier, France

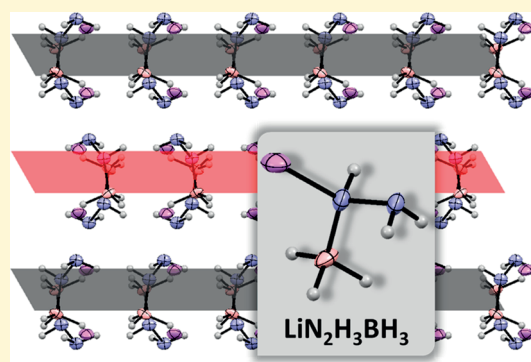
<sup>‡</sup>Institute of Condensed Matter and Nanosciences, Université Catholique de Louvain, Place L. Pasteur 1, 1348 Louvain-la-Neuve, Belgium

<sup>§</sup>Institute for Advanced Materials Research, Hiroshima University, 1-3-1 Kagamiyama, Higashi-Hiroshima, 739-8530, Japan

<sup>||</sup>Graduate School of Advanced Sciences of Matter, Hiroshima University, 1-3-1 Kagamiyama, Higashi-Hiroshima, 739-8530, Japan

## Supporting Information

**ABSTRACT:** Herein, we describe the synthesis and characterization (chemical, structural, and thermal) of a new crystal phase of lithium hydrazinidoborane ( $\text{LiN}_2\text{H}_4\text{BH}_3$ , LiHB), which is a new material for solid-state chemical hydrogen storage. We put in evidence that lithium hydrazinidoborane is a polymorphic material, with a stable low-temperature phase and a metastable high-temperature phase. The former is called  $\beta$ -LiHB and the latter  $\alpha$ -LiHB. Results from DSC and XRD showed that the transition phase occurs at around 90 °C. On this basis, the crystal structure of the novel  $\beta$ -LiHB phase was solved. The potential of this material for solid-state chemical hydrogen storage was verified by TGA, DSC, and isothermal dehydrogenations. Upon the formation of the  $\alpha$ -LiHB phase, the borane dehydrogenates. At 150 °C, it is able to generate 10 wt % of pure  $\text{H}_2$  while a solid residue consisting of polymers with linear and cyclic units forms. Reaction mechanisms and formation of bis(lithium hydrazide) of diborane  $[(\text{LiN}_2\text{H}_3)_2\text{BH}_2]^+[\text{BH}_4]^-$  as a reaction intermediate are tentatively proposed to highlight the decomposition of  $\beta$ -LiHB in our conditions.



## INTRODUCTION

Solid-state chemical hydrogen storage is a recent field in material science and has shown to have high potential to address the storage issue of the near-future hydrogen economy.<sup>1</sup> Technically, the ultimate objective is to find a way to store hydrogen safely and in high amounts.<sup>2</sup>

In this context, boron- and/or nitrogen-based materials, though not storing hydrogen reversibly, have shown to be very attractive candidates for carrying high amounts of hydrogen, which is of high interest for some (military and niche) applications. Ammonia borane  $\text{NH}_3\text{BH}_3$  (AB) is a typical example: (i) it is stable in ambient conditions if kept under an argon atmosphere,<sup>3</sup> and (ii) it is composed of 3  $\text{H}^{\delta+}$  and 3  $\text{H}^{\delta-}$  per 1 B and 1 N, and theoretically stores 19.6 wt % H. Accordingly, AB meets the aforementioned criteria for suitability in solid-state chemical hydrogen storage.<sup>4</sup>

Ammonia borane is stable upon heating at a constant rate up to ca. 100 °C, the temperature at which it starts to decompose.<sup>5</sup> However, over the temperature range of 100–200 °C, AB loses 40–60 wt % because of the release of  $\text{H}_2$ , but also of unwanted gaseous byproducts, such as borazine  $\text{B}_3\text{N}_3\text{H}_6$ , diborane  $\text{B}_2\text{H}_6$ , and aminoborane  $\text{NH}_2\text{BH}_2$ .<sup>5,6</sup> The thermolytic decomposition

suffers thus from two main drawbacks: a high onset temperature of dehydrogenation and the impurity of the released  $\text{H}_2$ . To solve these issues, various strategies of AB destabilization have been considered so far.<sup>7</sup> One of them focuses on chemical modification of AB to get derivatives that are less stable than the parent material. For example, Xiong et al. synthesized metal amidoboranes  $\text{MNH}_2\text{BH}_3$  (MAB) by ball-milling AB and an alkaline hydride MH (with M = Li and Na), and demonstrated the positive effect of such a destabilization with an onset temperature of dehydrogenation decreased to ca. 60 °C and liberation of  $\text{H}_2$  without borazine.<sup>8</sup> However, for sodium amidoborane  $\text{NaNH}_2\text{BH}_3$ , Fijalkowski et al. reported emission of ammonia.<sup>9</sup>

Recently, hydrazine borane  $\text{N}_2\text{H}_4\text{BH}_3$  (HB), another boron- and nitrogen-based material, emerged. It has been presented as an alternative to AB.<sup>10</sup> HB has a gravimetric capacity of 15.3 wt % H. Upon heating at 5 °C  $\text{min}^{-1}$ , it decomposes from ca. 60 °C.<sup>10,11</sup> In a previous work,<sup>11</sup> we showed that, over the range of

Received: March 20, 2014

Revised: May 5, 2014

Published: May 6, 2014

60–95 °C, HB loses 1.2 wt % of pure H<sub>2</sub>, but from 95 °C, the mass loss is significant, due to emission of hydrazine and/or ammonia. Unlike AB, no trace of borazine is detected. Actually, the situation is similar to that faced with AB: the challenges with HB are to decrease the onset temperature of dehydrogenation while avoiding the release of unwanted byproducts.

Wu et al. and then our group proposed to destabilize HB by ball-milling the borane in the presence of an equimolar amount of LiH and NaH, respectively.<sup>12,13</sup> Therefore, Wu et al. synthesized lithium hydrazinidoborane LiN<sub>2</sub>H<sub>3</sub>BH<sub>3</sub> (LiHB; 11.6 wt % H).<sup>12</sup> We successfully prepared sodium hydrazinidoborane NaN<sub>2</sub>H<sub>3</sub>BH<sub>3</sub> (NaHB; 8.8 wt % H).<sup>13</sup> Both materials possess 3 H<sup>δ-</sup> in tandem with 3 H<sup>δ+</sup>, and they could theoretically release up to 3 mol of H<sub>2</sub> per mole of metal hydrazinidoborane. In practical terms, LiN<sub>2</sub>H<sub>3</sub>BH<sub>3</sub> is able to liberate 9.3 wt % of H<sub>2</sub> under heating at 130 °C for 1 h,<sup>12</sup> and NaN<sub>2</sub>H<sub>3</sub>BH<sub>3</sub> releases 8.1 wt % of H<sub>2</sub> with very fast desorption kinetics when heated at 100 °C for 1 h.<sup>13</sup> Accordingly, both boranes have attractive features for solid-state chemical hydrogen storage.

In 2012, when Wu et al. published their work on LiHB,<sup>12</sup> we were also working on the mechanosynthesis of this material from lab-made HB and commercial LiH. However, we were triggering repeatability problems with our successive syntheses. Finally, we evidenced the formation of two polymorphs of LiHB in this system. Hence, we report herein the mechanochemical synthesis procedure, characterization results, and thermal and dehydrogenation properties of a new crystal phase of LiHB. We have called the Wu et al.'s phase  $\alpha$ -LiHB and our new phase  $\beta$ -LiHB.

## EXPERIMENTAL DETAILS

**Materials and Synthesis.** Commercial sodium borohydride NaBH<sub>4</sub> (Acros, 99%), hydrazine hemisulfate N<sub>2</sub>H<sub>4</sub>·1/2(SO<sub>4</sub>) (Aldrich, >99%), anhydrous 1,4-dioxane (Sigma-Aldrich, >99%), and lithium hydride LiH (Sigma-Aldrich, 95%) were used as-received. They were stored and handled in an argon-filled glovebox (MBraun M200B, H<sub>2</sub>O ≤ 0.1 ppm, O<sub>2</sub> ≤ 0.1 ppm). The solvent was used under an argon flow. HB was synthesized following a procedure we had optimized.<sup>11</sup> Typically, sodium borohydride and hydrazine hemisulfate were introduced in a round-bottom Schlenk glassware, followed by 1,4-dioxane. The slurry was kept under stirring during 48 h in ambient conditions. Then, the reaction mixture was filtered off and the filtrate was dried under vacuum. HB with a purity of ≥99% was obtained and stored in the glovebox. The synthesis of  $\beta$ -LiHB was performed by mechanochemical synthesis. In the argon-filled glovebox, equimolar amounts of HB and LiH were transferred in a stainless steel grinding jar. The weight ratio of balls over reactants (denoted R) was set at 200:1. After sealing, the jar was removed outside the glovebox, and the mixture was ball-milled by using a RETSCH PM 100 planetary ball mill. The milling conditions were optimized to the following parameters: 10 min of milling, followed by a 20 min break, 18 times, 200 rpm, and at ambient conditions. Finally, the jar was transferred into the glovebox and the sample recovered by sieving. The as-synthesized  $\beta$ -LiHB was stored and handled in the glovebox. For comparison with  $\beta$ -LiHB,  $\alpha$ -LiHB was prepared. Equimolar amounts of LiH and HB were put in a stainless steel grinding jar in the glovebox such as R = 200:1. Two milling cycles were necessary. During the first one, the mixture was ball-milled for 10 min, followed by a break of 10 min; this was done 10 times at 200 rpm at ambient conditions. The solid was recovered by sieving in the glovebox. The second cycle was performed as follows: 10 min of milling, 50 min of break, 18 times, 300 rpm, at ambient conditions. The as-obtained  $\alpha$ -LiHB was recovered by sieving in the glovebox. The XRD pattern is shown in Figure 2a and is compared to that of  $\beta$ -LiHB.

**Characterizations.** The crystal structure of  $\beta$ -LiHB (loaded in a 0.5 mm diameter glass capillary under an inert atmosphere) was analyzed by powder X-ray diffraction (XRD) with synchrotron radiation at the ESRF at the BM01 beamline (SNBL). The wavelength was  $\lambda = 0.69405$  Å. A 2D detector Pilatus 2 M positioned at 411 mm from the sample was used, and the detector geometry was calibrated with a LaB<sub>6</sub> standard. The molecular structure of  $\beta$ -LiHB was analyzed by Fourier transform infrared (FTIR) spectroscopy (Nicolet 710, 32 scans) and by <sup>11</sup>B MAS NMR (Varian VNMR400, 128.37 MHz). Thermogravimetric analyses (TGA) were performed using Rigaku TG8120 coupled with an M-QA200TS mass spectrometer under helium flux. The measurement was directly recorded inside an argon-filled glovebox. About 3 mg of product was loaded in a platinum crucible and then analyzed with a heating rate of 2 °C min<sup>-1</sup>. The same experimental conditions were used for differential scanning calorimetry (DSC, TA Instruments, Q10PDS). Thermal behavior under prolonged heating at constant temperature (90, 110, 140, and 150 °C) was investigated with our lab-made bench. The sample in a round-bottom Schlenk flask was heated by immersing the glassware in a thermostated oil bath. The volume of H<sub>2</sub> was followed with an inverted buret filled with colored water, the volume variation being video-recorded and afterward plotted using the Matlab software. Between the Schlenk flask and the inverted buret, a cold trap (kept at 0 °C) and a Dräger tube were placed in order to condensate any evolving hydrazine and to trap ammonia, respectively. The purity of H<sub>2</sub> after isothermal treatment was investigated by gas chromatography (Shimadzu, GC-14B; Column Chromosorb 103 (porous polymer adsorbent); 40 °C; Detector TCD). For both H<sub>2</sub> and NH<sub>3</sub>, 2250 points were recorded every 0.4 s for 15 min; the retention times were 1.57 and 5.57 min, respectively.

## RESULTS AND DISCUSSION

**Molecular Structure of  $\beta$ -LiHB.** The FTIR spectrum of  $\beta$ -LiHB is displayed in Figure 1a. The fingerprint of the N–H stretching bands (3390–3070 cm<sup>-1</sup>) of  $\beta$ -LiHB is less complex than that observed for HB (3500–2600 cm<sup>-1</sup>). This suggests that the N–H bonds of the hydrazinidoborane are involved in a smaller number of N–H···H–B interactions. The H<sup>δ+</sup>···H<sup>δ-</sup> network within  $\beta$ -LiHB should be weaker, which is a sign of decreased stability in comparison to HB. This effect is confirmed by the broadened N–H bending and rocking bands (1300–1800 cm<sup>-1</sup>). With respect to the B–H stretching region (2480–1900 cm<sup>-1</sup>), there are more bands, especially at lower wavenumbers than for HB (2500–2100 cm<sup>-1</sup>).

The Li<sup>+</sup> cation would interact with the H<sup>δ-</sup> of the BH<sub>3</sub> group, leading to different environments for the B–H bonds. The polarization of these bonds, and thus their reactivity, should have changed in comparison to HB. Concerning the N–N and B–N stretching regions for  $\beta$ -LiHB, the bands have red- and blue-shifted, respectively:  $\nu(\text{N–N}) = 1050$  cm<sup>-1</sup> and  $\nu(\text{B–N}) = 748$  cm<sup>-1</sup> for  $\beta$ -LiHB vs  $\nu(\text{N–N}) = 1022$  cm<sup>-1</sup> and  $\nu(\text{B–N}) = 781$  cm<sup>-1</sup> for HB. This is indicative of weaker N–N and stronger B–N bonds for  $\beta$ -LiHB. This reveals a strong electronic modification induced by the alkaline cation, as reported elsewhere.<sup>8,9,12,13</sup> Armstrong et al. reported that the formation of Li<sup>+</sup>···H<sup>δ-</sup> long-range interactions results in the increase of the Lewis basicity of the NH<sub>3</sub> moiety in AB derivatives,<sup>14</sup> which supports the strengthening we have predicted from the FTIR results.

Figure 1b shows the <sup>11</sup>B MAS NMR spectrum of  $\beta$ -LiHB. The signal of boron of  $\beta$ -LiHB is centered at –19.1 ppm and shows a single environment. Unlike in pristine HB, there is no quadrupolar effect, which could potentially be due to an interaction among the two quadrupolar elements: <sup>11</sup>B with  $s = 3/2$  and <sup>7</sup>Li with  $s = 3/2$ . No quadrupolar interaction was observed in NaHB.<sup>13</sup> These observations demonstrate that the

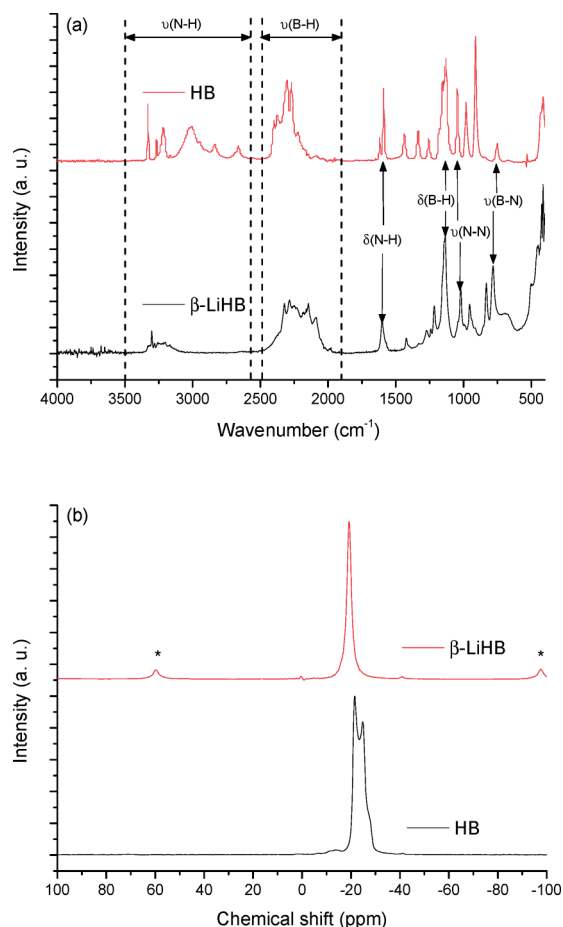


**Figure 1.** (a) FTIR and (b)  $^{11}\text{B}$  MAS NMR (the spinning sidebands are indicated by \*) spectra for  $\beta\text{-LiHB}$  and HB.

units in the crystal of  $\beta\text{-LiHB}$  are all equivalent and the insertion of the lithium modifies notably the electron repartition around the boron, which has become isotropic.

**Crystal Structure of  $\beta\text{-LiHB}$ .** The XRD pattern of  $\beta\text{-LiHB}$  was indexed as a single phase using an orthorhombic  $Pbca$  (No. 61) space group with  $a = 10.25182(11)$  Å,  $b = 8.47851(10)$  Å, and  $c = 7.46891(8)$  Å. The crystal structure was solved by global optimization with a parallel tempering algorithm using FOX software,<sup>15</sup> and then refined with the Rietveld method, anisotropically for non-H atoms, in the JANA2006 software.<sup>16</sup> After refinement, the following agreement factors were obtained:  $R_p = 2.3\%$ ;  $R_{wp} = 5.9\%$  (conventional);  $GOF = 9.02$ . The calculated pattern was then compared to the experimental one and both matched (Figure 2b).

Furthermore, removal of only one H atom in this light-Z system results in an increase of GOF up to 13. This assumption was confirmed by the refinement of the H positions, which lead to the expected staggered configuration on the  $\text{sp}^3$ -hybridized pivot (Figure 3). Despite the high sensitivity of synchrotron X-rays to H atoms in light hydrides,<sup>17</sup> only the average position of the electron cloud can be determined.

Accordingly, a systematic correction for the position of the H elements was introduced by extending the lengths of the B–H and N–H bonds to the ideal values of 1.22 and 1.03 Å, respectively.<sup>18</sup> The resulting coordinates are listed in Table S1 (Supporting Information). The crystal structure illustrated in Figure 4 shows that  $\text{H}^{\delta-}$  of LiH reacted with  $\text{H}^{\delta+}$  of the central nitrogen of HB (Figure 4a), leading to the formation of the new

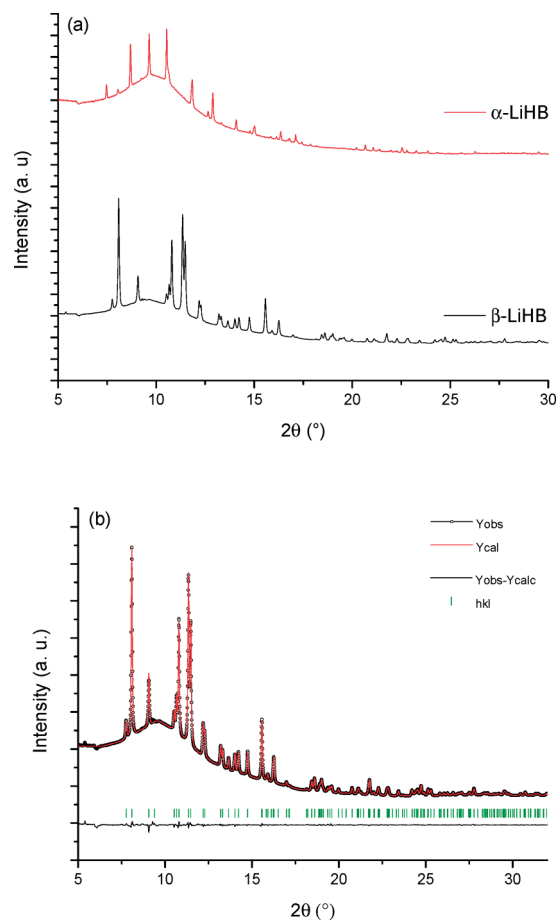


**Figure 2.** (a) High-resolution XRD patterns ( $\lambda = 0.693203$  Å) of the two phases of LiHB, i.e.,  $\alpha\text{-LiHB}$  and  $\beta\text{-LiHB}$ . (b) Comparison of the calculated (red line) and experimental (black circles) patterns. The difference is shown by the black line. The green vertical bars represent the calculated position of Bragg peaks for the  $\beta\text{-LiHB}$  phase.

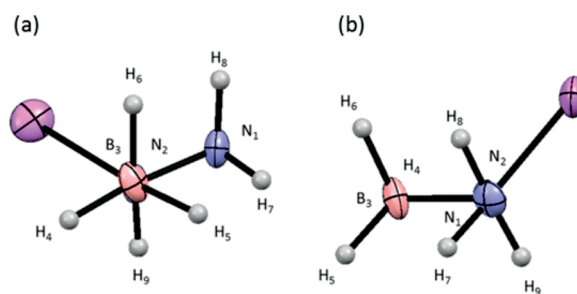


**Figure 3.** Representation of the staggered conformation for H on the  $\text{sp}^3$  pivot: (a) along the  $\text{N}_2\text{-B}_3$  bond and (b) along the  $\text{N}_2\text{-N}_1$  bond.

crystal phase of LiHB and  $\text{H}_2$ . This mode of deprotonation is consistent with those observed in the compounds  $\text{NaHB}$  and  $\alpha\text{-LiHB}$  and the complex  $\text{LiHB}\cdot 2\text{HB}$ .<sup>12,13</sup>

Figure 4b shows that  $\text{Li}^+$  has a tetrahedral environment: it interacts with four  $\text{N}_2\text{H}_3\text{BH}_3^-$  entities. A tetrahedral coordination polyhedron is typical for the metal atom in ambient pressure phases of lithium borohydride  $\text{LiBH}_4$ .<sup>18</sup> Two corners of the tetrahedron are occupied by  $\text{BH}_3$  groups ( $\text{B}_3\cdots\text{Li}^+$ : 2.624(5) and 2.622(6) Å), and the interaction occurs through the  $\text{BH}_2$  edge. Consequently,  $\text{Li}^+$  modifies the B–H bond polarization and decreases the electronic density around the B atoms, which explains the observations made by FTIR (Figure

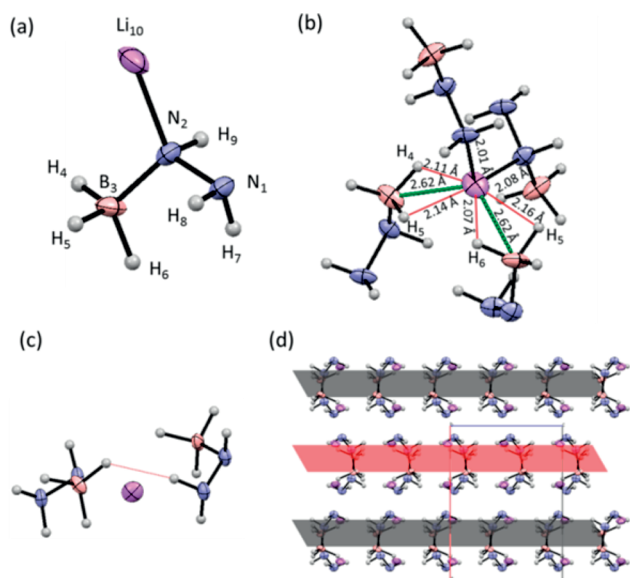


**Figure 4.** Crystal structure of  $\beta$ -LiHB with a detailed view of: (a) the asymmetric unit with labels; (b) the coordination of  $\text{Li}^+$ ; (c) the intermolecular  $\text{H}^{\delta+}\cdots\text{H}^{\delta-}$  dihydrogen bond according to Klooster et al.'s definition<sup>20</sup> ( $\text{H}_4\cdots\text{H}_7 = 2.25$  Å,  $\text{B}_3\text{-H}_4\cdots\text{H}_7 = 106.8^\circ$ , and  $\text{N}_1\text{-H}_7\cdots\text{H}_4 = 171.2^\circ$ ); and (d) the representation of the parallel planes on which the  $\text{H}^{\delta+}\cdots\text{H}^{\delta-}$  network extends.

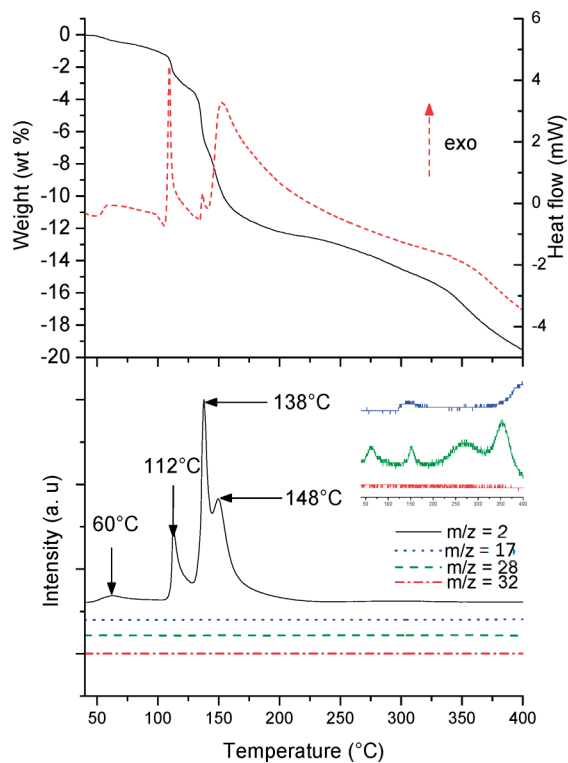


**Figure 5.** TGA/DSC ( $2^\circ\text{C min}^{-1}$ ) and MS results of  $\beta$ -LiHB: with  $m/z = 2$  for  $\text{H}_2$ ,  $m/z = 17$  for  $\text{NH}_3$ ,  $m/z = 28$  for  $\text{N}_2$ , and  $m/z = 32$  for  $\text{N}_2\text{H}_4$ . For the MS results, the inset is a zoom ( $\times 1000$ ) for the gases  $\text{NH}_3$ ,  $\text{N}_2$ , and  $\text{N}_2\text{H}_4$ .

1a) and confirms the  $\text{Li}^+\cdots\text{H}^{\delta-}$  interactions. This effect should lead to an activation of  $\text{H}^{\delta-}$  and, therefore, to an increase of its reactivity.<sup>19</sup> On the other hand,  $\text{Li}^+$  is coordinated with two N atoms from two different anions. The first coordination is done

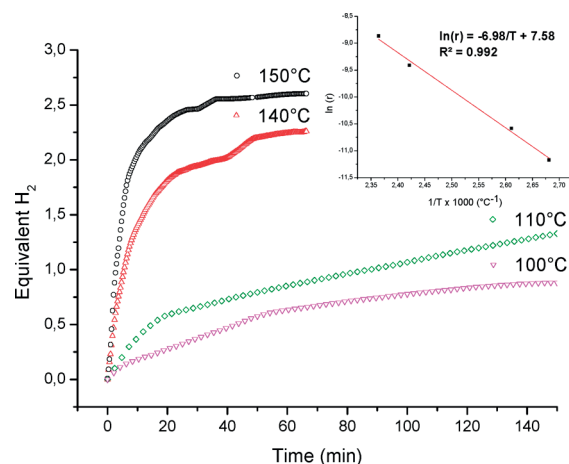


**Figure 6.** Volumetric measurements under isothermal treatment at 100, 110, 140, and 150  $^\circ\text{C}$  of  $\beta$ -LiHB. The inset figure is the Arrhenius plot for the determination of the apparent activation energy from the data of the volumetric measurements.

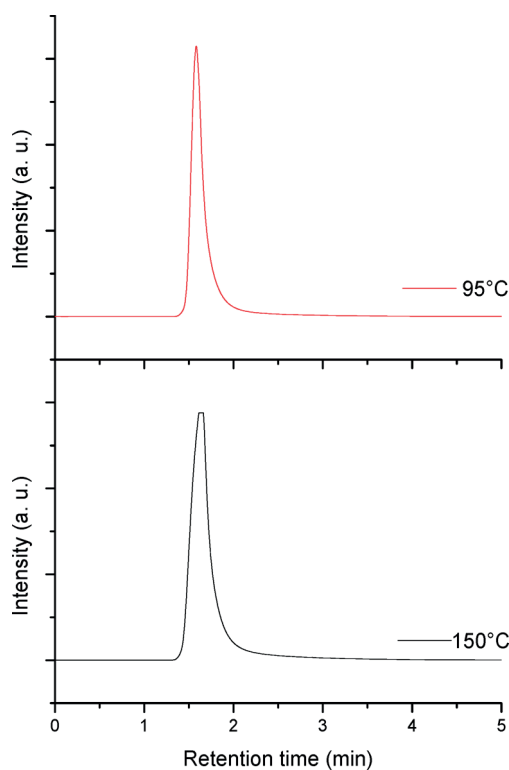


**Figure 7.** Analysis by GC of hydrogen liberated during a 2 h isothermal treatment of  $\beta$ -LiHB at 95 and 150  $^\circ\text{C}$ . No trace of ammonia was found in our experimental conditions, and the curves are not represented here.

by the substitution of  $\text{H}^{\delta-}$  by  $\text{Li}^+$ , with a  $\text{Li}^+\cdots\text{N}_2$  distance of  $2.086(4)$  Å.  $\text{Li}^+$  also coordinates the terminal N atom through an interaction with the lone electron pair of N, leading to a  $\text{Li}^+\cdots\text{N}_1$  distance of  $2.013(4)$  Å. By the same way, these two anions are connected to another  $\text{Li}^+$ , forming a cluster-like structure (Figure S1, Supporting Information). This kind of coordination is also observed in the complex  $\text{LiHB}\cdot 2\text{HB}$  (Figure S2, Supporting Information) but is not present in the  $\alpha$ -LiHB,<sup>12</sup> where the  $\text{Li}^+$  cations are bridging by two  $\text{BH}_3$  groups (Figure S3, Supporting Information). The distance between the two  $\text{Li}^+$  cations is shorter in the high-temperature

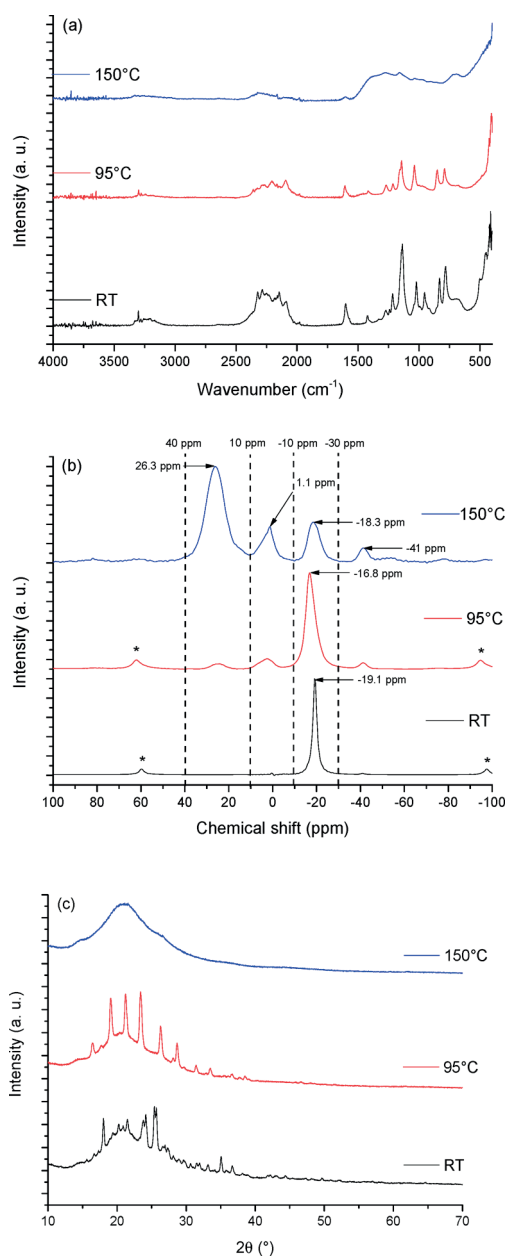


**Figure 8.** (a) FTIR and (b)  $^{11}\text{B}$  MAS NMR (spinning sidebands are indicated by \*) spectra and (c) XRD patterns of the solid residues recovered after a 2 h heat treatment of  $\beta$ -LiHB at 95 and 150 °C. For comparison, the spectrum of  $\beta$ -LiHB is also shown.

phase (3.31 Å) than in  $\beta$ -LiHB (3.49 Å), suggesting a better stability of the low-temperature phase. The  $\text{Li}^+\cdots\text{N}$  and  $\text{Li}^+\cdots\text{B}$  distances are in good agreement with previous reports on lithium amidoborane and  $\alpha$ -LiHB.<sup>12,20</sup> The tetrahedron around  $\text{Li}^+$  is slightly distorted: the angle  $\text{B}_3\cdots\text{Li}\cdots\text{B}_3$  ( $118.7(2)^\circ$ ) is more opened than the angles  $\text{N}_1\cdots\text{Li}\cdots\text{B}_3$  ( $103.8(2)^\circ$ ) and  $\text{N}_1\cdots\text{Li}\cdots\text{N}_2$  ( $109.1(2)^\circ$ ). The B–N and N–N distances are 1.549(2) and 1.495(2) Å, respectively. The former is shorter than in HB,<sup>11</sup> whereas the latter is longer, being consistent with the system of  $\text{Li}^+\cdots\text{H}^{\delta-}$  interaction inducing a reinforcement in the Lewis basicity of the  $\text{N}_2\text{H}_4$  moiety and strong electronic rearrangement due to the presence of  $\text{Li}^+$

The solid state of  $\beta$ -LiHB is stabilized by an intermolecular head-to-tail  $\text{H}^{\delta+}\cdots\text{H}^{\delta-}$  interaction (Figure 4c), with a geometry in good agreement with Klooster et al.'s definition of a

dihydrogen bond: the angle  $\text{B}_3\text{--H}_4\cdots\text{H}_7$  is bent ( $106.8^\circ$ ), whereas the  $\text{N}_1\text{--H}_7\cdots\text{H}_4$  fragment is almost linear ( $171.2^\circ$ ).<sup>21</sup> Similar contacts were also reported for HB,<sup>11</sup>  $\alpha$ -LiHB,<sup>12</sup> and NaHB.<sup>13</sup> The distance between  $\text{H}^{\delta+}$  and  $\text{H}^{\delta-}$  is 2.25 Å, longer than that for HB (2.01 Å),<sup>22</sup> but shorter than the sum of the van der Waals radii for H atoms (2.4 Å). The intermolecular head-to-tail  $\text{H}^{\delta+}\cdots\text{H}^{\delta-}$  interactions form chains (Figure 4d). For comparison, the network of dihydrogen bonds in HB extends in two dimensions and in three dimensions for AB.<sup>11,21</sup>

**Thermal Characterizations.** The TGA–MS results of  $\beta$ -LiHB are presented in Figure 5. They show that the decomposition of the borane is a five-step process. The decomposition starts at 40 °C, and over the range of 40–104 °C,  $\beta$ -LiHB liberates  $\text{H}_2$  and  $\text{N}_2$ , corresponding to a mass loss of 1.2 wt %. The second decomposition step ends at 127 °C, with 2.2 wt % of  $\text{H}_2$  being generated. The third step takes place over the range of 127–144 °C. Pure  $\text{H}_2$  (4.4 wt %) is released. For the last two steps, up to 400 °C, ca. 8.7 wt % of a mixture of  $\text{H}_2$ ,  $\text{NH}_3$ , and  $\text{N}_2$  evolves. Therefore, about 3 mol of  $\text{H}_2$  per mole of  $\beta$ -LiHB (i.e., 11.6 wt %  $\text{H}_2$ ) is generated. In our experimental conditions, no trace of  $\text{N}_2\text{H}_4$  is detected and the amount of formed  $\text{NH}_3$  is drastically decreased compared to HB. It is worth noting the absence of diborane and borazine in the gas stream (Figure S4, Supporting Information). Similar observations were reported for  $\alpha$ -LiHB and NaHB.<sup>12,13</sup> The DSC results (Figure 5) show that each of the decomposition processes is exothermic. Reversibility of H storage should then be thermodynamically difficult.<sup>8,12</sup> Another observation is that there is a slight deviation of the baseline at about 90 °C. This may be due to a phase transition.

The behavior of  $\beta$ -LiHB under prolonged isothermal heating was studied at 100, 110, 140, and 150 °C. The results of the volumetric measurements are shown in Figure 6. Three main observations stand out. First, there is no induction time: the  $\text{H}_2$  generation starts immediately. Second, the decomposition in isothermal conditions is a two-step process, with a first step that is faster than the second one. During the former step, the borane molecules are subjected to dehydrocoupling (fast intermolecular reactions) with formation of a polymeric residue and release of hydrogen. Then, the polymeric residue dehydrogenates through intramolecular reactions, with slower kinetics, since such reactions have high energy barriers and generally take place at higher temperatures under dynamic conditions.<sup>4–12</sup> Third,  $\beta$ -LiHB shows improved dehydrogenation properties in comparison to neat HB. For example, after 1 h of heating,  $\beta$ -LiHB is able to release 0.6, 0.9, 2.2, and 2.6 equiv of  $\text{H}_2$  at 100, 110, 140, and 150 °C, respectively, whereas the amount of  $\text{H}_2$  is 0.4, 1.1, and 1.4 equiv of  $\text{H}_2$  for HB at 100, 140, and 150 °C, respectively (no datum available at 110 °C for HB).<sup>11</sup> Note that the purity of  $\text{H}_2$  was determined by analyzing the gas mixture collected during the isothermal experiments at 95 and 150 °C. The results are shown in Figure 7. Unlike for HB,<sup>10,11,23</sup> no trace of ammonia was found in our conditions.

For the isothermal experiments, the rate ( $r$  in  $\text{mol H}_2 \text{ min}^{-1}$ ) of the first decomposition step was determined and then the rates were exploited to determine the apparent activation energy with the help of the Arrhenius equation. The evolution of  $\ln(r)$  as a function of  $1/T$  ( $\text{K}^{-1}$ ) is shown in Figure 6. From the slope, an apparent activation energy of  $58 \text{ kJ mol}^{-1}$  was found.

**Characterization of Solid Residues.** The solid residues forming after 2 h of isothermal treatment at 95 and 150 °C were recovered to be characterized. In Figure 8a are reported

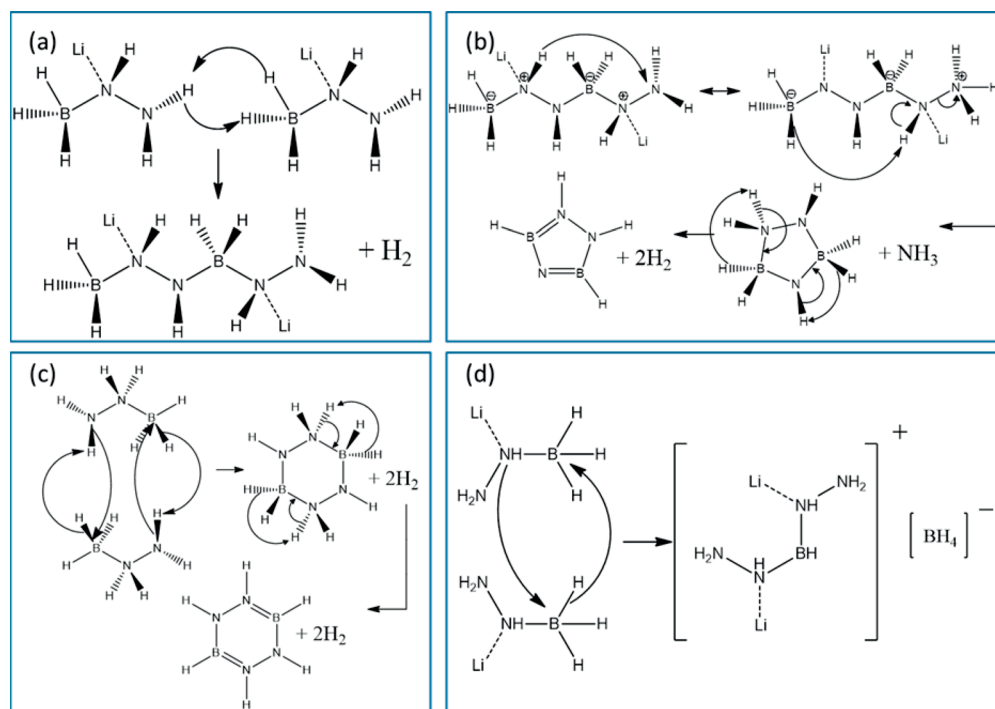


**Figure 9.** Proposition of mechanisms for the formation of monomeric units and BLHDB: (a) linear dimer with boron in  $sp^3$  hybridization; (b) 5-ring center monomer formed by proton exchange, then cyclization with  $NH_3$  release and finally dehydrocyclization, where boron is in  $sp^2$  hybridization; (c) 6-ring center monomer formed by cyclization of 2 HB monomers, followed by dehydrocyclization; (d) formation of BLHDB.

the FTIR spectra. The intensity of the N–H stretching bands ( $3390\text{--}3070\text{ cm}^{-1}$ ) has decreased for the residue formed at  $95\text{ }^\circ\text{C}$ , but these bands are no longer present for the residue formed at  $150\text{ }^\circ\text{C}$ . Similar observations can be made for the B–H stretching bands ( $2480\text{--}1900\text{ cm}^{-1}$ ), though some B–H bonds are still present for the latter residue. With respect to the bands within the range of  $1500\text{--}500\text{ cm}^{-1}$ , they have broadened. These results are explained by different dehydrogenation extents (Figure 6).

Figure 8b shows the  $^{11}\text{B}$  MAS NMR spectra of the two solid residues. For both, it seems that four species have formed as four additional signals can be distinguished. The first one peaks at  $-41\text{ ppm}$ . It is attributed to a  $BH_4^-$  environment. We assume that a compound similar to diammoniate of diborane  $[(NH_3)_2BH_2]^+[BH_4]^-$  (DADB), which is the reaction intermediate forming during the thermal decomposition of AB,<sup>24</sup> has formed. We propose the formation of bis(lithium hydrazide) of diborane  $[(LiN_2H_3)_2BH_2]^+[BH_4]^-$  (BLHDB), though further works (in progress) are required to confirm. The three other signals are visible over the ranges of  $-30$  to  $-10$ ,  $-10$  to  $10\text{ ppm}$ , and  $10\text{--}40\text{ ppm}$ . They can be ascribed to an oligo-/polymeric material with B having an  $sp^3$  hybridization (e.g.,  $NBH_2$ ), a polycyclic polymer, and a polymeric material with B showing  $sp^2$  hybridization (e.g.,  $N_2BH$  or  $N_3B$ ).<sup>24,25</sup> We, therefore, suggest that the solid residues consist of a mixture of polymers with linear and cyclic monomeric units, and species like BLHDB. For the solid residue recovered after heating  $\beta$ -LiHB at  $150\text{ }^\circ\text{C}$  for 2 h, the content of polymers with cyclic monomeric units is higher, suggesting the formation of a material with an  $N_3B$  environment.

Powder XRD was also used to analyze the solid residues (Figure 8c). After 2 h at  $95\text{ }^\circ\text{C}$ ,  $\beta$ -LiHB evolved into a material with a different crystalline structure. It transformed into  $\alpha$ -LiHB. This result is consistent with the observation made by

DSC, namely, a baseline deviation that could be due to a phase transition such as  $\beta$ -LiHB  $\rightarrow$   $\alpha$ -LiHB. The phase  $\alpha$  is thus more stable under heating. With respect to the solid residue heated at  $150\text{ }^\circ\text{C}$  for 2 h, the XRD pattern shows the formation of an amorphous material, which is the signature of a mixture of boron- and nitrogen-based polymeric species.<sup>26</sup>

**Proposition of Mechanisms.** The aforementioned results have shown that (i) the main decomposition pathway of  $\beta$ -LiHB is dehydrogenation; (ii) some ammonia is emitted under nonisothermal heating; (iii) the solid residues consist of a mixture of polymeric materials containing boron in  $sp^3$  and  $sp^2$  hybridization states; and (iv)  $BH_4^-$  is also present in the residues. We, therefore, suggest the formation of monomeric units by intermolecular reaction between  $H^{\delta-}$  and  $H^{\delta+}$ , and subsequent polycondensation of these species. Figure 9a–c shows the likely mechanisms. One path leading to the formation of  $NH_3$  is also suggested (Figure 9b). We have proposed above that the intermediate BLHDB plays a role of an activation agent in the HB decomposition; the possible mechanism of its formation is represented in Figure 9d.

## CONCLUSIONS

We have reported the synthesis and characterization results of a new crystalline phase of lithium hydrazinidoborane, called  $\beta$ -LiHB ( $\beta$ - $LiN_2H_3BH_3$ ), for chemical hydrogen storage. It was prepared from LiH and  $N_2H_4BH_3$  (HB) by mechanochemical synthesis at ambient conditions. The crystal structure of  $\beta$ -LiHB was solved in the orthorhombic space group  $Pbca$  (No. 61) with  $a = 10.25182(11)\text{ \AA}$ ,  $b = 8.47851(10)\text{ \AA}$ , and  $c = 7.46891(8)\text{ \AA}$ . Lithium hydrazinidoborane manifests two polymorphs,  $\beta$ -LiHB at low temperatures and  $\alpha$ -LiHB at high temperatures. The presence of the  $Li^+$  cation makes this material more reactive and less stable upon heating than the parent HB. Thermal and calorimetric characterizations have

shown improved dehydrogenation properties. Heated at 5 °C min<sup>-1</sup>,  $\beta$ -LiHB is able to release about 11.6 wt % H<sub>2</sub> up to 400 °C, with drastically reduced amounts of unwanted byproducts, such as N<sub>2</sub>H<sub>4</sub> and NH<sub>3</sub>. In isothermal conditions, at 150 °C, about 10 wt % of pure H<sub>2</sub> is generated in less than 1 h, with a real improvement in terms of dehydrogenation kinetics. From analyses of the released gases and solid residues, the dehydrogenation paths are discussed. The appearance of bis(lithium hydrazide) of diborane [(LiN<sub>2</sub>H<sub>3</sub>)<sub>2</sub>BH<sub>2</sub>]<sup>+</sup>[BH<sub>4</sub>]<sup>-</sup>, acting as an activation intermediate, and formation of polymeric residues constituted of linear and cyclic monomeric units are suggested. Works are in progress to better identify the different species. To conclude, we show that  $\beta$ -LiHB has a potential for chemical hydrogen storage if combined with an adapted effective recycling process of the solid residues.

## ■ ASSOCIATED CONTENT

### Supporting Information

The atomic positions for  $\beta$ -LiHB (Table S1), the representations of the various cluster-like structures of LiHB-based materials (Figures S1–S3), and MS results of the thermal decomposition of  $\beta$ -LiHB (Figure S4). This material is available free of charge via the Internet at <http://pubs.acs.org>.

## ■ AUTHOR INFORMATION

### Corresponding Author

\*E-mail: [umit.demirci@um2.fr](mailto:umit.demirci@um2.fr).

### Author Contributions

All authors have given approval to the final version of the manuscript.

### Notes

The authors declare no competing financial interest.

## ■ ACKNOWLEDGMENTS

The authors would like to acknowledge the support of the Direction Générale des Armées (DGA, France), the Centre National de la Recherche Scientifique (CNRS, France), and Fonds de la Recherche Scientifique (FNRS, Belgium). U.B.D. and T.I. would like to thank the JSPS (Japan) for partially supporting the present work through the JSPS Summer Program given to R.M. Also, U.B.D. and Y.F. would like to thank the COST program MP1103 called “Nanostructured Materials for Solid-State Hydrogen Storage” for partially supporting the present work through the short-term scientific mission given to R.M. Finally, Y.F. and R.M. acknowledge the SNBL (ESRF, France) for the beam-time.

## ■ REFERENCES

- (1) Armaroli, N.; Balzani, V. *ChemSusChem* **2011**, *4*, 21–36.
- (2) *Targets for Onboard Hydrogen Storage Systems for Light-Duty Vehicles*; U.S. Department of Energy: Washington, DC, 2009; <http://www1.eere.energy.gov>.
- (3) Demirci, U. B.; Miele, P. *Energy Environ. Sci.* **2009**, *2*, 627–637.
- (4) Staubitz, A.; Robertson, A. P. M.; Manners, I. *Chem. Rev.* **2010**, *110*, 4079–4124.
- (5) Baitalov, F.; Baumann, J.; Wolf, G.; Jaenicke-Rossler, K.; Leitner, G. *Thermochim. Acta* **2002**, *391*, 159–168.
- (6) Carpenter, J. D.; Ault, B. S. *Chem. Phys. Lett.* **1992**, *197*, 171–174.
- (7) (a) Gutowska, A.; Li, L.; Shin, Y.; Wang, C. M.; Li, X. S.; Linehan, J. C.; Smith, R. S.; Kay, B. D.; Schmid, B.; Shaw, W.; Gutowski, M.; Autrey, T. *Angew. Chem., Int. Ed.* **2005**, *44*, 3578–3582. (b) Goettker-Schnetmann, L.; White, P.; Brookhart, M. *J. Am. Chem. Soc.* **2004**, *126*, 1804–1811. (c) Bluhm, M. E.; Bradley, M. G.; Butterick, R., III;

Kusari, U.; Sneddon, L. G. *J. Am. Chem. Soc.* **2006**, *128*, 7748–7749. (d) Benzouaa, R.; Demirci, U. B.; Chiriac, R.; Toche, F.; Miele, P. *Thermochim. Acta* **2010**, *509*, 81–86.

(8) Xiong, Z.; Yong, C. K.; Wu, G.; Chen, P.; Shaw, W.; Karkamkar, A.; Autrey, T.; Jones, M. O.; Johnson, S. R.; Edwards, P. P.; David, W. I. F. *Nat. Mater.* **2008**, *7*, 138–141.

(9) Fijalkowski, K. J.; Grochala, W. *J. Mater. Chem.* **2009**, *19*, 2043–2050.

(10) Hügle, T.; Kühnel, M. F.; Lentz, D. *J. Am. Chem. Soc.* **2009**, *131*, 7444–7446.

(11) Moury, R.; Moussa, G.; Demirci, U. B.; Hannauer, J.; Bernard, S.; Petit, E.; van der Lee, A.; Miele, P. *Phys. Chem. Chem. Phys.* **2012**, *14*, 1768–1777.

(12) Wu, H.; Zhou, W.; Pinkerton, F. E.; Udovic, T. J.; Yildirim, T.; Rush, J. *J. Energy Environ. Sci.* **2012**, *5*, 7531–7535.

(13) Moury, R.; Demirci, U. B.; Ichikawa, T.; Filinchuk, Y.; Chiriac, R.; van der Lee, A.; Miele, P. *ChemSusChem* **2013**, *6*, 667–673.

(14) Armstrong, D. R.; Perkins, P. G.; Walker, G. T. *J. Mol. Struct.: THEOCHEM* **1985**, *122*, 189–204.

(15) Favre-Nicolin, V.; Cerny, R. *J. Appl. Crystallogr.* **2002**, *35*, 734–743.

(16) Petricek, V.; Dusek, M.; Palatinus, L. *Jana2006: The Crystallographic Computing System*; Institute of Physics, Academy of Sciences: Praha, Czech Republic, 2006.

(17) Filinchuk, Y.; Chernyshov, D.; Černý, R. *J. Phys. Chem. C* **2008**, *112*, 10579–10584.

(18) Filinchuk, Y.; Hagemann, H. *Eur. J. Inorg. Chem.* **2008**, 3127–3133.

(19) (a) Hartman, M. R.; Rush, J. J.; Udovic, T. J.; Bowman, R. C., Jr.; Hwang, S.-J. *J. Solid State Chem.* **2007**, *180*, 1298–1305.

(b) Filinchuk, Y.; Chernyshov, D.; Nevidomskyy, A.; Dmitriev, V. *Angew. Chem., Int. Ed.* **2008**, *47*, 529–532.

(20) Wu, H.; Zhou, W.; Yildirim, T. *J. Am. Chem. Soc.* **2008**, *130*, 14834–14839.

(21) Klooster, W. T.; Koetzle, T. F.; Siegbahn, P. E. M.; Richardson, T. B.; Crabtree, R. H. *J. Am. Chem. Soc.* **1999**, *121*, 6337–6343.

(22) Mebs, S.; Grabowsky, S.; Förster, D.; Kickbusch, R.; Hartl, M.; Daemen, L. L.; Morgenroth, W.; Luger, P.; Paulus, B.; Lentz, D. *J. Phys. Chem. A* **2010**, *114*, 10185–10196.

(23) Goubeau, J.; Ricker, E. Z. *Anorg. Allg. Chem.* **1961**, *310*, 123–142.

(24) Stowe, A. C.; Shaw, W. J.; Linehan, J. C.; Schmid, B.; Autrey, T. *Phys. Chem. Chem. Phys.* **2007**, *9*, 1831–1836.

(25) (a) Gervais, C.; Framery, E.; Duriez, C.; Maquet, J.; Vaultier, M.; Babonneau, F. *J. Eur. Ceram. Soc.* **2004**, *25*, 129–135. (b) Shimoda, K.; Zhang, Y.; Ichikawa, T.; Miyaoka, H.; Kojima, Y. *J. Mater. Chem.* **2011**, *21*, 2609–2615. (c) Kim, D.-P.; Moon, K.-T.; Kho, J.-G.; Economy, J.; Gervais, C.; Babonneau, F. *Polym. Adv. Technol.* **1999**, *10*, 702–712.

(26) Hu, M. G.; Geanangel, R. A.; Wendlandt, W. W. *Thermochim. Acta* **1978**, *23*, 249–255.